

**AFRL-ML-WP-TR-2001-4061**



**LASER-BASED ULTRASOUND FOR REMOTE AND  
LIMITED-ACCESS INSPECTION APPLICATIONS**

**ROBERT C. ADDISON, JR. AND ANDREW D.W. McKIE**

**ROCKWELL SCIENCE CENTER, LLC  
1049 CAMINO DOS RIOS  
THOUSAND OAKS, CA 91360**

**DECEMBER 2000**

**FINAL REPORT FOR 01 APRIL 1998 THROUGH 30 NOVEMBER 2000**

**APPROVED FOR PUBLIC RELEASE, DISTRIBUTION UNLIMITED.**

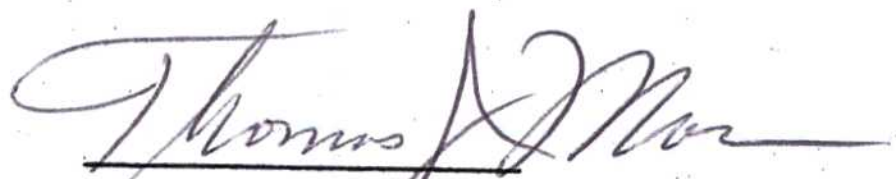
**MATERIALS AND MANUFACTURING DIRECTORATE  
AIR FORCE RESEARCH LABORATORY  
AIR FORCE MATERIEL COMMAND  
WRIGHT-PATTERSON AFB, OH 45433-7750**

## NOTICE

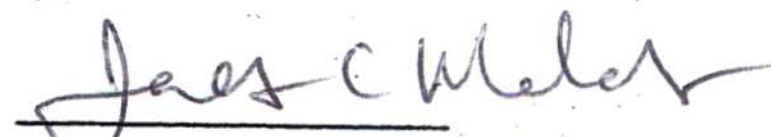
WHEN GOVERNMENT DRAWINGS, SPECIFICATIONS, OR OTHER DATA INCLUDED IN THIS DOCUMENT FOR ANY PURPOSE OTHER THAN GOVERNMENT-RELATED PROCUREMENT DOES NOT IN ANY WAY OBLIGATE THE US GOVERNMENT. THE FACT THAT THE GOVERNMENT FORMULATED OR SUPPLIED THE DRAWINGS, SPECIFICATIONS, OR OTHER DATA DOES NOT LICENSE THE HOLDER OR ANY OTHER PERSON OR CORPORATION, OR CONVEY ANY RIGHTS OR PERMISSION TO MANUFACTURE, USE, OR SELL ANY PATENTED INVENTION THAT MAY RELATE TO THEM.

THIS REPORT IS RELEASABLE TO THE NATIONAL TECHNICAL INFORMATION SERVICE (NTIS). AT NTIS, IT WILL BE AVAILABLE TO THE GENERAL PUBLIC, INCLUDING FOREIGN NATIONS.

THIS TECHNICAL REPORT HAS BEEN REVIEWED AND IS APPROVED FOR PUBLICATION.



THOMAS J. MORAN, Project Engineer  
Nondestructive Evaluations Branch  
Metals, Ceramics & NDE Division



JAMES C. MALAS, Chief  
Nondestructive Evaluations Branch  
Metals, Ceramics & NDE Division



GERALD J. PETRAK, Assistant Chief  
Metals, Ceramics & NDE Division  
Materials & Manufacturing Directorate

DO NOT RETURN COPIES OF THIS REPORT UNLESS CONTRACTUAL OBLIGATIONS OR NOTICE ON A SPECIFIC DOCUMENT REQUIRES ITS RETURN.

# REPORT DOCUMENTATION PAGE

*Form Approved  
OMB No. 074-0188*

Public reporting burden for this collection of information is estimated to average 1 hour per response, including the time for reviewing instructions, searching existing data sources, gathering and maintaining the data needed, and completing and reviewing this collection of information. Send comments regarding this burden estimate or any other aspect of this collection of information, including suggestions for reducing this burden to Washington Headquarters Services, Directorate for Information Operations and Reports, 1215 Jefferson Davis Highway, Suite 1204, Arlington, VA 22202-4302, and to the Office of Management and Budget, Paperwork Reduction Project (0704-0188), Washington, DC 20503.

<b>1. AGENCY USE ONLY (Leave blank)</b>			<b>2. REPORT DATE</b> December 2000	<b>3. REPORT TYPE AND DATES COVERED</b> Final Report, 4/01/1998 – 11/30/2000
<b>4. TITLE AND SUBTITLE</b> Laser-Based Ultrasound for Remote and Limited-Access Inspection Applications			<b>5. FUNDING NUMBERS</b> C: F33615-97-D-5271 PE: 63112F PR: 4349 TA: 40 WU: 01	
<b>6. AUTHOR(S)</b> Robert C. Addison, Jr. and Andrew D.W. McKie				
<b>7. PERFORMING ORGANIZATION NAME(S) AND ADDRESS(ES)</b> Rockwell Science Center, LLC 1049 Camino Dos Rios Thousand Oaks, CA 91360			<b>8. PERFORMING ORGANIZATION REPORT NUMBER</b> 98-S437-0003-C1	
<b>9. SPONSORING / MONITORING AGENCY NAME(S) AND ADDRESS(ES)</b> MATERIALS AND MANUFACTURING DIRECTORATE AIR FORCE RESEARCH LABORATORY AIR FORCE MATERIEL COMMAND WRIGHT-PATTERSON AIR FORCE BASE, OH 45433-7750 POC: Thomas Moran, AFRL/MLP, 937-255-9800			<b>10. SPONSORING / MONITORING AGENCY REPORT NUMBER</b> AFRL-ML-WP-TR-2001-4061	
<b>11. SUPPLEMENTARY NOTES</b>				
<b>12a. DISTRIBUTION / AVAILABILITY STATEMENT</b> Approved for public release, distribution unlimited.			<b>12b. DISTRIBUTION CODE</b>	
<b>13. ABSTRACT (Maximum 200 Words)</b> The design, implementation, and proof-of-concept demonstration of a fiber-based Cassegrain optical scanning system was completed. Optical generation and detection with the fiber-based Cassegrain optical scanning system over 100-m lengths of optical fiber was demonstrated. High peak power, Q-switched Nd:YAG laser pulses (>45 mJ/pulse at 532 nm) through optical fiber in a robust manner was successfully delivered. This program established the absolute thermoelastic generation efficiency for four different laser wavelengths and eight different material/boundary conditions.				
<b>14. SUBJECT TERMS</b> laser-based ultrasound, fiber-coupling, Cassegrain scanning system, and optical ray-tracing			<b>15. NUMBER OF PAGES</b> 116	
			<b>16. PRICE CODE</b>	
<b>17. SECURITY CLASSIFICATION OF REPORT</b> Unclassified	<b>18. SECURITY CLASSIFICATION OF THIS PAGE</b> Unclassified	<b>19. SECURITY CLASSIFICATION OF ABSTRACT</b> Unclassified	<b>20. LIMITATION OF ABSTRACT</b> SAR	

## TABLE OF CONTENTS

Sections	Pages
List of Figures .....	v
List of Tables .....	x
1. Acknowledgements .....	xi
2. Introduction .....	1
2.1 Objective .....	2
2.2 Technical Approach.....	2
2.3 Major Accomplishments.....	3
3. The Fiber-Based Cassegrain Optical Scanning System .....	4
3.1 Introduction.....	4
3.2 Cassegrain Scanning System Design - Concept and Issues .....	5
3.3 Optimization of Laser Beam Coupling from the Target to the Optical Detection System.....	11
3.3.1 <i>Determination of Light Collection Efficiency of the Cassegrain System</i> .....	12
3.3.2 <i>Optimization of Light Coupling from the Collection Fiber to the SFPI</i> .....	19
3.3.3 <i>Optimization of Laser Beam Delivery with the Cassegrain Scanning System</i> ...	22
3.4 Experimental Characterization of the Optimized Cassegrain Scanning System ...	26
3.4.1 <i>Optimized Coupling and Delivery of the Generation and Probe Lasers to the Target</i> .....	27
3.4.2 <i>Ultrasonic Signal Detection with the Optimized Cassegrain Scanning System</i>	27
3.5 Summary and Discussion.....	28
4. Optical Fiber Delivery of High Peak-Power Laser Pulses .....	30
4.1 Optical Fiber Attenuation Characteristics.....	30
4.2 Fiber Damage Considerations .....	31
4.3 Fiber Core Size and Numerical Aperture Selection.....	32
4.4 Coupling of High Peak-Power Laser Pulses into Fibers.....	32
4.4.1 <i>Criteria For Optimum Coupling</i> .....	32
4.4.2 <i>Optimization of the Lens to Fiber Coupling Distance</i> .....	33
4.5 Experimental Results .....	34
4.5.1 <i>Fiber Coupling of the CO<sub>2</sub> Generation Laser</i> .....	34
4.5.2 <i>Fiber Coupling of the Alexandrite Generation Laser</i> .....	35
4.5.3 <i>Fiber Coupling of the Long-Pulse Nd:YAG Probe Laser</i> .....	36
4.5.4 <i>Fiber Coupling of the Q-Switched Nd:YAG Generation Laser</i> .....	37

4.5.5	<i>Summary and Discussion</i> .....	41
5.	Generation Efficiency Studies .....	43
5.1	Absolute Thermoelastic Ultrasonic Wave Generation Efficiency in Polymer-Matrix Composite Materials.....	43
5.2	Effects of Coating Thickness on the Thermoelastic Generation Efficiency.....	45
5.3	Summary and Discussion.....	47
6.	Conclusions and Summary .....	48
7.	References .....	50
8.	<b>List of Acronyms</b> .....	52
Appendix A	.....	53
A1.	Calculation of the Étendue for an SFPI .....	53
A2.	Calculation of Effective Aperture of an SFPI.....	56
Appendix B	.....	59
B1.	Analysis of Light Collection from the Target to the Receiving Optical Fiber .....	59
B1.1.	<i>A Paraxial Analysis</i> .....	59
B1.2.	<i>An Optical Ray-Tracing Analysis</i> .....	65
B2.	Analysis of Light Coupling from the Receiving Optical Fiber to the SFPI.....	68
B2.1.	<i>A Paraxial Analysis</i> .....	68
B2.2.	<i>An Optical Ray-Tracing Analysis</i> .....	73
Appendix C	Analysis of the Cassegrain Obscuration Losses .....	75
Appendix D	.....	83
D1.	Analysis of Light Coupling from a Delivery Optical Fiber to the Target .....	83
D1.1.	<i>A Paraxial Analysis</i> .....	83
D1.1.1 .	Collimating Method.....	83
D1.1.2 .	Imaging Method .....	89
D1.1.3 .	Summary of Paraxial Analysis .....	91
D1.2.	<i>Ray-Tracing Analysis of the Cassegrain Subassembly Relay-Optics</i> .....	91
Appendix E	Cross-Calibration of the SFPI with a Stabilized Michelson Interferometer .....	96

## LIST OF FIGURES

Figures		Pages
1.	Concept for a Fiber-Coupled Laser-Based Ultrasound (LBU) Inspection Unit for Remote and Limited-Access Inspection Applications .....	1
2.	Detection of Alexandrite Laser-Generated Ultrasonic Signals in a Black Graphite/Epoxy Panel Using the Fiber-Coupled Cassegrain Optical Scanning System.....	4
3.	Concept for the Fiber-Coupled Cassegrain Optical Scanning System. ....	6
4.	Schematic Diagram of the Cassegrain Optical Collection System. ....	6
5.	Photograph of the Cassegrain Optical Collection System .....	7
6.	Optical Layout for Calculating the Required Fiber Diameter Needed to Collect All of the Light Transmitted by a Lens at Both the Minimum and Maximum Range of the Target .....	9
7.	Maximum Ray Height at Fiber Face as Focal Length of Light Collecting Lens Varies .....	10
8.	Minimum Required Fiber Diameter to Collect All of the Light versus Lens Diameter for a Fiber NA of 0.22. (Lens Diameters for a Fiber Diameter of 1.5 mm are Marked) .....	11
9.	Minimum Required Fiber Diameter to Collect All of the Light versus Lens Diameter for a Fiber NA of 0.11. (Lens Diameters for a Fiber Diameter of 1.5 mm are Marked) .....	11
10.	Schematic Diagram Illustrating the Relevant Parameters Used for the Analytical and Ray Tracing Obscuration Analyses .....	13
11.	Analytical Paraxial Calculation of the Loss of Light from a 5.85 mm Diameter Probe Laser Spot Scattered from the Target. Light Loss Results from Obscuration of Incoming Light by the Secondary Mirror and from Overfilling of 1, 2, 5 and 7 mm Diameter Optical Fibers .....	14
12.	Optical Ray-Trace Calculations of the Loss of Light from a 5.85 mm Diameter Probe Laser Spot Scattered from the Target. Light Loss Results from Obscuration Caused by the Secondary Mirror/Spider Assembly and from Overfilling of a 7 mm Diameter Optical Fiber .....	15
13.	Cassegrain System Obscuration Calculations for a 1.5 mm Core Diameter Optical Fiber (NA=0.38) and a 7 mm x 7 mm Optical Fiber Bundle .....	16
14.	Cassegrain System Obscuration Calculations for a 2.0 mm Core Diameter Optical Fiber (NA=0.38) and a 7 mm x 7 mm Optical Fiber Bundle .....	16
15.	Spatial Characteristics of the Probe Laser Beam Incident on the Entry Face of the Optical Fiber Bundle at Ranges of 34, 46 and 50 Inches .....	17
16.	A Comparison of the Normalized Optical Power Collection Efficiency of the (a) Galvanometer and (b) Cassegrain Scanning Systems .....	19
17.	Beam and Lens Diameter as a Function of the Distance Between the lens and the Center of the SFPI Cavity for a) a 1 mm Source with an NA of 0.2 ( $\theta = 11.537^\circ$ ) and b) a 10 mm Source with the Same NA. The Lens Focal Length Is Selected to Image the Source at the Center of the SFPI with a Magnification that Will Minimize the Beam Size at the Output Mirror of the SFPI .....	21

## LIST OF FIGURES (Continued)

Figures		Pages
18.	Schematic Diagram of Model Used for Coupling Between an Optical Fiber and the SFPI .....	22
19.	Beam Diameter at Lens Versus Fiber NA for a Range of Fiber Diameters and a 6 mm Target Spot Diameter .....	24
20.	Schematic of LACIS-R Relay Optics Configuration Used to Transmit Generation Beam from Optical Fiber .....	25
21.	Schematic of an Improved Relay Optics Configuration Used to Transmit the Generation Beam from Optical Fiber to Target .....	26
22.	Detection of Q-Switched Nd:YAG Laser-Generated Ultrasonic Signals in a White-Painted Graphite/Epoxy Panel Using the Modified Fiber-Coupled Cassegrain Optical Scanning System .....	28
23.	Detection of Q-Switched Nd:YAG Laser-Generated Ultrasonic Signals in a White-Painted Graphite/Epoxy Panel. The Modified Fiber-Based Cassegrain System Was Used to Deliver the Generation Beam to the Target, but the Probe Beam Was Delivered and Collected Using a Bulk Optics Galvanometer Scanning System .....	28
24.	Spectral Response for 3M™ TECST™ – Coated Silica/Silica Optical Fiber .....	31
25.	Q-Switched Laser Pulse Energy Measured at the Input to the 910 $\mu\text{m}$ Core Diameter Silica/Silica Optical Fiber versus the Laser Energy Measured at the Fiber Output .....	38
26.	Experimental Vacuum Cell Configuration Used to Prevent Air-Breakdown when Coupling High Peak-Power Generation Laser Pulses into the Silica/Silica Optical Fiber .....	39
27.	Absolute Longitudinal Wave Displacement for the CO <sub>2</sub> , Nd:YAG ( $\lambda = 532$ and 1064 nm) and Alexandrite Generating Lasers When Used to Irradiate a Series of Polymer-Matrix Composite Specimens .....	44
28.	Plot Showing Variation in Thermoelastically Generated Longitudinal Wave Amplitude in an Aluminum Plate as a Function of the Applied Paint Thickness ....	46
29.	Reverberant Longitudinal Ultrasonic Waves Detected after Thermoelastic Excitation of an Aluminum Plate Having Different Paint Thicknesses Applied to the Surface. Paint Thicknesses Were (a) ~23 $\mu\text{m}$ , (b) ~38 $\mu\text{m}$ , (c) ~53 $\mu\text{m}$ and (d) ~71 $\mu\text{m}$ . ....	46
A-1.	Schematic of an SFPI .....	54
A-2.	Schematic Diagram of Model Used for Calculating the Effective Diameter of the Mirrors.....	56
B-1.	Optical Layout for Calculating the Required Fiber Diameter Needed to Collect All of the Light Transmitted by the Lens at Both the Minimum and Maximum Range of the Target.....	60
B-2.	Optical Rays Vignetted when the Target Spot is at a) Its Minimum Range, and b) Its Maximum Range .....	60
B-3.	Maximum Ray Height at Fiber Face as Focal Length of Light Collecting Lens Varies .....	62
B-4.	Absolute Value of Ray Height at Fiber Face versus Minimum and Maximum Ranges are Based on a Target Distance of 5 ft and a Scan Area of 6 by 6 ft .....	63

## LIST OF FIGURES (Continued)

Figures	Pages
B-5. Absolute Value of Ray Height at Fiber Face versus Minimum and Maximum Ranges are Based on a Target Distance of 40 Inches and a Scan Area of 4 by 4 ft .....	64
B-6. Minimum Required Fiber Diameter to Collect All of the Light versus Lens Diameter for a Fiber NA of 0.22. Lens Diameters for a Fiber Diameter of 1.5 mm are Marked .....	64
B-7. Minimum Required Fiber Diameter to Collect All of the Light versus Lens Diameter for a Fiber NA of 0.11. Lens Diameters for a Fiber Diameter of 1.5 mm are Marked .....	65
B-8. Schematic Diagram Illustrating the Relevant Parameters Used for the Analytical and Ray-Tracing Obscuration Analyses .....	66
B-9. Cassegrain System Obscuration Calculations for a 1.5 mm Core Diameter Optical Fiber and a 7 by 7 mm Optical Fiber Bundle .....	67
B-10. Cassegrain System Obscuration Calculations for a 2.0 mm Core Diameter Optical Fiber and a 7 by 7 mm Optical Fiber Bundle .....	67
B-11. Sketch of Optical Layout for Analysis of Coupling Losses when Using a Lens that Collimates the Light from the Source Prior to Passing through the SFPI..	68
B-12. Sketch of Optical Layout for Analysis of Coupling Losses when Using a Lens that Images the Source at the <i>Center</i> of the SFPI.....	70
B-13. a) Beam and Lens Diameter as a Function of the Distance between the Lens and the Center of the SFPI Cavity for a 1 mm Source with an NA of 0.2 ( $\theta = 11.537^\circ$ ). b) Beam and Lens Diameter as a Function of the Distance between the Lens and the Center of the SFPI Cavity for a 10 mm Source with an NA of 0.2 ( $\theta = 11.537^\circ$ ). In Both cases, the Lens Focal Length is Selected to Image the Source at the Center of the SFPI with a Magnification that will Minimize the Beam Size at the Output Mirror of the SFPI.....	72
B-14. Schematic Diagram of Model Used for Coupling between an Optical Fiber and the SFPI.....	73
B-15. Beam and Lens Diameter as a Function of the Distance between the Lens and the Center of the SFPI Cavity for a 1.5 mm Source with an NA of 0.38 ( $\theta = 22.33^\circ$ ).....	74
C-1. 3D Model Imported into OptiCAD for the Analysis of the Cassegrain Optical Collection System.....	75
C-2. Wire Frame Display of the Optical Configuration Used to Analyze the Obscurations in the Cassegrain Optical Collection System. The Source Shown is Modelled as an Extended Source Having a 10 mm Diameter and 25 rays are Shown Diverging from the Source with a Maximum Full-Divergence Angle of $8.7^\circ$ . Obscuration Calculations are Performed with the Source Located at Different Locations along the z-axis. The Source is Shown at $z = 38$ inches in this Model .....	76

## LIST OF FIGURES (Continued)

Figures	Pages
C-3. Comparison of Analytical Paraxial Theory and Optical Ray-Trace Model Obscuration Calculations for Cases of Vignetting by the Secondary Mirror Alone, and Vignetting by the Spider Assembly Which Holds the Secondary Mirror in Place. For each Ray-Traced Case, the Source Radiated 10,000 Rays into a Maximum Full-Divergence Angle of 8.7° .....	77
C-4. Calculations for the Full Cassegrain System Obscuration Which Takes Into Account Obscuration Caused by the Spider and Overfilling of the Optical Fiber Bundle. For the Optical Ray-Trace, the Source Radiated 10,000 Rays into a Maximum Full-Divergence Angle of 8.7° .....	78
C-5. Spatial Beam Profile Resulting from the Summation of $10^6$ rays Traced from a Gaussian Source of 5 mm Extent having a Beam Waist of 2.5 mm and Received at the Detector. (a) 2D Intensity Distribution, (b) 1D Intensity Profile with Symmetry about the Center of the Beam.....	79
C-6. Spatial Beam Profile Resulting from the Summation of 106 rays Traced from a 5 mm Diameter Lambertian Disk Source and Received at the Detector. a) 2D Intensity Distribution, (b) 1D intensity profile with Symmetry about the Center of the Beam .....	80
C-7. Calculations for the Full Cassegrain System Obscuration Which Take into Account Obscuration Caused by the Spider and Overfilling of the Optical Fiber Bundle. Several Parameter Sets, Described Below, were Analyzed and the Results Plotted .....	81
C-8. Optical Ray-Trace Calculations of the Loss of Light from a 5.85 mm Diameter Probe Laser Spot Scattered from the Target. Light Loss Results from Obscuration Caused by the Secondary Mirror and Spider Assembly and from Overfilling of a 7 mm Diameter Optical Fiber. ....	82
D-1. Sketch of Optical Rays Relevant to the Determination of the Minimum Divergence Angle, $\theta$ , of a Collimated Beam from an Optical Fiber with a Diameter, $d$ , and an $NA_f = \sin \theta_f$ .....	84
D-2. Variation of Diameter of Target Spot (S) as a Function of $\alpha$ for a 0.12 NA Fiber with Diameters Ranging from 0.1 mm to 1.5 mm.....	87
D-3. Variation of Diameter of Target Spot (S) as a Function of $\alpha$ for a 0.1 mm Diameter Fiber with NA's of 0.12 and 0.22 .....	88
D-4. Variation of Beam Diameter at Lens, $D$ , as a Function of $\alpha$ for Fiber Diameters Ranging from 0.1 to 1.5 mm. ....	88
D-5. Variation of Lens Focal Length, $f$ , as a Function of $\alpha$ for Fiber Diameters Ranging from 0.1 to 1.5 mm .....	89
D-6. Beam Diameter at Lens Versus Fiber Diameter for a 0.12 NA Fiber and a 6 mm Target Spot Diameter.....	90
D-7. Focal Length of Lens Versus Fiber Diameter for a 0.12 NA Fiber and a 6 mm Target Spot Diameter.....	91
D-8. Schematic of LACIS-R Relay Optics Configuration Used to Transmit Generation Beam from Optical Fiber.....	92

## LIST OF FIGURES (Concluded)

Figures	Pages
D-9. Schematic of the Improved Relay Optics Configuration Used to Transmit the Generation Beam from Optical Fiber to Target .....	93
D-10. Fraction of Energy in Laser Spot at Target as a Function of the Radius from Center .....	95
E-1. (a) Theoretical Magnitude and (b) Phase Response of the 1 m SFPI Operating in Reflection Mode with Mirror Reflectivities of 93% .....	97
E-2. Ultrasonic Waveforms Generated by the Piezoelectric Calibration Cell and Detected by a) the 1 m SFPI, and (b) the Stabilized Michelson Interferometer.....	98
E-3 Plot of the Deconvolved SFPI Signal Amplitude (i.e., Displacement) as a Function of the Raw SFPI Signal Amplitude. ....	99
E-4. Plot of the Pseudo-Displacement Obtained by Integration of the SFPI Signal as a Function of the Raw SFPI Signal Amplitude. ....	100

## LIST OF TABLES

<b>Tables</b>		<b>Pages</b>
1. Design Criteria for the Two SFPI Configurations .....	12	
2. Efficiency of Light Coupling into the SFPI for Selected Lenses.....	22	
3. Optical Transmission Efficiency of Relay Optics with Selected Lenses.....	25	
4. Optical Parameters of Selected Commercial Optical Fibers.....	29	
5. Fiber and Lens Parameters for Fiber Coupling the Nd:YAG Probe Laser. ....	36	
6. Fiber and Lens Parameters for Fiber Coupling the Nd:YAG Generation Laser.....	37	
7. Thermoelastic Generation Efficiency Polymer-Matrix Composites.....	44	
A-1. Comparison of Effective Mirror Diameters for Two Reflectivities.....	58	
B-1. Comparison of Beam Diameters at Different Locations .....	69	
B-2. Efficiency of Light Coupling into the SFPI for Selected Lenses.....	73	
D-1. Optical Transmission Efficiency of Relay Optics With Selected Lenses .....	95	

## **1. ACKNOWLEDGEMENTS**

This work was supported by the Air Force Wright Aeronautical Laboratories/Material Laboratory under Contract No. F33615-97-D-5271. The program was administered by Universal Technologies Corporation (UTC) for the Nondestructive Evaluation (NDE) Branch, Wright Air Force Research Laboratory Materials Directorate. The program monitor for UTC was Robert Cochoy. Dr. Curtis J. Fiedler was the program monitor for the Air Force.

## 2. INTRODUCTION

State-of-the-art integrally stiffened composite materials, manufactured for use in the next generation of commercial and military aircraft, are increasingly being used for structural components such as wings and fuselages. However, the complexity of the manufacturing processes can produce small variations in the shape of integrally stiffened composite structures. Thus, *a priori* knowledge of the nominal part shape often does not provide sufficient accuracy to allow an *automated* conventional ultrasonic inspection. Many of the advantages of laser-based ultrasonics, including its noncontacting nature and applicability to rapid scanning of contoured and integrally stiffened aerospace structures, have been described previously [1-4].

To further extend the utility of laser-based ultrasonics, the ability to quickly and directly manipulate flexible low mass optical fibers, equipped with specialized endoscopic scanning optics, makes fiber systems an attractive method for the development of remote and limited-access inspection systems that have the potential to enable 100% inspection (Figure 1). A promising approach for the implementation of a fiber-coupled inspection head is based on the use of a Cassegrain optical collection system. This approach minimizes the load-carrying requirements of the scanning and articulation assembly, and is also well suited for integration with fiber optics to allow the delivery of the ultrasonic generation and detection laser beams and reception of the detection laser beam via long lengths of optical fiber. This provides increased mobility of the laser-based ultrasound (LBU) scan head and allows the ultrasonic generation and detection lasers, and other sensitive equipment, to be housed in an environmentally controlled location which potentially can be hundreds of meters from the inspection area.

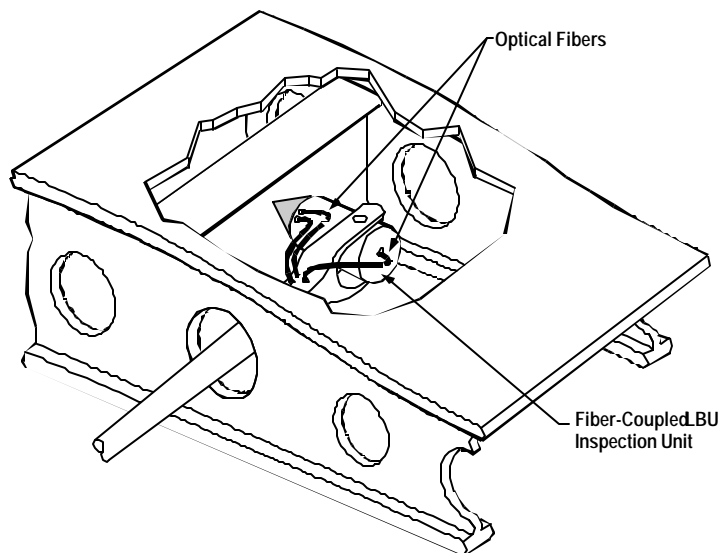


Figure 1. Concept for a Fiber-Coupled Laser-Based Ultrasound (LBU) Inspection Unit for Remote and Limited-Access Inspection Applications

## 2.1 Objective

The overall objective of this program is to determine feasible combinations of ultrasonic generation and detection lasers that would allow inspection of polymer composite or metallic structures that are located remotely from the lasers. Also to be investigated are design concepts for a scan head for a remote LBU inspection system that would allow inspection of areas with limited-access.

## 2.2 Technical Approach

Successful implementation of a fiber-coupled remote and limited-access LBU inspection system relies on two key factors. First, the capability to efficiently and robustly deliver the high peak-power generation and detection laser beams via fiber optics to the part under test must be established. Second, collection of the scattered light from the part and efficient coupling to the interferometer system via optical fiber must be implemented [5,6]. The selection of the generation and detection lasers is a critical step in the process of optimizing the LBU system signal-to-noise ratio (SNR). To maintain the ability to operate the remote scan head at distances of tens of meters from the lasers at a reasonable cost, the lasers selected must be transmitted efficiently over a standard silica optical fiber. While the long-pulse Nd:YAG ( $I=1.06\text{ }\mu\text{m}$ ) probe laser [7] is readily transmitted through standard silica optical fiber, the pulsed CO<sub>2</sub> ( $I=10.6\text{ }\mu\text{m}$ ) generation laser, which has been routinely used for LBU inspection of composite materials, is not. Furthermore, the generation laser selected should ideally result in optimum ultrasonic generation efficiency for the material under test. Consequently, an alternative generating laser has been sought that can be transmitted efficiently over standard silica optical fiber. Current solid-state laser technology is capable of producing Q-switched Nd:YAG lasers that are robust enough for industrial applications such as LBU. Both the fundamental wavelength ( $\lambda = 1064\text{ nm}$ ) and the first harmonic ( $\lambda = 532\text{ nm}$ ) of these lasers are compatible with transmission through long lengths of optical fiber. However, one potential problem with the Q-switched Nd:YAG laser is that the high energy generation-laser pulses may cause catastrophic failure of the optical fiber used to deliver the pulses. For this reason, an alexandrite laser, which is continuously tunable over the 720-800 nm wavelength range, was also investigated for this application.

A key element in the success of a fiber-based remote and limited-access system is the inspection head, which must perform multiple functions. The head must first integrate the fiber inputs from the generation and probe lasers and deliver the laser beams to a compact spot on the target. Second it must allow efficient collection of the light scattered from the target and subsequent transmission to the optical detection system. Finally the head must provide the capability to rapidly scan the beams over the target surface while minimizing the load-carrying requirements of the carrier. The approach chosen here is to use a Cassegrain optical collection system with an integrated set of relay optics for conveying the fiber-delivered generation and probe lasers to the target. Relay optics allow the two laser beams to be made collinear with each other and with the axis of the Cassegrain system. Such a system can be made compact and relatively lightweight, while efficiently collecting scattered light from the target.

The compositions of some polymer-matrix composites have been demonstrated to provide a near optimum laser-ultrasonic generation mechanism that results in ultrasonic waves propagating in

the forward direction. However, the absolute ultrasonic amplitude generated varies as a function of the materials used in the polymer-matrix composite and the *wavelength of the incident laser*. To assure success of a remote and limited-access inspection capability, a study was performed to determine the conditions for optimizing the SNR of the LBU system. Also, the effects of different types of coatings and their thickness on the generation efficiency and on defect resolution were studied. In some instances, a coating may be present on the substrates or perhaps application of a coating and then subsequent removal is an acceptable step for achieving a successful inspection. In the case of polyurethane paints, a solvent is required to remove the coating. Experience has shown that this can raise environmental issues with regard to disposal of the stripping solution. A better approach seems to be the use of a water-based strippable coating, which can be easily peeled from the substrate once the inspection has been completed. However, it is important to know the relative generation efficiencies that are provided by each of the coating types when applied to different substrates and irradiated with different laser wavelengths. This will allow the LBU SNR, and thus defect detectability, to be maximized in any given application.

### **2.3 Major Accomplishments**

A list of major accomplishments achieved under this research program are outlined below:

- Completed design, implementation, and proof-of-concept demonstration of a fiber-based Cassegrain optical scanning system .
- Demonstrated optical generation and detection with the fiber-based Cassegrain optical scanning system over 100 m lengths of optical fiber.
- Successfully delivered high peak-power, Q-switched Nd:YAG laser pulses (>45 mJ/pulse at 532 nm) through optical fiber in a robust manner.
- Established the absolute thermoelastic generation efficiency for four different laser wavelengths and eight different material/boundary conditions.

### 3. THE FIBER-BASED CASSEGRAIN OPTICAL SCANNING SYSTEM

#### 3.1 Introduction

This program was preceded by the LACIS-R (Large Area Composite Inspection – Rockwell) program [8] whose purpose was to investigate the feasibility of using laser-based ultrasound technology for the rapid inspection of polymer-matrix composite materials. As part of that program, a Cassegrain optical system was fabricated and assembled with a spherical Fabry-Pérot interferometer (SFPI) that was built at Rockwell. In this system the generation and probe lasers were delivered to the target via optical fibers. The light scattered from the target was collected with a Cassegrain optical system and coupled into the SFPI via a coherent optical fiber bundle.

This system was tested using an alexandrite laser for generation and a long pulse Nd:YAG probe laser. The target was a ~8 mm thick black graphite/epoxy panel. The Cassegrain scan head was oriented such that the generation and detection lasers were incident at an angle of ~30°. Figure 2. shows the resulting ultrasonic signal, which clearly shows the longitudinal wave detected after reflection from the backwall of the part. The detected signal had a smaller amplitude than expected based on previous work with CO<sub>2</sub> and Nd:YAG generating lasers [9] and thus averaging of 50 signals was required to obtain the displayed signal (Figure 2).

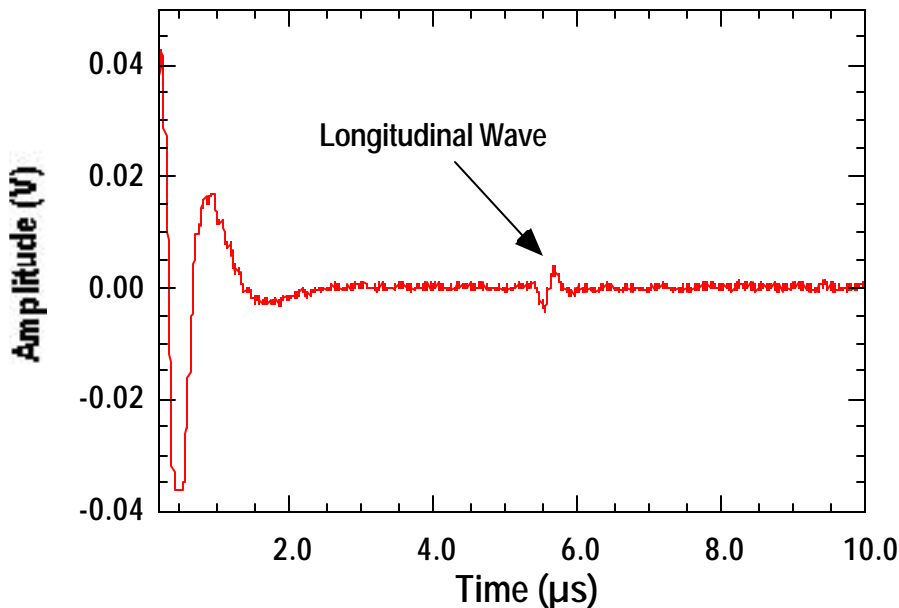


Figure 2. Detection of Ale xandrite Laser-Generated Ultrasonic Signals in a Black Graphite/Epoxy Panel Using the Fiber-Coupled Cassegrain Optical Scanning System

The signal amplitude is very low compared to the signal obtained from this same target using either the CO<sub>2</sub> or Nd:YAG generating lasers and a simple lens to couple light into the SFPI. This suggests that there is a problem with the system. A check of the system for a failed or misaligned component revealed no problem. This leaves two possibilities. Perhaps the thermoelastic generation efficiency of the alexandrite laser is much less than that of the CO<sub>2</sub> and Nd:YAG

generating lasers. Or perhaps the Cassegrain optical system is not effectively coupling light from the target to the SFPI through the fiber bundle.

Much of this report is concerned with the investigation of these two issues. A study of the thermoelastic generation efficiency of four different lasers with a variety of polymer-matrix composite materials is presented in Section 5. This section, concerning the fiber-based Cassegrain optical scanning system, contains detailed studies of the performance of the system and its optimization. Here the term “Cassegrain optical scanning system” includes the optics required to deliver the lasers to the target and the optics required to collect the light scattered from the target and effectively couple it into the SFPI. These functions provide a separation of the design process into beam delivery optics and beam collection optics. Although these two functions do not overlap, they are connected by the need to have the laser beams focused to a spot at the same place where the Cassegrain is focused. Further, the étendue for the system is defined by the SFPI, which affects the target spot size as well as the diameter of the primary collection mirror. Also included are the stages and servos used to scan the beams over the target.

### **3.2 Cassegrain Scanning System Design - Concept and Issues**

A Cassegrain optical system, which dates back to the late 17<sup>th</sup> century [10], is defined as a two-mirror configuration in which the secondary mirror is located between the primary mirror and the image plane of the primary mirror. This system is most commonly used for astronomical telescopes which have the object at infinity. However, for use as the collection optics for an LBU system, operation is required with object distances of 1 to 2 meters. It has the advantage of combining both the beam scanning and light collecting functions of the LBU system into a single compact unit. The concept for the Cassegrain scanning system is shown in Figure 3, with a more detailed schematic of the collection optics depicted in Figure 4 and a photograph of the system shown in Figure 5. In Figure 5, the Cassegrain subassembly relay optics are seen mounted beneath the Cassegrain scan head. On entering the subassembly relay optics the generation and probe laser beams are represented by red and green laser beams, respectively. On exiting the subassembly relay optics, the yellow beam represents the propagation path of the generation and probe laser beams after they have been combined within the Cassegrain subassembly relay-optics. The combined beams are reflected off a beam steering mirror mounted to the spider assembly and directed to the part under test. A diffuse cone of probe laser light is then seen entering the Cassegrain scan head after being scattered from the target. The key requirement of the design was to maximize the collection of the light that is diffusely scattered from the target as the Cassegrain scan head deflects the probe laser beam over the target surface. The optical scanning losses vary with the distance of the primary mirror from the target surface (range) as the probe laser beam is deflected from the center to the periphery of the scan area. The main losses are caused by overfilling of the primary mirror collection aperture, blockage of the incoming scattered probe laser light by the secondary mirror and spider assembly of the Cassegrain system, and overfilling of the receiving optical fiber.

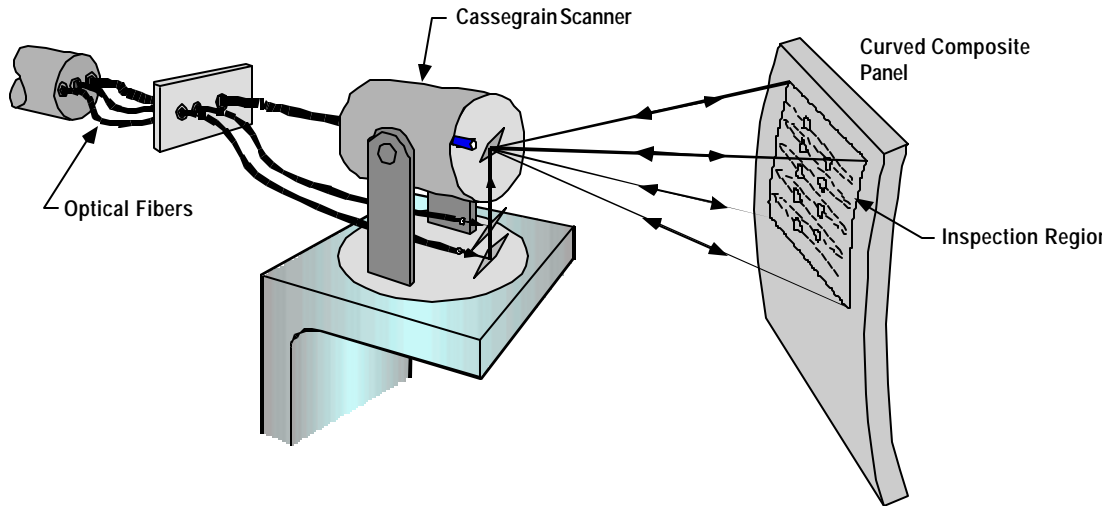


Figure 3. Concept for the Fiber-Coupled Cassegrain Optical Scanning System

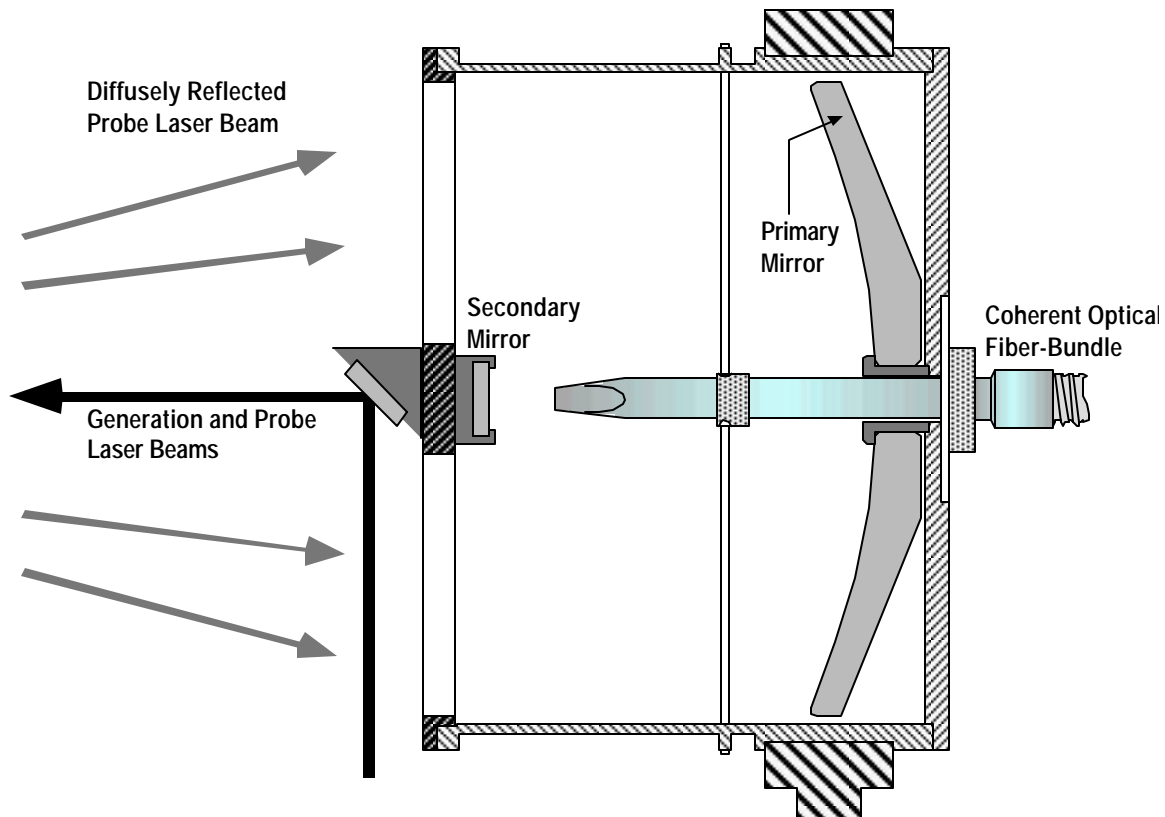


Figure 4. Schematic Diagram of the Cassegrain Optical Collection System

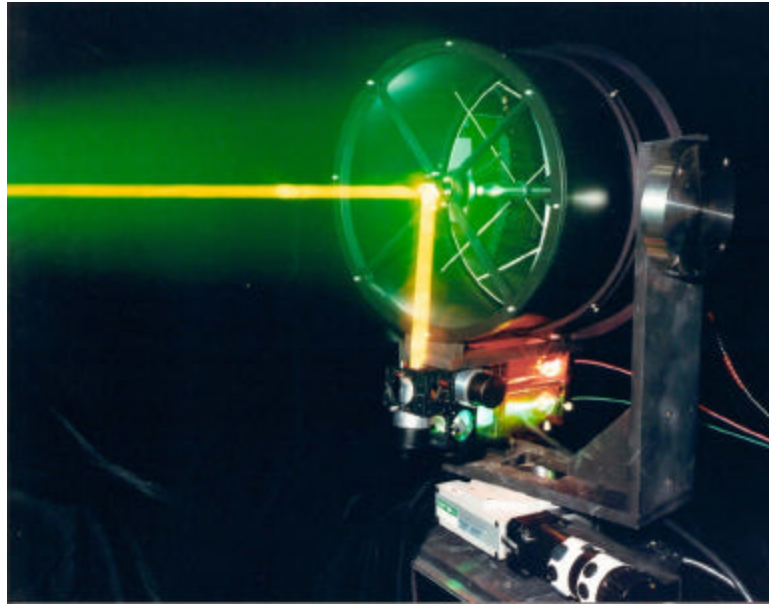


Figure 5. Photograph of the Cassegrain Optical Collection System

The LACIS-R Cassegrain optical collection system design employed a 10 inch diameter (254 mm) spherical primary mirror which has a focal length of 6.25 inches (~160 mm). The secondary mirror is axially located 6.017 inches (~153 mm) from the apex of the primary mirror. The optical collection head is designed to accommodate two interchangeable secondary mirrors having diameters of 1.115 inches (~28.3 mm). A flat mirror permits the unit to be used at a short range of ~32–48 inches (~0.80–1.20 m), while a 1.75 inch (~45 mm) focal length convex mirror allows operation at a longer range of ~56–66 inches (~1.42–1.68 m). The secondary mirrors may be interchanged without adjustment of any other optics. This configuration allows the collection optics to be mounted in an 11 inch diameter (~280 mm) housing, which is ~8 inches (~205 mm) long. Scanning of the Cassegrain scan head is performed in both azimuth (fast axis) and elevation (index axis), with an angular range of  $\pm 45^\circ$  in both azimuth and elevation. The performance of the azimuthal stage is the most critical since this is the fast scan axis and has to accelerate the full inertia of the Cassegrain housing from a standstill to a velocity of  $45^\circ/\text{s}$  in an angular increment corresponding to only a few pixels of the field-of-view that is being scanned. To accomplish this, the housing was designed to have a minimum moment of inertia so that the torque requirements of the azimuthal drive motor were minimized. Under full load, servo parameters were chosen that enabled the stages to accelerate smoothly with minimum following error and without excessive overshoot. The encoder used with this stage has a resolution of 1000 counts/degree. It is possible to accelerate the stage at  $2 \times 10^6$  counts/s<sup>2</sup> while maintaining smooth operation. At the furthest operating range of ~1.68 m, this acceleration dictates that the scan head achieve its full speed in a distance of 21.3 mm, which corresponds to a little over 2 pixels, assuming a pixel size of 10 mm and a  $\pm 0.6$  m scan field. At the near range of ~1.20 m, the scan head achieves its full speed in a distance of 18.7 mm. High-speed performance of the servo loop associated with the elevation stage was not required since it was used chiefly as an index axis during the raster scans. Accordingly, the maximum acceleration was not critical since index moves were so short that full speed could not be achieved. The azimuthal motor and controller

provide an encoder output that is programmed to give a TTL signal when the scanner arrives at the target position. This capability allows synchronization of the Cassegrain scanner position with the firing of the generating and probe lasers, which is essential for correct data acquisition and spatial registration.

A coherent optical fiber bundle was used in the LACIS-R Cassegrain system to couple light from the focal plane of the Cassegrain collection optics to the input lens of the SFPI. It was constructed using 8  $\mu\text{m}$  core diameter fibers and had a minimum bend radius of  $\sim$ 100 mm, which was more than adequate to follow the motion of the Cassegrain scan head during a raster. The bundle has an actual area of 7.5 mm x 7.5 mm which provided a 0.25 mm margin around the perimeter to allow for edge variation and trimming breakage. The high quality region was specified as a 7.0 mm x 7.0 mm area and contained a total of 469,225 fibers. The packing fraction, defined as the ratio of the total fiber core area to total surface area, was 48% and the transmittance of the coherent optical fiber bundle was measured to be  $\sim$ 40% ( $\lambda=1064 \text{ nm}$ ). The additional 8% loss was attributed to Fresnel and fiber losses. The NA (numerical aperture) of the individual fibers and hence of the fiber bundle was specified as 0.66, although experimentally the effective NA of the fiber bundle was measured to be  $\sim$ 0.6. Although a coherent optical fiber bundle preserves spatial coherence, phase coherence is not preserved. However, experiments verified that phase incoherence of the coherent optical fiber bundle did not appear to introduce any deleterious effects, and ultrasonic signals were successfully detected after an ultrasonically phase modulated light beam was transmitted through the coherent optical fiber bundle and imaged through the SFPI. The optical fiber bundle was mounted on the back plate of the Cassegrain housing (Figure 4) with an assembly that allowed precision adjustment of its position over  $\pm 2.5 \text{ mm}$ .

Ultimately, light collected by the receiving optical fiber (bundle or single fiber) must be coupled into the optical detection system for demodulation and ultrasonic wave detection. Therefore, for optimization of light collection efficiency, it was important to ensure that the Cassegrain optical system design was commensurate with the optical detection system. The term étendue, or light-gathering power, which is generally used to characterize the light-collection efficiency of the SFPI, is an optical invariant that ensures that optical power is conserved. The method for calculating the étendue of an SFPI is summarized in Appendix A, where it is shown that the étendue is dependent on the length, mirror reflectivity and operating wavelength of the SFPI. The SFPI used in this program is 1 m long, has a mirror reflectivity of 93% and operates at a wavelength of 1064 nm, which results in an étendue of  $0.4856 \text{ mm}^2 \cdot \text{sr}$ . This limits the maximum full-divergence angle of scattered rays from a 5.85 mm diameter probe beam at the target to  $\sim 8.7^\circ$ .

In addition to conserving étendue via the maximum convergence angle and spot size, the focused output of the Cassegrain optical collection system must also be coupled into an optical fiber. The fiber is located at the prime focus of the optical collection system and provides a flexible transmission path to the optical detection system. As the system is scanned, the range to the target changes, and, therefore, the position of the prime focus changes. The range and angle of incidence (for inspection of a flat panel) are at a minimum when the optical axis of the

Cassegrain scanner is perpendicular to the target surface, and are a maximum when it is pointed at the corners of the inspection area. It is important to minimize the optical collection loss at the receiving optical fiber during a scan. Two approaches may be pursued. Either the distance between the fiber entry face and the secondary mirror can be dynamically changed to track the image plane as the Cassegrain scan head deflects the probe laser beam over the inspection area, or the distance can be fixed at an optimum location for a specified operational range and the fiber diameter can be increased. For the LACIS-R Cassegrain system design, we chose to fix the distance between the fiber entry face and the secondary mirror. To extend the collection efficiency over a useful operational range, the 7 mm x 7 mm optical fiber bundle, described elsewhere, was selected. Experimentally, the position of the input face of the optical fiber bundle was adjusted relative to the prime focus of the Cassegrain optical system to equalize the received laser power measured at either end of the operating range. The location of the fiber bundle input face was nominally 125 mm from the apex of the primary mirror, and the output end of the optical fiber bundle was coupled into the SFPI. Subsequent analyses and experimental observations have indicated that the use of the large NA fiber bundle imposes some serious limitations on the amount of light that can be coupled into the SFPI (see Section 4.3.3.2). For this reason, the use of a single, large-core, optical collection fiber has also been investigated.

When using a single large-core fiber with the distance between the secondary mirror and the fiber entry face is fixed, it is important to know the relationship between the fiber parameters (diameter and NA), the lens or lens system parameters (diameter and focal length) and the optimum placement of the fiber entry face. This allows calculation of the minimum fiber diameter that can be used and still collect 100% of the light at both the minimum and maximum target ranges. This was done for the system shown in Figure 6. The parameters that influence the required diameter of the optical fiber are the range to the target, the diameter of the light source at the target, the diameter of the collection lens, and its focal length. The source is assumed to be radiating isotropically. For this analysis, a simple lens which has an equivalent diameter and focal length has been substituted for the Cassegrain optics.

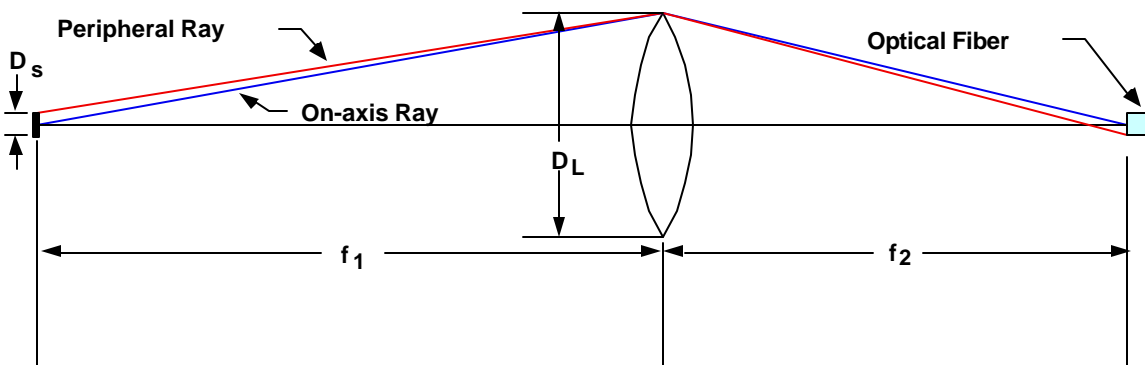


Figure 6. Optical Layout for Calculating the Required Fiber Diameter Needed to Collect All of the Light Transmitted by a Lens at Both the Minimum and Maximum Range of the Target

The details of the calculations are provided in Appendix B. As expected, there is a relationship between the minimum lens focal length and the maximum ray height at the fiber face

(Figure 7). To minimize the maximum ray height, the focal length is chosen to have the minimum value allowed by the fiber NA. It is then possible to calculate the minimum fiber diameter as a function of the lens diameter. Before doing this there are several parameters that must be specified in the equations. A value of 5 mm is selected for the target spot diameter. Since the curves are dependent on the values of the maximum and minimum target ranges, the results were calculated for four sets of target ranges. Finally the fiber NA is selected to be 0.22 for the curves presented in Figure 8 and 0.11 for the curves in Figure 9. For the scan range that is relevant to the LACIS-R system, i.e., a minimum range of 40 inches and a scan area of 4 ft x 4 ft, the maximum lens diameter that can be used with a 1.5 mm diameter fiber decreases from ~79 mm to ~66 mm as the NA decreases from 0.22 to 0.11. This implies that the étendue also decreases. At the maximum range of 1332 mm, the étendue for the system is only  $0.054 \text{ mm}^2 \cdot \text{sr}$ . This is significantly less than the  $0.4856 \text{ mm}^2 \cdot \text{sr}$  étendue of the SFPI and shows that the system must be capable of dynamically moving the fiber face as the range changes to realize its maximum sensitivity during scanning.

The results of the analysis for optical collection of light reflected from the target show that it is advantageous to have a fiber with a large diameter and NA to obtain a large areal scan range without dynamically refocusing. Even so, severe limits are placed on the maximum lens diameters that can be used (and therefore the maximum étendue) if practical-sized fibers are to be used ( $\leq 1.5$  mm core diameter). The requirement for relatively small lens diameters restricts the étendue of the system and, therefore, its sensitivity. If dynamic refocusing is used, larger lenses can be used to obtain a greater étendue. The system built for this program does not have a ranging system that would allow us to track the image plane, as the range to the target varies during a raster. For purposes of demonstrating an all fiber system, the target range is held constant so that the full étendue of the SFPI can be realized. For systems with a ranging system, the results of these calculations should be used to select the lens focal length in order to relax the accuracy requirements of the range finder.

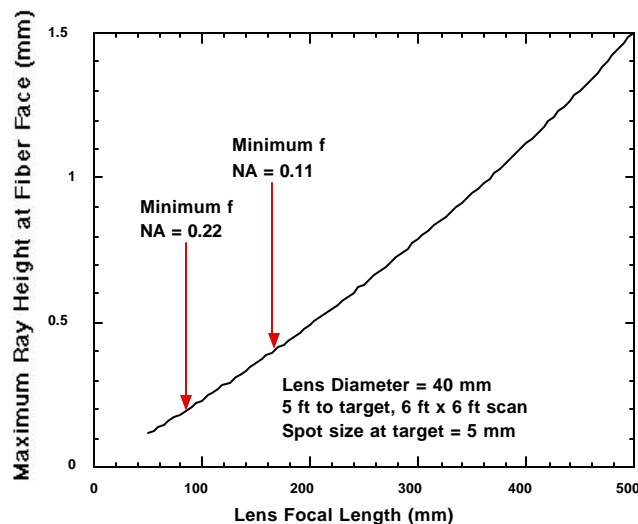


Figure 7. Maximum Ray Height at Fiber Face as Focal Length of Light Collecting Lens Varies

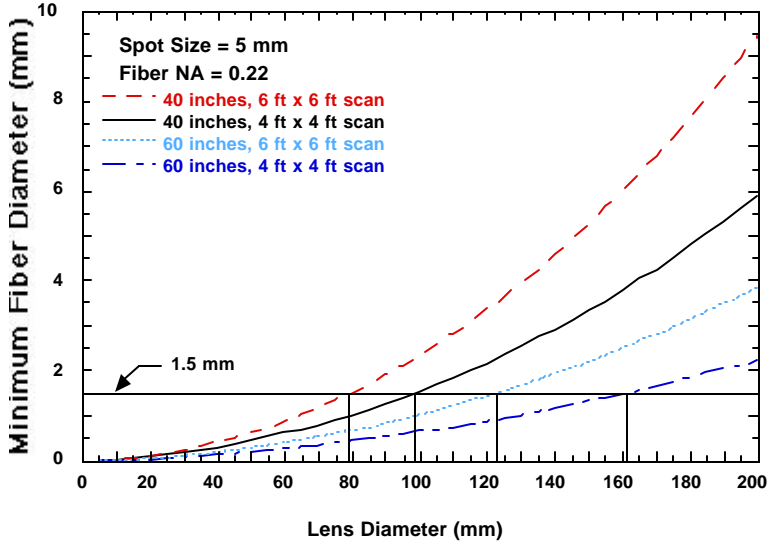


Figure 8. Minimum Required Fiber Diameter to Collect All of the Light versus Lens Diameter for a Fiber NA of 0.22 (Lens Diameters for a Fiber Diameter of 1.5 mm are Marked.)

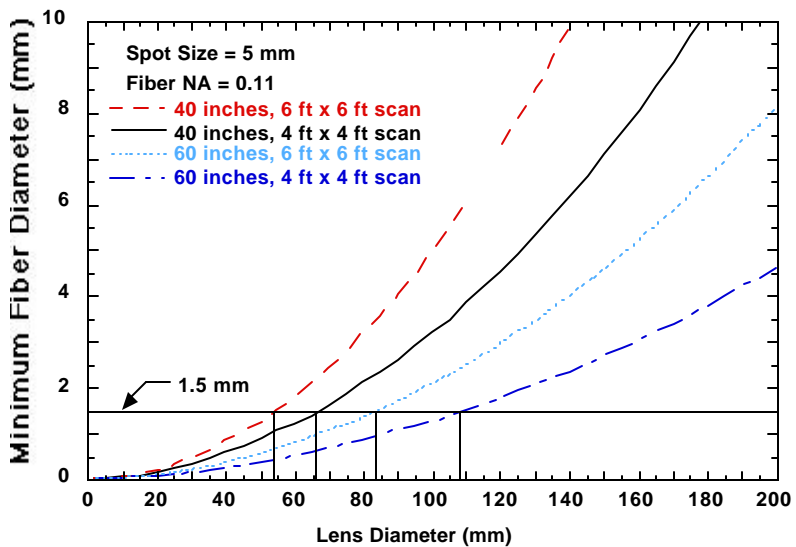


Figure 9. Minimum Required Fiber Diameter to Collect All of the Light versus Lens Diameter for a Fiber NA of 0.11 (Lens Diameters for a Fiber Diameter of 1.5 mm are Marked)

### 3.3 Optimization of Laser Beam Coupling from the Target to the Optical Detection System

A portion of the probe laser light scattered from the illuminated target is collected by the primary mirror of the Cassegrain optical collection system and refocused for coupling into the collection optical fiber. Ideally, using either of the methods described in Section 3.2, the optical collection fiber is located at the prime focus of the system and provides a flexible transmission path to the optical detection system for demodulation and ultrasonic wave detection. Although the LACIS-R system makes use of a fiber bundle, for remote and limited-access applications it will ultimately

be necessary to transmit the collected probe laser light over many meters of optical fiber. In this case, the use of a coherent fiber bundle becomes unrealistic and prohibitively expensive. Thus, optical analyses and experimental measurements were also performed for the case of a single, large-core, receiving optical fiber used in the Cassegrain optical collection system. To fully optimize the system sensitivity it was necessary to assess the light-collection and coupling efficiencies for the following:

- Scattered light reflected from the target, collected by the Cassegrain primary mirror and relayed via the secondary mirror to the entry face of the collection fiber.
- Light exiting the output face of the collection fiber and coupled into the SFPI.

### 3.3.1 Determination of Light Collection Efficiency of the Cassegrain System

The obscuration of the light that is collected by the Cassegrain optics is primarily dependent on the range and on the maximum allowed full-divergence angle from the target spot. The LACIS-R Cassegrain optical scanning system required  $\pm 0.6$  m scan area and a 10 mm diameter laser spot. Light scattered from the target that could be successfully coupled into the 1m length SFPI was contained within a solid angle corresponding to the maximum étendue of the SFPI. At the time the design was being established, the SFPI had not been fully tested, but utilized mirrors which were 81% reflecting and the incident probe laser wavelength was 1064 nm, resulting in a system étendue of  $1.4192 \text{ mm}^2.\text{sr}$ . Thus for a 10 mm diameter spot size, the maximum full-divergence angle was limited to  $\sim 8.7^\circ$ . Light from such a source could be collected without vignetting by a 10 inch primary mirror at a range up to  $\sim 63$  inches ( $\sim 1603$  mm). Subsequent to completion of the original design and fabrication of the Cassegrain system, aberrations were discovered in the 81% reflectivity mirrors that were being used in the SFPI cavity. These aberrations severely reduced the étendue of the system and limited the useful diameter of the mirrors to only  $\sim 10$  mm in the center of the 50 mm diameter mirror. When new mirrors were ordered, the mirror reflectivity was increased to 93%. The increased reflectivity had the favorable effect of decreasing the ultrasonic receiver bandwidth from 10 MHz to 3.5 MHz and increasing the finesse. The narrower bandwidth is more appropriate for the inspection of composites, and the sensitivity of the SFPI is proportional to the finesse. However, this change had the unfavorable effect of decreasing the étendue from  $1.4192 \text{ mm}^2.\text{sr}$  to  $0.4856 \text{ mm}^2.\text{sr}$ . Since the Cassegrain system had already been fabricated, the best option for changing the system design to maintain optimal operation was to maintain the same full-divergence angle, thereby utilizing the primary mirror diameter to its full design extent at the maximum operating range. This required the probe laser beam size at the target to be reduced to 5.85 mm to conserve étendue. A summary of the relevant design criteria based on the SFPI mirror reflectivity is given in Table 1.

**Table 1. Design Criteria for the Two SFPI Configurations**

SFPI Mirror Reflectivity	Limiting Étendue (1064 nm)	Optimum Spot Size (8.7° Full Divergence Angle)	Maximum Range Before Overfilling Primary Mirror
81%	$1.4192 \text{ mm}^2.\text{sr}$	10 mm	1603.83 mm
93%	$0.4856 \text{ mm}^2.\text{sr}$	5.85 mm	1631.11 mm

### 3.3.1.1 An Optical Ray-Tracing Analysis

When the original design of the Cassegrain optical system was performed, as part of the LACIS-R program, a paraxial ray analysis was used. However, the increasing sophistication of optical design and optical ray-tracing software packages allows the simple analytical theory to be extended, thereby allowing for more accurate and detailed modeling of the actual system design. Figure 10 shows a schematic diagram illustrating the relevant parameters used for both the analytical and optical ray-tracing obscuration analyses. A detailed description of the optical ray tracing analysis is presented in Appendix C and the most important results are summarized below:

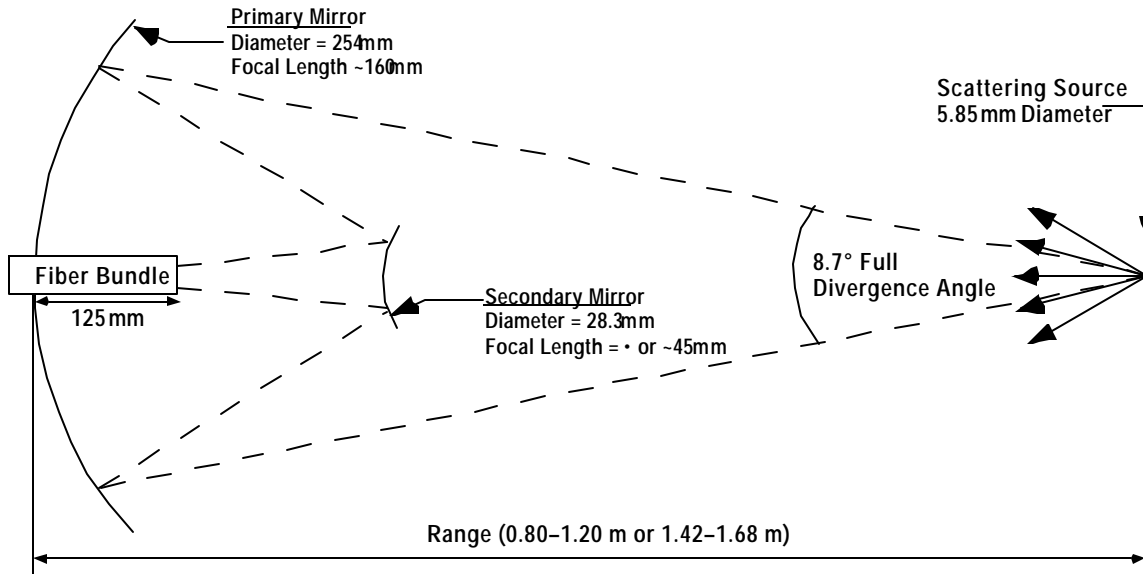


Figure 10. Schematic Diagram Illustrating the Relevant Parameters Used for the Analytical and Ray Tracing Obscuration Analyses

Assuming a Lambertian source, obscuration losses caused by overfilling an optical fiber that is *stationary* relative to the Cassegrain mirror system were calculated for fibers having diameters of 1, 2, 5 and 7 mm, and the results are compared in Figure 11. The range was consistent with scanning the system  $\pm 45^\circ$  over a flat target with scan field dimensions of  $\pm 0.6$  m in both the horizontal and vertical directions. An obscuration of 1.0 means that no light rays reached the detector. This was caused at near range by the secondary mirror/spider assembly completely blocking the rays radiating from the source, although the analytical paraxial theory did not include the obscurations caused by the spider assembly. From Figure 11, it is evident that the light transmitted into the 1.0 mm diameter fiber is always less than the light transmitted into the 7 mm fiber bundle even at the optimum range. This implies that the spot size always slightly exceeds the fiber diameter. Away from the optimum range of  $\sim 1150$  mm, the obscuration increases rapidly as the blur circle greatly exceeds the diameter of the fiber and increases the loss. This results in a much-reduced optimum operational range compared with the optical fiber bundle, which was anticipated since the fiber remains stationary in this analysis. Also, for the 2, 5 and 7 mm diameter fibers, it was observed that the obscuration abruptly increases from the value determined by loss at the secondary mirror alone to an increased value when the blur circle eventually exceeds the diameter of the fiber and also further increases the loss. The optimum

operational range for the 7 mm diameter fiber, where the obscuration was at a minimum, when using the flat secondary mirror configuration was calculated to be from ~31.5 inches to ~47 inches (~0.8 m to ~1.2 m) for a 5.85 mm diameter extended source.

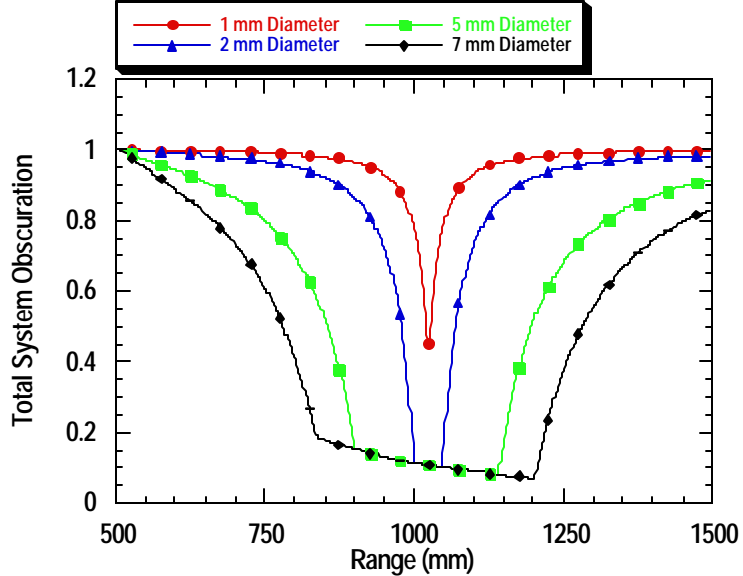


Figure 11. Analytical Paraxial Calculation of the Loss of Light from a 5.85 mm Diameter Probe Laser Spot Scattered from the Target. Light Loss Results from Obscuration of Incoming Light by the Secondary Mirror and from Overfilling of 1, 2, 5 and 7 mm Diameter Optical Fibers.

Figure 12 shows optical ray-trace calculations for the full Cassegrain system obscuration analysis (using the flat secondary mirror) which take into account obscuration caused by the secondary mirror/spider assembly and overfilling of the optical fiber bundle. Both Lambertian and Gaussian spatial source distributions were modeled (Appendix A) using rays that radiated from a 5.85 mm diameter source into a maximum full-divergence angle of 8.7°. These results were also compared with the original analytical model for a 7 mm diameter fiber (Figure 11). The results are similar for both analytical and optical ray-trace models. The main difference is slightly increased loss associated with the ray-trace models, which would be expected since the additional obscuration caused by the spider assembly is accounted for. The maximum loss of light at each extreme of the near range configuration is about 10% to 20%, which is consistent with experimental measurements and is within acceptable limits for this type of system. Small differences are also evident in the Lambertian and Gaussian source optical ray-trace models, but these typically occur outside of the operational range for the system. Furthermore, in practice it is likely that after the beam exits the multimode delivery fiber, the original Gaussian spatial intensity profile will have been homogenized to some degree. To investigate this aspect of the Cassegrain operation would require experimental intensity profile measurements to be obtained of the Nd:YAG probe laser at the target surface to determine the beam waist and also compare the uniformity of the beam intensity profile at the input and output of the optical fiber. However, based on the results of Figure 12 it is expected that the actual beam profile would yield very similar results to the case presented for the Lambertian disk source. Thus, the additional complication of determining the exact probe laser beam profile was not pursued and the Lambertian disk source was used for all subsequent optical ray-trace analyses.

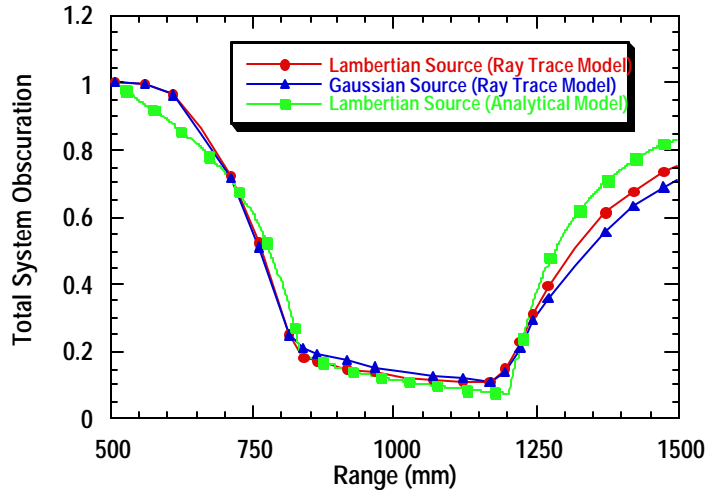


Figure 12. Optical Ray-Trace Calculations of the Loss of Light from a 5.85 mm Diameter Probe Laser Spot Scattered from the Target (Light Loss Results from Obscuration Caused by the Secondary Mirror/Spider Assembly and from Overfilling of a 7 mm Diameter Optical Fiber)

The final step of the obscuration analysis was to extend the model to determine the amount of light that propagated through the collection fiber, thereby taking into account any skew rays that might exceed the NA of the collection fiber and thus be lost in the fiber cladding. Figures 13 and 14 compare calculations for the full Cassegrain system obscuration analysis (near range configuration that uses the flat secondary mirror) at both the input and output of 1.5 and 2.0 mm diameter optical fibers having an NA of 0.38. For the 1.5 mm diameter optical fiber, Figure 13 shows that a maximum of ~80% of light is transmitted to the input face of the fiber, with an additional ~14% loss after propagation through the fiber. Similar analyses are shown for a 2 mm diameter fiber (NA=0.38) in Figure 14. At the optimum range of ~1150 mm, the 2-mm fiber is large enough to collect all of the light as evidenced by the fact that the data intersects the curve for the fiber bundle. Also, ~90% of the scattered light reached the input to the fiber with an additional ~16% loss after propagation through the fiber. It should be noted that these analyses have excluded any Fresnel losses at the fiber entry and exit faces. An accurate analysis of the obscuration at the output of the fiber bundle was not investigated. However, the packing fraction for the fiber bundle is the dominating source of loss with a measured transmittance of ~40% (Section 3.2). The large NA of the fiber bundle would likely ensure that the skew rays were collected without loss.

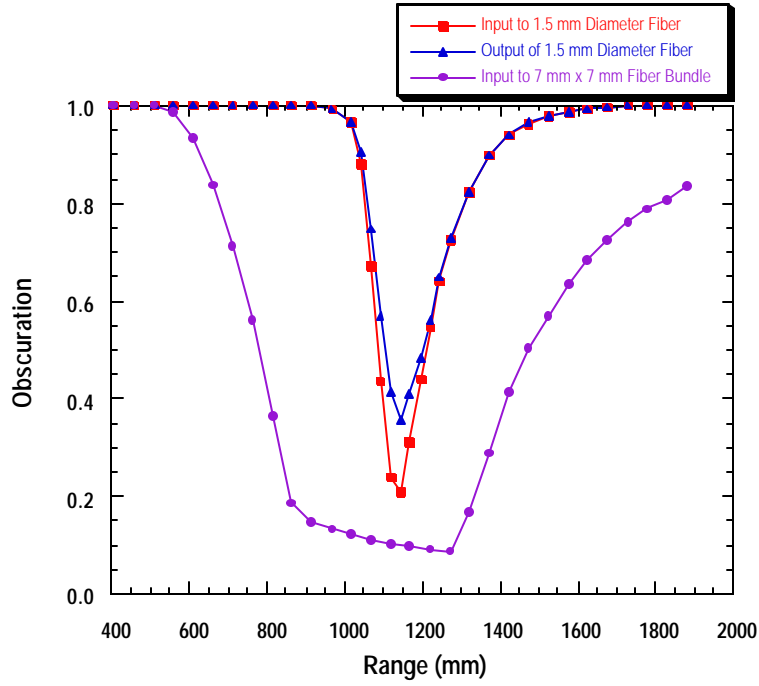


Figure 13. Cassegrain System Obscuration Calculations for a 1.5 mm Core Diameter Optical Fiber (NA=0.38) and a 7 mm x 7 mm Optical Fiber Bundle

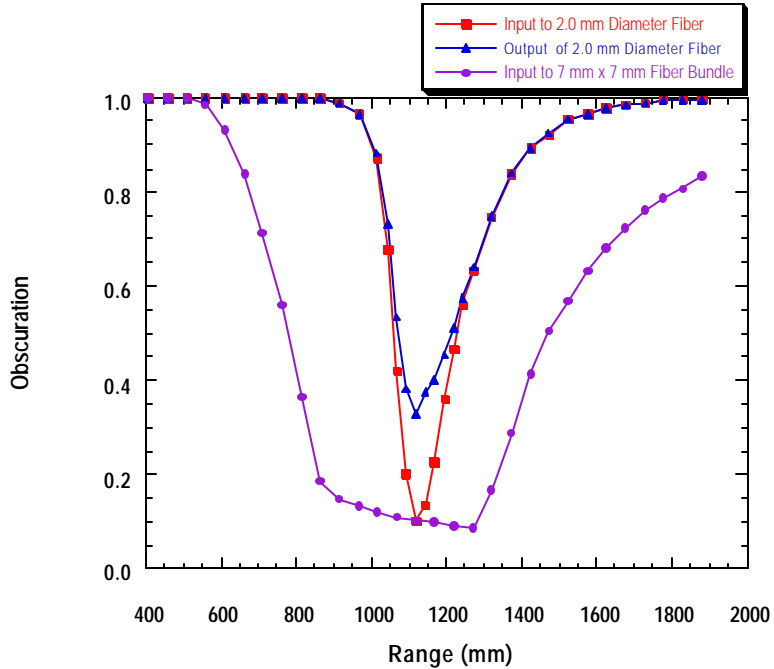


Figure 14. Cassegrain System Obscuration Calculations for a 2.0 mm Core Diameter Optical Fiber (NA=0.38) and a 7 mm x 7 mm Optical Fiber Bundle

For completeness, Figure 15 shows the spatial characteristics of the probe laser beam incident on the entry face of the receiving optical fiber as a function of three different operating ranges. The square region is equivalent to the 7.5 mm x 7.5 mm full entrance aperture of the optical fiber bundle, and each ray that is incident on the entrance aperture is marked with a cross. The main

source of obscuration is the secondary mirror/spider assembly, which is most evident in the spatial distribution of the received beam at  $z = 34$  inches. These results compare favorably with visual observations.

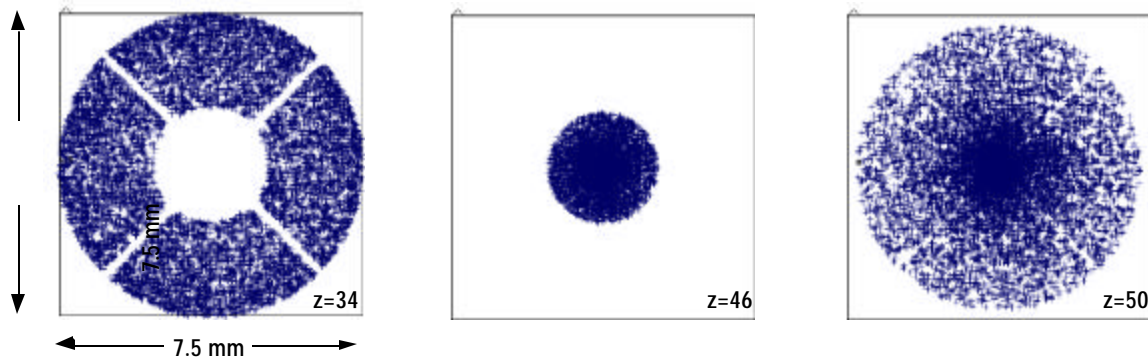


Figure 15. Spatial Characteristics of the Probe Laser Beam Incident on the Entry Face of the Optical Fiber Bundle at Ranges of 34, 46 and 50 Inches

### 3.3.1.2 Experimental Measurements

A quantitative comparison was made of the relative optical power collection efficiencies of the Cassegrain and galvanometer mirror [1] scanning systems and of the variation in their sensitivities over a scan range of  $\pm 5^\circ$  in both X and Y directions. The limiting apertures of the galvanometer and Cassegrain systems had diameters of 50 and 254 mm, respectively, and the path lengths between the limiting apertures and the sample were equalized. The output optical power from each of the optical scanning systems was then measured using a large-area photodetector located at the *input* to the SFPI. Figure 16 shows the resulting optical power contour plots that were obtained from the two scanners when using a white-painted graphite/epoxy panel as a scattering test target. For the galvanometer mirror scanning system (Figure 16a), there was a large amplitude on-axis component, which corresponds to the specular reflection from the sample. At angles greater than  $\sim \pm 0.6^\circ$ , the specular component is vigneted by the limiting aperture in the scanning system. Beyond this angle, the diffuse optical wavefield has approximately uniform amplitude over the  $\pm 5^\circ$  angular range investigated. Since the galvanometer mirror system collection aperture remains fixed as a function of scan angle, the effective collection aperture is reduced as the scan angle increased. In contrast, the image obtained with the Cassegrain scanning system (Figure 16b) has a region of low amplitude in the central portion of the image, which corresponds to the zero angle of incidence position. This occurs because the beamsteering mirror that is attached to the back of the secondary mirror (Figure 4) blocks the specular reflection. Thus for the Cassegrain system, only the diffuse component is detected in the on-axis configuration.

As the scanner is moved off-axis, to sufficiently large angles, the specular component is no longer blocked, but is collected by the primary mirror of the Cassegrain system and is reflected into the coherent optical fiber bundle. Within the specular component, regions of lower amplitude are clearly visible as  $45^\circ$  lines crossing the central portion of the surface plot (Figure 16b). These regions correspond to the spokes of the spider that hold the secondary mirror in place and correlate well with the optical ray-trace results of Figure 15. Since the specularly

reflected beam is larger in diameter than the spokes, only partial extinction occurs in these regions. At angles greater than  $\sim\pm 2.25^\circ$ , the specular component is vigneted by the Cassegrain collection optics. Note that this angular range is  $\sim 3.7\times$  greater than that of the galvanometer system, due to the larger collection aperture of the Cassegrain system. Further, since the axis of the Cassegrain optics points at the target, its effective collection aperture remains the same during a scan. Beyond this angular range, the diffuse optical wavefield is detected which, again, has an approximately uniform amplitude over the  $\pm 5^\circ$  angular range.

Although not evident in the normalized images of Figure 16, the Cassegrain system exhibits an  $\sim 16.4\times$  increase in the optical power collected at the scan area extremities when compared with the galvanometer scanner. This value accounts for the optical losses in each system, and is thus an absolute measure of the improvement in optical power collection efficiency as measured at the *input* to the SFPI. This result suggests that the detected amplitude of the ultrasonic waves collected from the extremities of the scanned area by the Cassegrain scanner would be increased in amplitude by  $\sim 24$  dB, if all of the light collected was successfully matched into the SFPI. Thus use of the Cassegrain collection optics should result in a significant improvement in SNR. In addition, based on this assumption, the measurements indicate that the expected variation in ultrasonic signal amplitude that was caused by reflectivity and collection efficiency variations is 47 dB for the galvanometer scanner, but only 22 dB for the Cassegrain scanner. The Cassegrain-detected signals thus permit operation with detection electronics having smaller dynamic range requirements for operation over the same scanned area. This is advantageous since it permits an additional 25 dB of dynamic range for signal variability caused by ultrasonic attenuation within the part. Further, when using an 8-bit waveform digitizer with a dynamic range of only 48 dB, the gain setting of the digitizer is less critical, and saturation of the amplifier inputs may be more easily avoided throughout the full scan range without the need for automated dynamic intensity control of the delivered probe laser beam energy.

### 3.3.1.3 Summary

The results of the obscuration analyses show that without dynamically refocusing the optical collection system (i.e., when the receiving fiber is to remain stationary), it is advantageous to have a fiber with a large diameter and NA to maximize the areal scan range. For practical implementation of the Cassegrain optical scanning system we have considered design concepts for optical collection using either a 7 mm x 7 mm diameter optical fiber bundle or a single optical fiber with a maximum diameter of up to 2.0 mm. Full obscuration analyses, which include the obscuration by the secondary mirror/spider assembly and overfilling of the collection fiber, show that a 1.5 mm diameter fiber (NA = 0.38) will allow  $\sim 80\%$  of the light scattered from a 5.85 mm diameter spot within a full-divergence angle of  $8.7^\circ$  to be incident on the fiber entry face. However, modeling in OptiCAD allowed the output of the fiber to also be calculated, thereby taking into account any skew rays that might exceed the NA of the optical fiber and therefore be lost. This resulted in an additional  $\sim 14\%$  loss. Similar analyses for a 2 mm diameter fiber (NA=0.38) show  $\sim 90\%$  of the scattered light reaching the input to the fiber and an

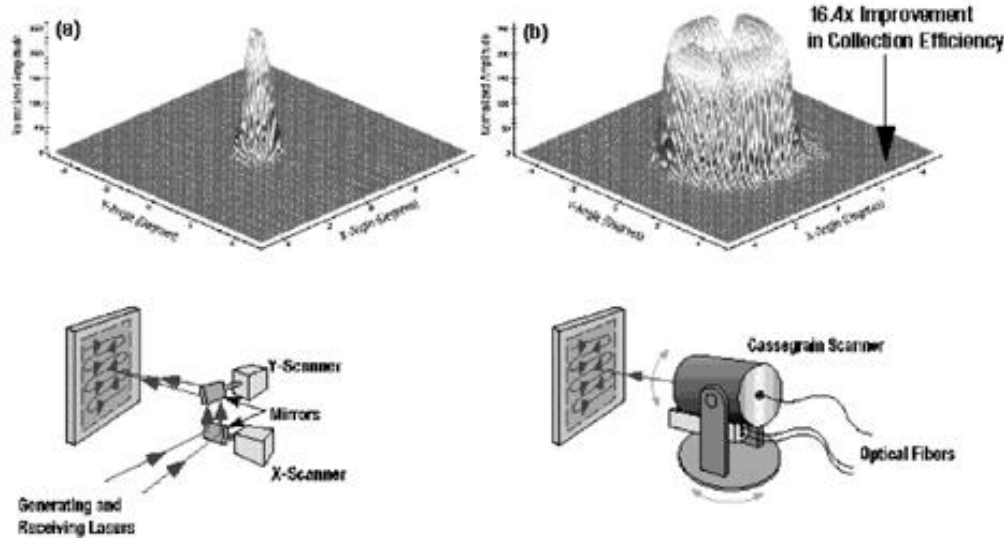


Figure 16. A Comparison of the Normalized Optical Power Collection Efficiency of the  
 (a) Galvanometer and (b) Cassegrain Scanning Systems

additional ~16% loss after coupling into the optical fiber. It should be noted that these analyses have neglected any Fresnel losses at the fiber entry and exit faces. Although a single fiber would be preferable, because of the availability of long lengths, a 2 m length coherent optical fiber bundle was used to demonstrate the proof-of-concept. This approach also simplified the design of the Cassegrain optical collection system, since implementation of an autofocus system to track the image focal plane was not required.

The optical analyses also verified that the system developed allowed operation, with minimum obscuration losses, at ranges of ~0.80–1.20 m and ~1.42–1.68 m based on two different secondary mirror configurations. The Cassegrain optical collection system was shown to have an off-axis optical power collection efficiency which exceeded that of a previously used galvanometer mirror system by ~16.4 $\times$ . Additionally, the Cassegrain system approach allowed the realization of decreased dynamic range requirements for the detection electronics since the on-axis specular reflection from the target was directly blocked by the secondary mirror/spider assembly.

### 3.3.2 Optimization of Light Coupling from the Collection Fiber to the SFPI

The final element in the LBU system is the optical detection system that demodulates and detects the ultrasonic signals contained in the light reflected from the target. Typical industrial applications of LBU systems require an optical detection system that is capable of operating with the light scattered from diffusely reflecting targets. Thus, for the studies described here, optical detection of ultrasound was performed using an SFPI [11–15]. The interferometer was operated in the reflection mode, which resulted in broadband ultrasonic detection [15–17].

### 3.3.2.1 Optical Fiber Considerations

After the scattered light from the target has been collected by the Cassegrain optical system, it is transmitted via the collection fiber from the Cassegrain focal plane to the input lens of the SFPI ultrasonic detection system. The light that is coupled into the SFPI cannot be used if it exceeds the étendue of the SFPI. The étendue of the fiber is the product of the area of its entry face and the solid angle into which it radiates (Appendix A). This solid angle is given by the following equation:

$$\Omega = 2\mathbf{p}(1 - \cos \mathbf{f}), \quad (1)$$

where  $\phi$  is the half-angle of a cone coaxially centered on the fiber entry face. Note that  $\phi$  is the meridional angle. For meridional rays passing through the fiber, the angle  $\phi$  is the same as the arcsine (NA). However, if the NA of the fiber is larger than the sine ( $\phi$ ), skew rays may exist at the input to the SFPI that have angles larger than  $\phi$  without violating the conservation of étendue. Thus, the NA of the fiber and the étendue of the SFPI are related and careful consideration must be given to ensure appropriate matching to optimize the demodulation of reflected light within the SFPI. It is possible to couple light into a fiber that does not utilize its full NA. One might expect that light coupled out of the fiber would have the same étendue as the light coupled in. However, this will only be true if there is no scattering of light within the fiber into higher order modes. This is generally true for short lengths of straight fiber. However, for longer lengths of fiber or fibers with tight bends, the light will scatter into higher order modes and fill the NA of the fiber. When this occurs, the étendue of the light coupled out of the fiber will be equal to the étendue of the fiber. Thus an optical fiber does not necessarily conserve étendue. This occurs with the coherent optical fiber bundle used with the LACIS-R system. The Cassegrain collection optics had been designed to ensure that the light was coupled *into* the optical fiber bundle with an étendue matching the  $0.4856 \text{ mm}^2 \cdot \text{sr}$  limit set by the 1 m SFPI. Unfortunately mode mixing occurred in the fibers comprising the bundle, and the output étendue was equal to the  $9.8 \text{ mm}^2 \cdot \text{sr}$  of the fiber bundle.

When operating the Cassegrain optical system with single fibers, nonconservation of étendue is generally not a problem since the étendue of the light coupled into the fiber equals or exceeds that of the fiber. The input lens must then couple all of the light from the fiber into the SFPI. This input lens is selected to have a diameter and focal length that will minimize vignetting of the light at the lens and at either mirror of the SFPI.

### 3.3.2.2 Coupling Lens Design and Analysis

Since the main requirement for the input lens is to maximize the light that is coupled into the SFPI, there is no direct requirement on the focal length or spacing from the input mirror of the SFPI. It is useful to perform some simple paraxial optics calculations to obtain an estimate of the minimum optical beam diameters obtainable at the output mirror of the SFPI. This provides insight into the best lens to use for maximizing the coupling efficiency of the light from either the target or the optical fiber into the SFPI. Two methods were investigated. One method was basically a collimation technique that attempted to collimate the light from the fiber and couple it into the SFPI. The other method attempted to image the face of the fiber into the center of the

SFPI. The details of each of these analyses are presented in Appendix B. As will be shown, the imaging technique is found to be capable of coupling a greater percentage of the light into the SFPI than the collimation method.

The results of the paraxial analysis are summarized in Figure 17 for collection fiber diameters of 1 mm and 10 mm and an NA=0.2, where F2 represents the distance from the lens to the center of the SFPI. Note that a 1 mm source diameter requires significantly smaller mirror and lens diameters compared to the 10 mm source diameter. Further, since the effective diameter of the mirrors as set by the étendue of the SFPI is only  $\sim 39$  mm (Appendix A), the additional light coupled into the SFPI by the larger diameters of the lens and mirrors does not aid in obtaining a larger signal.

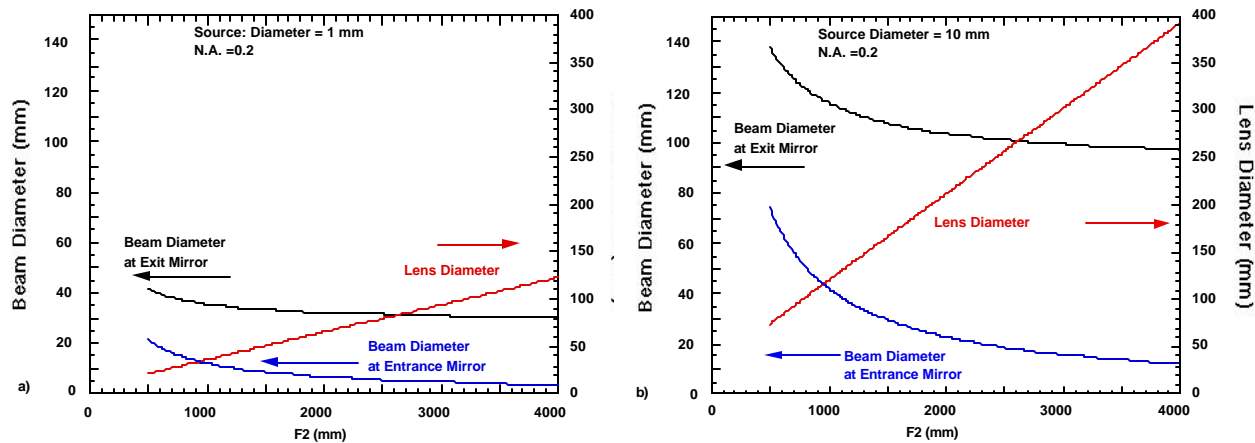


Figure 17. Beam and Lens Diameter as a Function of the Distance Between the Lens and the Center of the SFPI Cavity for a) a 1 mm Source with an NA of 0.2 ( $\theta = 11.537^\circ$ ) and b) a 10 mm Source with the Same NA. The Lens Focal Length Is Selected to Image the Source at the Center of the SFPI with a Magnification that will Minimize the Beam Size at the Output Mirror of the SFPI.

Given the presence of optical aberrations, the actual performance of any system is most accurately determined by using numerical analysis and ray-tracing packages such as OptiCAD or ZEMAX. We have used these tools to determine the optimum performance that can be achieved by replacing the optical fiber bundle with a single, large-core diameter optical fiber. A schematic for the model (Figure 18) contains the beam splitter located at the entrance to the SFPI, as well as the optical fiber and a lens. For the initial screening of lenses for coupling light from the fiber to the SFPI, the model for the SFPI contained an entrance window with zero optical power and an exit mirror. The version of ZEMAX being used, ZEMAX-XE, does not allow the reflectivity of the mirrors to be adjusted to any value other than 100%. The initial screening test for the lenses was to determine how much of the light could be transmitted through the entrance window and reflected from the exit mirror without vignetting. The system aperture was specified as an object space NA of 0.38, the field was set by the diameter of the fiber (1.5 mm), and the wavelength was 1.064  $\mu\text{m}$ .

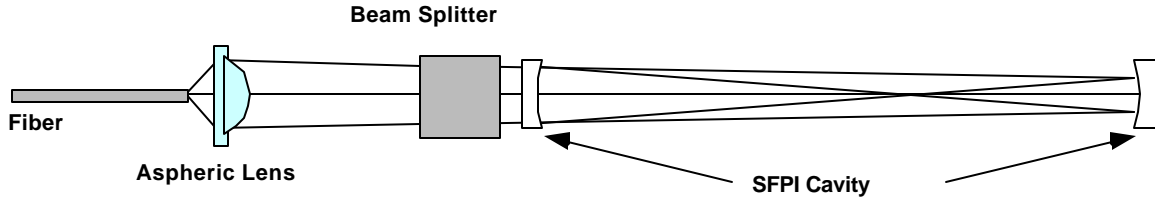


Figure 18. Schematic Diagram of Model Used for Coupling Between an Optical Fiber and the SFPI.

When using a paraxial lens, it is possible to couple nearly 100% of the light emanating from the fiber into the SFPI, confirming the paraxial analysis above. However, when a real lens is used, the amount of light that is coupled into the SFPI decreases significantly because of the aberrations associated with lenses that have a large enough NA to accept all of the light from the 0.38 NA fiber. Several lenses were considered for collecting the light from the optical fiber and coupling it into the SFPI. These include an equi-convex lens (Coherent 43-1452), an air-spaced, two-element condenser (Melles Griot 01 CMP 125) and an aspheric condenser (Melles Griot 01 LAG 019). The amount of light from the fiber that can be coupled into the SFPI without vignetting at either the entrance or exit mirror for each of these lenses is summarized in Table 2.

**Table 2. Efficiency of Light Coupling into the SFPI for Selected Lenses**

Lens	Diameter (mm)	Focal Length (mm)	Light Coupled into SFPI (%)
Coherent 43-1452	100	100	63.55
Melles Griot 01 CMP 125	100	100	71.85
Melles Griot 01 LAG 019	65	53	98.62

### 3.3.2.3 Summary and Discussion

Since the performance of the aspheric condenser was significantly better than that of the others, it was selected for further studies of the coupling from the fiber to the SFPI. Also, since the version of ZEMAX that is being used does not support ray tracing through nonsequential components, it is necessary to simulate the multiple bounces of the light through the SFPI with multiple mirrors in the model. These mirrors reflect the light back and forth over the length of the SFPI. The model used for these studies had 14 mirrors, which effectively simulated light passing through the SFPI seven times. This is sufficient to allow an estimate of whether light is continuing to leak from the cavity or has reached a steady state. The results show that there is no significant loss of light, caused by vignetting at either the entry or exit mirrors, during the first seven passes through the SFPI. This lens was selected for coupling the light from the fiber to the SFPI.

### 3.3.3 Optimization of Laser Beam Delivery with the Cassegrain Scanning System

An optical subassembly (Figure 5.) is mounted beneath the Cassegrain scan head whose purpose is to deliver the generation and probe laser beams to the target. This subassembly contains the optical fibers that are delivering the generation and probe lasers. It also includes the lenses and a

dichroic mirror that allow the beams to be made collinear and brought to a focus on the target with the desired spot size. A mirror attached to the rear of the secondary mirror of the Cassegrain optics (Figure 5.), and oriented at 45°, deflects the combined generation and probe laser beams to the target and ensures that they propagate coaxially with the optical axis of the Cassegrain scan head. Since in the LACIS-R design the subassembly must fit beneath the Cassegrain housing, the space requirements must be minimized. To gain insight into the system design considerations, it is helpful to initially use a paraxial design procedure for specifying the lens and fiber diameter that should be used in the relay optics. However, to obtain specific performance data, such as the effect of lens aberrations, the efficiency with which the light is transmitted to the target, and the spot size of the beams at the target, an exact ray tracing analysis must again be used. The details for both a paraxial and a numerical ray-tracing analysis are presented in Appendix D.

### ***3.3.3.1 Paraxial Analysis of the Cassegrain Subassembly Relay optics***

In Appendix D, both a collimation technique and an imaging technique are investigated for transmitting the generation and probe laser beams, emitted by the fibers, to the target. The light at the target must be confined within a certain spot size that is consistent with the étendue requirements of the SFPI and with the light collecting capabilities of the primary mirror of the Cassegrain optics. Results of the analysis showed that unless the fibers have core diameters  $\ll 0.1\text{mm}$ , it is best to image the delivery fiber face onto the target. When imaging the fiber face, both the core diameter and NA of the fiber significantly affect the diameter of the lenses required to relay the light from the fiber to the target as well as the spot size at the target. The relationship between the fiber diameter and the beam diameter at the lens is linear, and the relationship between the beam diameter at the lens and the NA of the fiber is approximately linear for NAs  $<0.4$  (Figure ). Thus a small fiber diameter and NA are required to obtain a small spot size at the target with reasonably sized relay optics. Using a 0.1 mm diameter, 0.12 NA fiber, it is possible to obtain a 6 mm diameter spot at the target with a lens having a focal length of 19.3 mm and a diameter of only 4.8 mm. This size fiber is suitable for use with the probe laser. If the diameter of the fiber is increased to 1.5 mm, which is suitable for the generating laser, the lens focal length must be increased to 235 mm and the lens diameter increases to 72.5 mm. Unfortunately, it is not possible to fit this size lens into the space available beneath the Cassegrain housing. This conflict led to using a numerical ray-tracing program, ZEMAX, to model the relay optics for the generation laser.

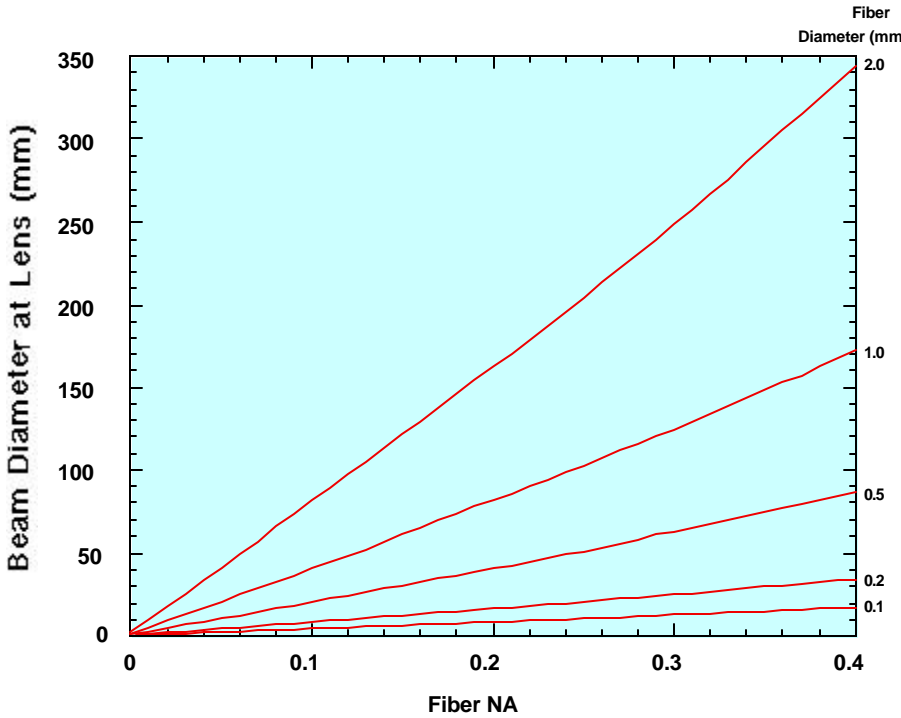


Figure 19. Beam Diameter at Lens Versus Fiber NA for a Range of Fiber Diameters and a 6 mm Target Spot Diameter

### 3.3.3.2 Ray-Tracing Analysis of the Cassegrain Subassembly Relay-Optics

The objective of the numerical ray-tracing was to determine a design that would achieve the desired spot size at the target while minimizing the power loss due to vignetting. A model of the LACIS-R generation laser relay optics was prepared, which consists of the hardware shown in Figure 20. The light is emitted from the optical fiber, passes through a lens to the first turning mirror (mirror 1), then to the second turning mirror (mirror 2) and finally to the target. Mirror 1 has an elliptical periphery with major and minor axes of 31.5 mm and 22.4 mm, respectively. The second mirror has a circular periphery with a diameter of 18 mm. The optical fiber is 0.91 mm in diameter with an NA of 0.22. The lens selected to image the fiber face onto the target is a Newport KPX094 plano-convex lens with a diameter of 25.4 mm and a nominal focal length of 100 mm. The model allows the face of the 0.91 mm diameter fiber to be imaged onto the target at a range of ~1028 mm from the Cassegrain primary mirror. When the lens is adjusted to produce the minimum spot size on the target, which is ~8.8 mm, the transmitted energy is only ~14.6% of the energy emitted from the fiber. This is slightly less than the energy that was experimentally transmitted through this system which was ~20%. A slightly larger spot size at the target during the experiments and a nonuniform distribution of light across the output face of the fiber are the likely causes of the difference between the two results. Neither of these parameters was precisely measured experimentally, but could result in an increase in the transmitted energy.

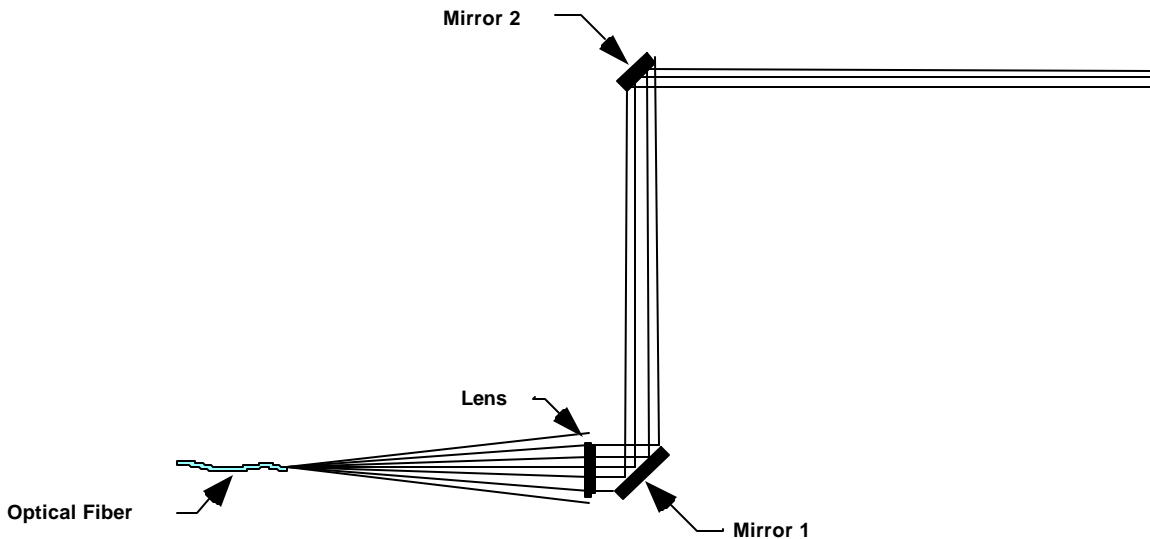


Figure 20. Schematic of LACIS-R Relay Optics Configuration Used to Transmit Generation Beam from Optical Fiber

The power transmission efficiency can be improved by changing the model so that the lens is placed between the two turning mirrors. This allows a slightly larger lens to be used if needed and reduces the vignetting at mirror 1. This model is shown in Figure 21. In addition, the beamsplitter that is used to combine the generation and probe laser beams was added to the model. In this analysis, the diameter of the optical fiber that is to be used to deliver the Q-switched Nd:YAG generation laser to the Cassegrain subassembly was increased to 1.0 mm and its NA was decreased to 0.12. The model has been used with three different lenses, including the one used with the LACIS-R optics. The results of these calculations are summarized in Table 3.

**Table 3. Optical Transmission Efficiency of Relay Optics with Selected Lenses**

Lens Model	Diameter (mm)	Focal Length (mm)	Power Transmitted (%)	RMS Spot Size (mm)
Newport KPX-094	25.4	100	46.6	8
Melles Griot LAO-139	30	140	20.5	6
Melles Griot LAO-189	30	200	8.7	4

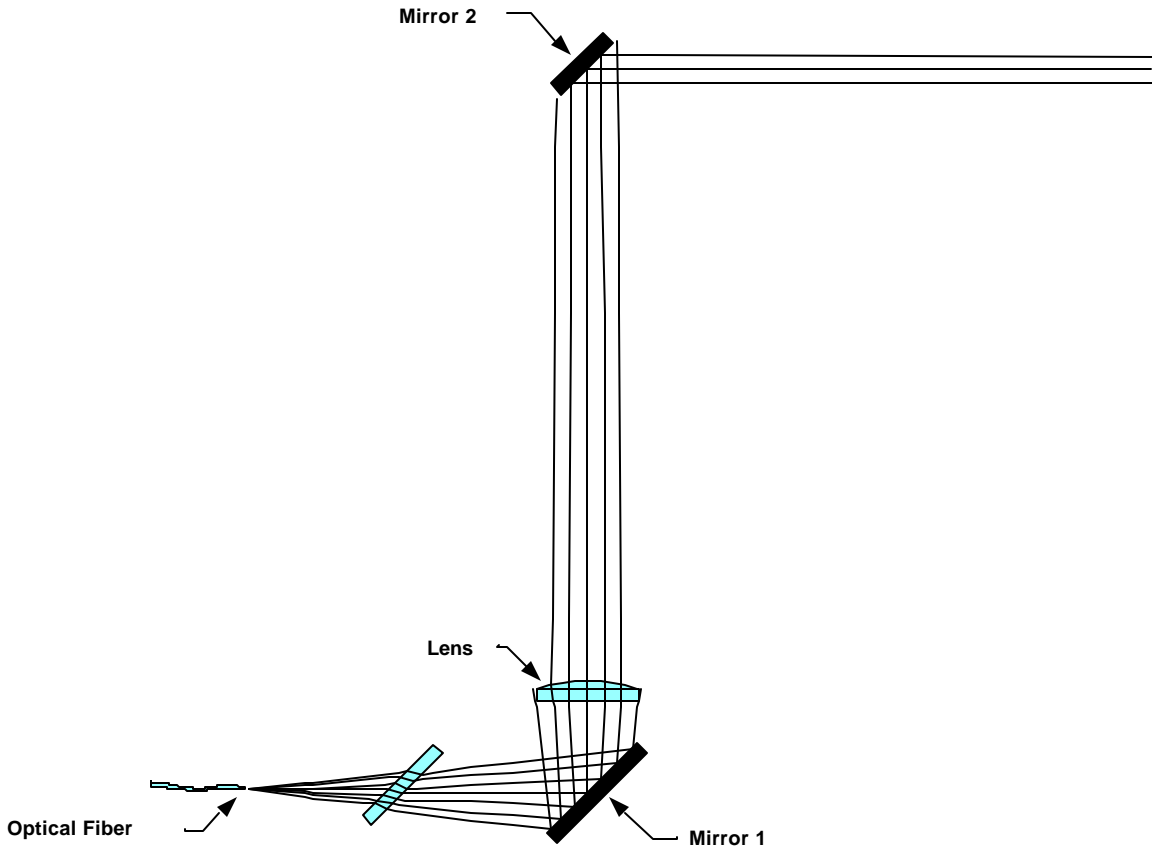


Figure 21. Schematic of an Improved Relay Optics Configuration Used to Transmit the Generation Beam from Optical Fiber to Target

### 3.3.3.3 Summary

Using the Newport KPX-094 lens, the improved design produces an 8 mm spot at the target and a transmission efficiency of 46.6%. For this configuration, the first folding mirror transmits about 86% of the energy, which implies that ~40% of the energy is vignetted at the second folding mirror. Note that as the spot size at the target is made smaller, the power transmission efficiency decreases rapidly. The energy throughput can be improved further without increasing the obscuration of the Cassegrain primary mirror by redesigning the mount for the second mirror and using a larger mirror with an elliptical cross section that will decrease the vignetting. This must be done for systems that require high resolution and, therefore, small spot sizes. To further increase the transmission efficiency, it is necessary to redesign the entire framework in which the relay optics are mounted, with the goal of increasing the diameters of all of the lenses, mirrors and the beamsplitter. Note that because of the constrained space below the Cassegrain housing, the relay optics would have to be moved to another location, perhaps above the Cassegrain housing. The details of such a redesign have not been investigated in this program.

## 3.4 Experimental Characterization of the Optimized Cassegrain Scanning System

After completing all of the optimization analyses, we selected various fiber and lens combinations to realize the improvements predicted. These results are reported below.

### **3.4.1 Optimized Coupling and Delivery of the Generation and Probe Lasers to the Target**

Based on the results of the optimization analyses for delivery of the Q-switched Nd:YAG generation laser, the coupling optical fiber was changed from a 0.91 mm core diameter with an NA of 0.22 to a 1.0 mm diameter fiber with an NA of 0.12. This resulted in the measured transmitted pulse energy through the Cassegrain subassembly increasing from ~33% to ~67% efficiency. To remain below the damage threshold of the delivery fiber input, the maximum energy that can routinely be transmitted through the optical fiber is ~45 mJ/pulse (Section 4.5.4). Thus the improved transmission efficiency through the Cassegrain relay optics readily permits ~30 mJ/pulse to be delivered to the target. This is a significant improvement, which has permitted the generation and detection of ultrasonic waves using the Cassegrain collection system and the Q-switched Nd:YAG generation laser.

For the delivery of the probe laser, the coupling optical fiber was changed from a 600  $\mu\text{m}$  core diameter with an NA of 0.39 to a 100  $\mu\text{m}$  diameter fiber with an NA of 0.12. This resulted in the combined fiber coupling and transmitted pulse energy through the Cassegrain subassembly increasing from ~32% to ~85% efficiency. Since the fiber-coupling losses were ~8%, a further 7% loss occurred as the beam propagated through the relay-optics. Again, this was a significant improvement over the previous configuration and allowed the majority of the probe laser light to reach the target.

### **3.4.2 Ultrasonic Signal Detection with the Optimized Cassegrain Scanning System**

To assess the overall Cassegrain optical system improvement of the LACIS-R design, a white-painted graphite/epoxy panel (~2 mm thick) was irradiated with pulses from the Q-switched Nd:YAG laser, and the resulting signals detected with the SFPI system. Figure 22 shows the resulting ultrasonic signal, which clearly shows the longitudinal wave detected after reflection from the back wall of the part. Unlike previous attempts to detect signals with the LACIS-R configuration, these signals were attainable without the need for signal averaging. However, the SNR is still unacceptable for large-area scanning applications. In contrast, Figure 23 shows a detected waveform in which the Cassegrain system was used to deliver the generation laser beam, but the galvanometer-based bulk optical system was used to deliver the probe laser to the target and to collect and relay the scattered light back to SFPI detection system. Comparison of Figure 22 and Figure 23 clearly shows much improved system sensitivity when the galvanometer system is used for probe laser delivery and collection.

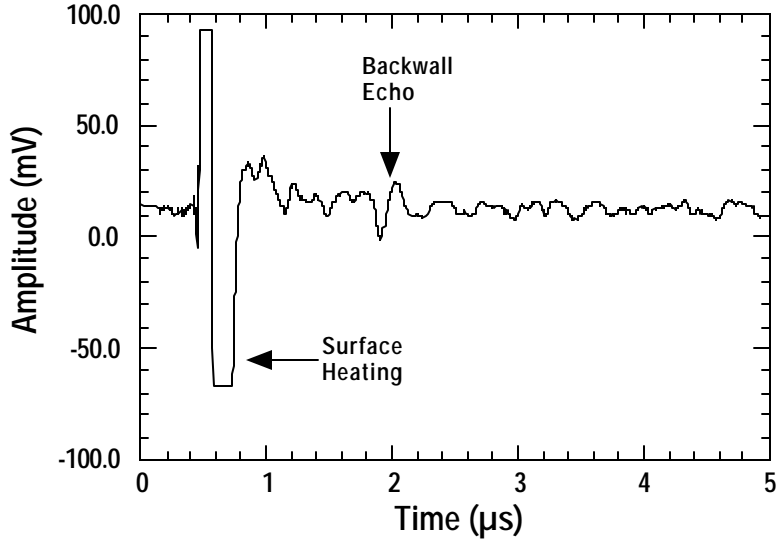


Figure 22. Detection of Q-Switched Nd:YAG Laser-Generated Ultrasonic Signals in a White-Painted Graphite/Epoxy Panel Using the Modified Fiber-Coupled Cassegrain Optical Scanning System

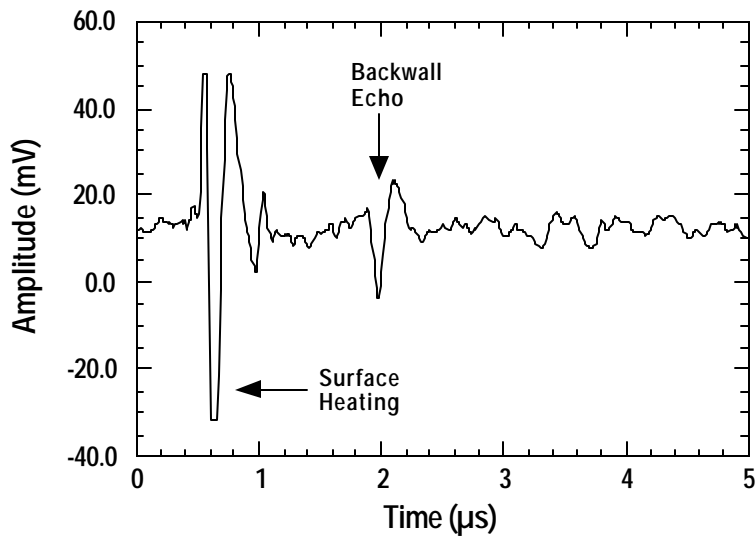


Figure 23. Detection of Q-Switched Nd:YAG Laser-Generated Ultrasonic Signals in a White-Painted Graphite/Epoxy Panel. The Modified Fiber-Based Cassegrain System Was Used to Deliver the Generation Beam to the Target, But the Probe Beam Was Delivered and Collected Using a Bulk Optics Galvanometer Scanning System

### 3.5 Summary and Discussion

Initial results under the LACIS-R program successfully demonstrated the use of the fiber-coupled Cassegrain optical scanning system for the detection of laser-generated ultrasonic waves. In that study an alexandrite laser was used for ultrasonic generation, but the SNR was low, and signal averaging was required. With the optimization of the system design and the implementation of fiber-delivery of a Q-switched Nd:YAG generation laser, we were also

successful in demonstrating ultrasonic signal detection. Although signals were detected with reasonable SNR without the need for averaging, the overall sensitivity with the Cassegrain system is significantly below that obtained with the galvanometer-based scanning system.

Although the Cassegrain system exhibited an  $\sim 16.4\times$  increase in the optical power collected when compared with the galvanometer scanner, not all of this gain is realized in practice. The Cassegrain optical system design ensured that the collected light was coupled into the coherent optical fiber bundle with an étendue of  $0.4856\text{ mm}^2.\text{sr}$ , commensurate with the limit set by the 1 m SFPI configuration. However, mode dispersion in the 2 m long optical fiber bundle resulted in nonconservation of NA, and the light that exited the fiber bundle filled the full NA of 0.6. This result is the antithesis of measurements obtained with a single-core multimode fiber. Thus, all of the light was not effectively coupled into the SFPI and currently prevents the benefits of the increased collection efficiency from being fully realized. Further analyses have shown [18] that it was not possible, with practical-sized optical elements, to collect all of the light exiting the optical fiber bundle with this large a numerical aperture and efficiently match into our present SFPI configuration. However, this problem can be eliminated by using a fiber bundle of lower NA or adopting the approach of perhaps a 1 mm diameter single optical fiber where the position of the fiber input face actively tracks the image plane as the range to the target varies during a raster. This latter approach was not implemented during this program because of the additional engineering requirements. However, we have explored the availability of large-core diameter optical fibers. Currently 1.5 mm and 2.0 mm diameter fibers are commercially available from FiberGuide Industries. Both 1.5 mm and 2.0 mm diameter fibers are available in a PCS (plastic-clad silica) configuration which are less expensive than silica-clad fibers, although they are only available with a nominal NA of 0.4. Furthermore, this type of fiber exhibits a decrease in NA as a function of fiber length. For a 3 m length of fiber, the NA is  $\sim 0.38$ . The NA reaches a minimum steady-state value of 0.23 for lengths exceeding 50 m. The silica core/silica-clad fibers are available with a maximum core diameter of 1.5 mm and NAs of 0.12, 0.22 and 0.26. However, the value of NA is not length dependent. Table 4 lists these three large-core diameter optical fibers with the corresponding equivalent étendue. It can be seen that the silica/silica optical fiber is the only one that does not exceed the étendue requirements of the current SFPI configuration. Although, the lengths of the PCS fibers could be tailored to reduce the NA, the 2.0 mm diameter fiber would always slightly exceed the required NA. The NAs required to obtain the appropriate étendue of  $0.4856\text{ mm}^2.\text{sr}$  are also given in Table 4.

**Table 4. Optical Parameters of Selected Commercial Optical Fibers**

Fiber Type	Fiber Ø	Fiber NA	Equivalent Étendue	NA Equivalent to $0.4856\text{ mm}^2.\text{sr}$
FiberGuide PCS	1.5 mm	0.38 (3 m )	0.8329	0.2925
FiberGuide Silica/Silica	1.5 mm	0.26 (N/A)	0.3819	0.2925
FiberGuide PCS	2.0 mm	0.38 (3 m )	1.4807	0.2204

## 4. OPTICAL FIBER DELIVERY OF HIGH PEAK-POWER LASER PULSES

An important aspect of the Cassegrain scanner concept was the efficient delivery of the ultrasonic generation and detection laser beams to the target via long lengths of optical fiber. When selecting an optical fiber for transmission of the pulsed generation laser beam, several parameters must be considered [9]. Most important are the fiber attenuation characteristics for the chosen generation laser wavelength and the capability of the fiber to withstand the short duration, high peak-power laser pulses that are typically employed to generate ultrasound efficiently. Investigations were performed to determine the applicability of using fiber-coupling with CO<sub>2</sub>, alexandrite and Q-switched Nd:YAG ( $\lambda = 532$  nm) generation lasers and a long-pulse Nd:YAG probe laser (LPPL). Silica core multimode fibers, that transmit efficiently at the Nd:YAG ( $\lambda = 532$  and 1064 nm) and alexandrite laser ( $\lambda = 720\text{--}800$  nm) wavelengths, and that can satisfy the high peak-power laser pulses requirements, were readily available from several commercial vendors. However, optical fibers that could be used to transmit the pulsed CO<sub>2</sub> generation laser ( $\lambda = 10.6 \mu\text{m}$ ) over long distances were more difficult to obtain. Four classes of fibers for use at 10.6 μm were investigated; polycrystalline silver halide fibers, chalcogenide glass fibers, hollow metallic waveguides, and hollow sapphire fibers. Typically, these fibers had much higher losses than silica fibers and were intended for transmission over relatively short lengths of only 1 to 2 m. The hollow sapphire waveguide fiber relies on the anomalous dispersion of the sapphire to produce a refractive index less than that of air (i.e., <1.0) in a small wavelength interval that includes 10.6 μm, so that the sapphire acts as the fiber cladding with the air being the fiber core. This provides the waveguiding effect that is characteristic of an optical fiber. Within this wavelength interval, the hollow sapphire fiber has many desirable characteristics, including relatively low loss compared with the other infrared fiber types, and capability for transmitting pulses with large peak-powers, but is available only in lengths of 1 to 1.5 m with a minimum bending radius of 15 cm. Chalcogenide glass fibers have moderate losses and are available in lengths of up to 30 m with a minimum bending radius of 25 mm. However, it was not clear whether these fibers would sustain the high peak-powers characteristic of the transversely excited atmospheric (TEA) CO<sub>2</sub> generation laser pulses. The properties of the silver halide fibers deteriorated with age, repeated bending, and exposure to ultraviolet light, while the hollow metal waveguides required cooling, were susceptible to damage by high peak-power pulses and were very expensive. Ultimately, the hollow sapphire waveguide fiber was chosen for testing purposes.

### 4.1 Optical Fiber Attenuation Characteristics

Silica core multimode fibers that can operate over a wide range of generation laser wavelengths, from the UV (ultraviolet) to near IR (infrared), are readily available from several commercial vendors. The attenuation of a silica core fiber, which is dependent on the optical wavelength, is determined by the cladding material and the concentration of OH ions in the silica. Low OH<sup>-</sup> fibers have superior transmission in the visible and near-IR range while high OH<sup>-</sup> fibers are typically better suited to UV and select visible applications. Typical attenuation characteristics over a broad laser wavelength range are given in Figure 24 for a 3M™ TECS™-coated silica/silica optical fiber. It is fortuitous that the spectral characteristics of the high OH<sup>-</sup> silica/silica fibers available from either 3M or FiberGuide Industries have minima in attenuation

for Nd:YAG at both the probe ( $\lambda = 1064$  nm) and generation ( $\lambda = 532$  nm) laser wavelengths and also the alexandrite generation laser wavelengths ( $\lambda = 720\text{--}800$  nm). Based upon the high-power handling capability and low spectral attenuation, these fibers were selected for the current studies since they could be used interchangeably between laser systems. However, as described above, silica-based fibers are not suitable for operation in the far infrared and have very high attenuation at the CO<sub>2</sub> generation laser wavelength ( $\lambda = 10.6 \mu\text{m}$ ). The hollow sapphire fibers used with this generation laser will be described below.

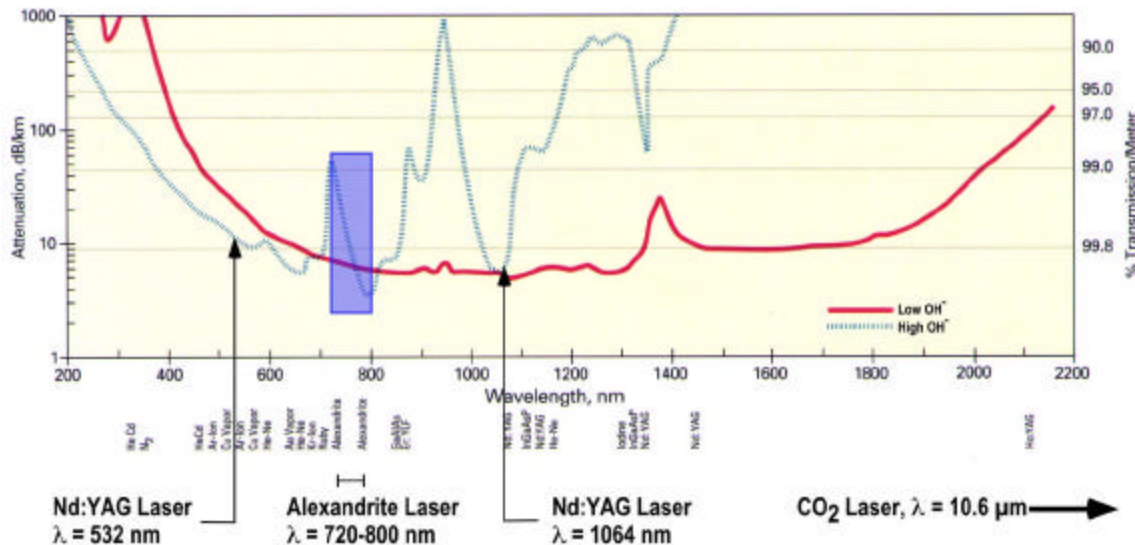


Figure 24. Spectral Response for 3M™ TECS™ – Coated Silica/Silica Optical Fiber

#### 4.2 Fiber Damage Considerations

The fundamental limit of any optical fiber-based, pulsed-laser delivery system depends on the surface and/or bulk damage threshold of the fiber core material. Given the typical laser pulse energies used for ultrasonic generation and the short pulse duration required to efficiently generate ultrasonic waves, the damage threshold for the optical fiber is easily approached. Typically silica fibers can withstand incident power densities of 1 to 5 GW/cm<sup>2</sup> without damage. However, laser parameters such as wavelength, pulse energy, pulse duration, transverse and longitudinal mode structure, beam size, and location of the beam waist all are important in determining the damage threshold [19,20]. Other factors that may detrimentally affect system performance include poor beam quality, misalignment effects, and nonlinear effects which produce internal focusing of the beam such as the electro-optic Kerr effect. Cleanliness and prior irradiation history also are factors in determining the damage threshold.

In this program, damage observed in optical fibers caused by incident laser energy has been attributed to two primary effects. The first is high average power, which causes excessive temperature rise in the materials surrounding the core. It usually occurs with either CW (continuous wave) or long-pulse lasers such as the LBU system probe laser. The temperature rise is usually caused by laser energy that missed the fiber core upon input and instead entered the cladding or exceeded the fiber numerical aperture, and exited through the side of the core. The

surrounding cladding, buffer, epoxy or connector materials absorb this leaked energy and heat up until the core/cladding interface is destroyed. This is a gradual degradation, which, once started, will propagate with continued illumination and eventually result in catastrophic fiber failure.

The second primary effect causing damage in optical fibers occurs for high peak-powers and can result in fracturing or localized shattering of the fiber. It usually occurs with short pulse lasers, such as the lasers used to generate ultrasonic waves. The maximum energy that can be delivered through a fiber is ultimately limited by the peak optical power incident on the fiber entry face. Fiber damage can also result from peak-powers that are less than this damage threshold if the pulse is locally absorbed at an impurity site either within the fiber or at the entry or exit faces. For sufficiently high incident power densities, ablation of these impurities occurs, resulting in a plume of rapidly expanding ionized particles that cause an acoustic shock wave to be launched into the fiber. Typically it is this acoustic shock wave that fractures or shatters the fiber [21]. Subsequent laser pulses are scattered into the cladding or epoxy, and with the excessive heating that occurs, catastrophic failure follows. In addition, poor beam quality can result in skew rays that exceed the numerical aperture of the fiber, and thus pass into the cladding and produce excessive heating at the core/cladding interface.

### **4.3 Fiber Core Size and Numerical Aperture Selection**

Finally, once a selection of an optical fiber with suitable attenuation characteristics and a sufficiently high damage threshold has been made, the fiber core size and numerical aperture (NA) can be selected. General considerations suggest selection of a fiber with a large-core diameter, to avoid damage, and a large NA for less critical fiber alignment requirements and to promote optimized transmission through multimode fibers by exciting a large number of modes. However, for LBU applications, the use of fibers to deliver light to and collect light reflected from a target impose conflicting requirements. For optical collection, it is advantageous to have a fiber with a large diameter and NA to obtain a large areal scan range without dynamically refocusing. However, ultimately the étendue requirements of the detection interferometer must also be taken into consideration. This is discussed in detail in Section 3.3. Also, when coupling the generation and probe laser from a fiber to the target, it is advantageous to have a small fiber diameter and NA to obtain a small spot size at the target with reasonably sized relay optics. Although the latter is possible with the probe laser, the typical generating laser power densities dictate fibers with core diameters of 1000  $\mu\text{m}$  or greater. These conflicting requirements result in design trade-offs to select a fiber diameter and NA that will maintain optimal transmission and minimize the target spot size while avoiding damage to the fiber.

### **4.4 Coupling of High Peak-Power Laser Pulses into Fibers**

#### **4.4.1 Criteria for Optimum Coupling**

Although damage caused by excessive laser energy or excessive peak-power is of primary concern, it is also important to use care when coupling the laser beam into the fibers. In optimizing the fiber launch geometry for coupling high peak-power, Q-switched lasers into a large-core optical fiber, adherence to the following criteria [21,22] were important in determining the survivability of the optical fiber:

- To avoid directly damaging the fiber, the incident laser beam should be focused in front of the input face of the fiber and then expanded to illuminate ~70–80% of the specified diameter of the fiber core. This criterion arises from the concentricity tolerances given for large-core diameter fibers and also provides a margin of error for translation misalignment or illumination with noncircular input beams. Ultimately, the goal is to ensure that no laser light falls within the cladding, since this will typically result in eventual fiber failure.
- The input cone angle should generally be ~70-80% of the acceptance angle of the optical fiber. Squeezing the fiber, with a fiber chuck assembly, or tightly bending the fiber should be avoided since it may cause higher order modes to couple out of the core. Energy exiting the fiber can cause a failure in the surrounding cladding and jacketing materials.
- Preparation of the input and output faces of the optical fiber is critical. With a well-prepared fiber input face, the surface damage threshold can approach that of the bulk material. One of two standard methods is used to properly prepare the input face of the fiber, cleaving or polishing. The ideal RMS (root mean square) surface finish for maximum power handling should be 25% of the incident laser wavelength [21]. One problem with polishing the input face of the fiber is that compounds or impurities become embedded within the surface of the fiber input face and can then act as absorption sites when exposed to the high peak-power laser input. The resulting thermal stress may fracture the fiber. Alternatively, obtaining a good cleave in optical fibers with large-core diameters is difficult and often results in a chipped region where the cleave was initiated, which is highly susceptible to light scattering and absorption. However, commercial vendors can perform this service with very high quality results. Consequently, cleaving the optical fiber is the preferred technique for high power laser beam delivery.

#### **4.4.2 Optimization of the Lens to Fiber Coupling Distance**

As reported above, it is desirable to fill the incident optical fiber core diameter to ~80% and the input cone angle should generally be ~70-80% of the acceptance angle of the optical fiber. Based on these criteria, simple paraxial calculations can be performed to determine the appropriate focal length lens and approximate lens-to-fiber spacing. In practice, the longitudinal spherical aberration of a real lens will result in the location of the minimum beam diameter being some distance closer to the lens. While this location is readily calculated using geometric ray-tracing optical analysis with software packages such as ZEMAX, ultimately the Gaussian properties of the laser beam add a further correction to the size and location of the minimum beam waist. Unfortunately, to accurately measure this requires accurate knowledge of the  $M^2$  factor, which is a measure of the beam quality. While this can be accurately measured, it is not a trivial measurement to perform. Thus, we have adopted an experimental method to optimize the lens-to-fiber distance. The essential steps of this method are outlined as follows:

- Use paraxial lens theory to select an appropriate focusing lens.
- Use incident pulse energies of ~1 mJ and monitor the energy delivered at the fiber output.
- Arrange the lens-to-fiber distance so that the beam is focused in front of the optical fiber and expands to overfill the fiber.

- Verify that a small lateral adjustment of the optical fiber position does not result in any change in received optical energy.
- Iterate the process of reducing the lens-to-fiber distance and realigning the optical fiber until small lateral adjustments of the optical fiber position result in measurable changes in detected optical energy. At this point the incident beam approximately fills the core of the optical fiber.
- Reduce the lens-to-fiber distance further until small lateral adjustments of the optical fiber do not result in any energy loss. This is a subjective measure unless the fiber positioner is equipped with a high-resolution digital readout.

## 4.5 Experimental Results

### 4.5.1 Fiber Coupling of the CO<sub>2</sub> Generation Laser

A 1.5 m long hollow sapphire waveguide fiber, which had an internal diameter of 600  $\mu\text{m}$ , was used to investigate transmission of the CO<sub>2</sub> generation laser to the Cassegrain subassembly. The fiber was not terminated, but a fiber chuck was used for interfacing with the Cassegrain optical subassembly. Since the fiber was expensive, initial studies utilized a separate 380 mm length of fiber. A 25.4 mm diameter, 100 mm focal length zinc selenide lens was used to focus the CO<sub>2</sub> laser pulses into the 380 mm section of hollow sapphire fiber so that the transmission characteristics could be investigated. The incident and transmitted laser energies measured at the input and output ends of the fiber, respectively, showed that ~90% transmission was obtained at low incident energies (~15 mJ/pulse). The loss in the fiber increased at higher peak-powers to yield ~65% transmission with incident energies of 130 mJ/pulse. For optimum coupling into the hollow fiber and minimum attenuation, the CO<sub>2</sub> laser should be operated in TEM<sub>00</sub> mode with a beam waist that is ~0.65× the bore diameter of the fiber [23]. In these tests, the laser was not operated in TEM<sub>00</sub> mode, and while the beam diameter at the input to the fiber could not be accurately measured, it did not appear to be the optimum diameter. Although both of these factors contributed to the increased loss, for purposes of ultrasonic wave generation, the measured losses appeared acceptable.

Since hollow waveguides do not have a bulk core material, they are much less susceptible to laser damage problems associated with coupling high peak-power laser pulses into solid fibers. However, the robustness of the hollow sapphire waveguide to damage caused by misalignment of the incident laser beam was evaluated. The incident beam was misaligned so that it was focused onto the sapphire annulus. In doing so, ablation at the fiber surface resulted in pitting and chipping of the sapphire. In spite of the damage to the input surface, when the alignment was corrected so that the incident laser pulse was again focused into the center of the hollow fiber, there was no measurable degradation in the transmitted energy level. Thus the transmission characteristics of the fiber were insensitive to damage around the entrance annulus, as expected. Another observation was ionization of the air core at higher peak-powers. This was caused by debris or contamination inside the bore. The result of the air breakdown was low light transmission through the fiber, since the incident laser energy was reflected by the plasma formed by the ionized air. However, after the ionization had subsided, the transmission coefficient returned to its previous value with no apparent deleterious effect on the integrity of the fiber.

The temporal characteristics of the CO<sub>2</sub> laser pulses were monitored using a fast photo-electromagnetic detector. Propagation through the fiber did not change the temporal properties of the laser pulse. The spatial characteristics were monitored by visual observation of the beam fluorescence when irradiating a graphite target. The output beam from the CO<sub>2</sub> laser has a rectangular profile because of the shape of the electric discharge region between the laser electrodes and the aspect ratio of the beam profile changes with propagation distance. Although the desired aspect ratio may be obtained with the use of cylindrical optical elements, one advantage of propagating the CO<sub>2</sub> laser through the hollow sapphire waveguide was homogenization of the output beam profile into a circular beam with an equivalent numerical aperture of ~0.025, which agreed with the fiber NA specification.

After initial testing was completed, the 1.5 m length of hollow core sapphire waveguide was integrated with the Cassegrain optical subassembly. Although in initial studies >65% transmission through a 380 mm length of waveguide was achieved, only 25% transmission efficiency could be realized for the 1.5 m length waveguide. The cause of the decrease in the transmission was not determined. Given the high loss and the rigidity of the sapphire waveguide, which prevented scanning the Cassegrain head over more than a few degrees, it was decided that either the Nd:YAG ( $I=532$  nm) or the alexandrite generation laser might yield a more appropriate ultrasonic generation source, and further experimentation with the fiber-coupled CO<sub>2</sub> generation laser was curtailed.

#### 4.5.2 Fiber Coupling of the Alexandrite Generation Laser

A 100 m length of silica optical fiber (3M™ TECS™ hard-clad fiber), with an NA of 0.39, was used for delivery of the alexandrite generation laser beam, with a core diameter of 1000 μm. The fiber was terminated with type SMA (sub miniature assembly) 905 high-power connectors and interfaced with the optical subassembly that was mounted beneath the Cassegrain scan head (Section 3.2). A plano-convex lens having a focal length of 150 mm was used to couple the alexandrite laser pulses into the optical fibers. The alexandrite laser was operated at band center ( $I \sim 755$  nm) with typical output energies of ~100 mJ in a ~95 ns pulse. This was similar to the operating energy level and pulse width of the TEA CO<sub>2</sub> laser that is currently being used as a generation laser for industrial inspection of composite materials [2,3,24]. This configuration resulted in a power density of ~0.54 GW/cm<sup>2</sup> at the input to a 1000 μm core diameter fiber.

Typical fiber damage thresholds are specified as 1-5 GW/cm<sup>2</sup> so care was needed when coupling the alexandrite laser to avoid damage to the fiber caused by overfilling. Well-prepared fiber end faces were also required to avoid localized absorption sites, which can lead to thermally induced failure [9]. Attenuation in the optical fiber was at the alexandrite laser wavelengths was ~3 dB/km. This translated to a theoretical loss of ~7% over a 100 m length of optical fiber. The fiber-coupling losses and attenuation of the 100 m fiber length resulted in an overall transmission efficiency of ~83%. Sustained output energies of 65 mJ (alexandrite) were demonstrated at pulse repetition rates of 20 Hz.

### 4.5.3 Fiber Coupling of the Long-Pulse Nd:YAG Probe Laser

#### 4.5.3.1 Coupling and Transmission Issues

The Fiber Coupling options that have been investigated with the long-pulse Nd:YAG probe laser are detailed in Table 5. Initial coupling efforts used a 100 m length of silica optical fiber (3M™ TECS™ hard-clad fiber), with an NA of 0.39, for delivery of the long-pulse Nd:YAG probe laser with a fiber core diameter of 600  $\mu\text{m}$ . The fiber was terminated with high-power SMA 905 connectors and interfaced with the optical subassembly that was mounted beneath the Cassegrain scan head (Section 3.2). A plano-convex lens, with a nominal focal length of 100 mm, was used to couple the LPPL into the optical fiber. The LPPL had a peak-power of ~1 kW [25] with resulting power densities of ~360 kW/cm<sup>2</sup> when focused to fill a 600  $\mu\text{m}$  core optical fiber. Thus the power densities were comfortably below the 1 to 5 GW/cm<sup>2</sup> damage threshold specification for the fiber. Attenuation in the optical fiber for the Nd:YAG laser wavelength was ~3 dB/km. This translated to a theoretical loss of ~7% over a 100 m length of optical fiber. Experimentally, a reduction in ultrasonic signal of ~10% was measured when the probe laser delivery fiber length was increased from 3 m to 100 m. The Fiber Coupling losses and attenuation of the 100 m fiber length resulted in an overall transmission efficiency of ~83%. Sustained output energies of 60 mJ were demonstrated at pulse repetition rates of 20 Hz.

**Table 5. Fiber and Lens Parameters for Fiber Coupling the Nd:YAG Probe Laser**

Long-Pulse Nd:YAG Probe Laser	Initial Configuration	Final Configuration
<b>Wavelength</b>	1064 nm	1064 nm
<b>Beam Diameter at Target</b>	~10 mm	~6 mm
<b>Fiber Type</b>	3M™ TECS™ FT-600-DMT	FiberGuide Industries Anhydroguide G, VIS-NIR
<b>Fiber Core Diameter</b>	600 $\mu\text{m}$	100 $\mu\text{m}$
<b>Fiber NA</b>	0.39	0.12
<b>Fiber Length</b>	100 m	3 m
<b>Coupling Lens</b>	$f = 102.01 \text{ mm}$ (Newport KPX094)	$f = 64.17 \text{ mm}$ (Newport KPX085)

After these initial experiments, the long-pulse Nd:YAG probe laser delivery fiber was changed from a 600  $\mu\text{m}$  core diameter, 0.39 NA fiber to a 100  $\mu\text{m}$  core diameter, 0.12 NA fiber. This design change for the final operating configuration was implemented since a systematic investigation of the energy loss through the Cassegrain subassembly (Appendix D) using ZEMAX showed that vignetting could be eliminated. Since the LPPL has a much lower peak-power than the Q-switched generation laser (1 kW versus ~50 MW) the reduction in fiber diameter can be afforded without risking catastrophic fiber breakage. With incident pulse energies of 1 mJ, transmission efficiencies of ~92% were recorded, which approaches the theoretical limit assuming 4% Fresnel losses at each fiber face.

#### 4.5.3.2 Power-Dependent Effects

It was noted that when coupling the LPPL into the optical fiber, spiking of the diode-pumped seed laser resulted in instabilities in the normally smooth long-pulse profile [25]. This was caused by sufficiently intense specular reflections from the coupling lens and the uncoated fiber entry face that leaked back into the diode-pumped seed laser. Although a Faraday isolator was present in the LPPL optical system, the extinction provided from a single device proved to be inadequate. The use of a second Faraday isolator, which provided an additional 40 dB of optical isolation, eliminated the problem and thus allowed the full optical power to be coupled into the optical fiber without any undesirable instabilities. It was also noted that the smaller core diameter fiber (100  $\mu\text{m}$ ) was particularly susceptible to significant back-reflection, which was possibly a result of stimulated Brillouin scattering, which is known to restrict the launch energy.

#### 4.5.4 Fiber Coupling of the Q-Switched Nd:YAG Generation Laser

##### 4.5.4.1 Coupling and Transmission Issues

The high peak-power of the Q-switched Nd:YAG generation laser precludes the use of small-core diameter fibers if laser pulses with sufficient energy for ultrasonic generation are to be delivered. The Fiber Coupling options that have been investigated with the Q-switched Nd:YAG generation laser are detailed in Table 6. Initial coupling efforts used a 3M<sup>TM</sup> TECS<sup>TM</sup>-coated silica/silica optical fiber which was designed for the delivery of high peak-power, Q-switched laser pulses. The fiber core diameter selected was 910  $\mu\text{m}$  with an NA of 0.22 and fiber length of 3 m. The input and output fiber faces were cleaved and terminated with a high-power SMA 905 connector.

**Table 6. Fiber and Lens Parameters for Fiber Coupling the Nd:YAG Generation Laser**

Q-Switched Nd:YAG Generation Laser	Initial Configuration	Final Configuration
Laser	Lumonics HyperYAG 750	Big Sky Laser Technologies (Model CFR 200)
Wavelength	532 nm	532 nm
Beam Diameter	10 mm	$\sim$ 6 mm
Fiber Type	3M <sup>TM</sup> TECS <sup>TM</sup> FG-910-UER	FiberGuide Industries Superguide G, VIS-NIR
Fiber Core Diameter	910 $\mu\text{m}$	1000 $\mu\text{m}$
Fiber NA	0.22	0.12
Fiber Length	3 m	3 m
Coupling Lens	f=30.29 mm (S&H 31 2331)	f=30.29 mm (S&H 31 2331)

The optical fiber launch geometry used to couple the Q-switched Nd:YAG generation laser was tailored in accordance with the criteria described in Section 4.4 for optimized coupling. A 10 mm aperture in front of the coupling lens limits the diameter of the incident generation laser. To fill the acceptance angle of the fiber to 80%, a simple plano-convex lens having a focal length of 30.29 mm at  $\lambda = 532 \text{ nm}$  is used. Further, the fiber entry face is located  $\sim$ 2 mm beyond the focal plane of the lens, allowing the incident laser beam to expand to fill  $\sim$ 80% of the fiber core. Under

these conditions and with the lens oriented for minimum spherical aberration, the minimum spot size is calculated to be  $\sim 80 \mu\text{m}$ . A laser beam with a 10 ns pulse duration and an energy of 25 mJ/pulse that illuminates a  $728 \mu\text{m}$  diameter region of the fiber input face will have a peak-power density of  $\sim 0.6 \text{ GW/cm}^2$ . This does not exceed the damage threshold of the optical fiber ( $1-5 \text{ GW/cm}^2$ ) at the input face of the fiber, which is consistent with our experimental observations where damage, when it did occur, was observed several millimeters beyond the input face.

Pulse energies of  $\sim 6 \text{ mJ/pulse}$  were successfully transmitted with low loss, and more importantly, without failure of the optical fiber. A plot of laser pulse energy, measured at the input to the optical fiber, versus the laser energy measured at the output of the 3 m length of optical fiber (Figure 25.) shows that the relationship is linear. Further, the results are repeatable, which indicates that no damage to the fiber occurred. The transmission efficiency is measured at  $>90\%$  which, assuming the inherent 4% Fresnel loss per entry and exit surface, indicates excellent coupling efficiency with only 2% additional loss. Further increases in delivery energy caused unexpected breakdown of the air. This resulted in a visible spark in front of the optical fiber. Although the breakdown does not result in damage to the fiber face, it prevents transmission of the laser energy to the optical fiber. The threshold for the onset of air breakdown is  $\sim 6.5-7 \text{ mJ}$  for the conditions in our laboratory. For the lens used, the expected minimum geometric spot size is on the order of  $\sim 80 \mu\text{m}$ , which results in a peak-power density of  $\sim 140 \text{ MW/mm}^2$  for a 7 mJ laser pulse with a 10 ns duration. This appears to be significantly below the expected threshold for air breakdown. One factor that can greatly reduce the threshold for air breakdown is dust. In an effort to eliminate the effects of particulate matter entering the focal volume, a gas line was configured to blow dry nitrogen across the volume. This did not affect the threshold for air breakdown.

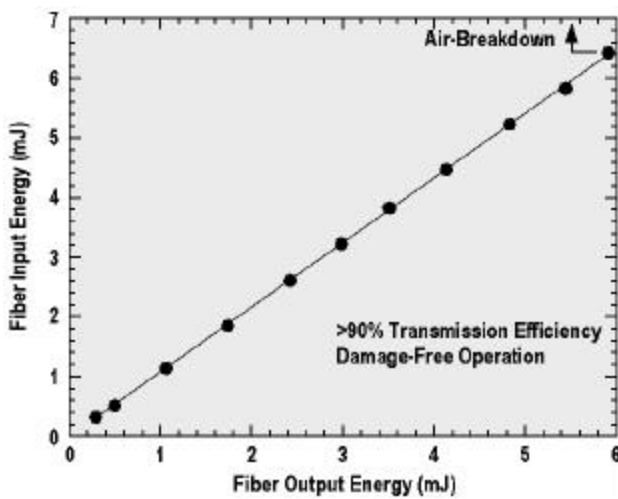


Figure 25. Q-Switched Laser Pulse Energy Measured at the Input to the  $910 \mu\text{m}$  Core Diameter Silica/Silica Optical Fiber versus the Laser Energy Measured at the Fiber Output

#### 4.5.4.2 Prevention of Air-Breakdown

An experimental vacuum cell (Figure 26) was fabricated to further investigate the maximum energy that could be delivered. The cell was fabricated from aluminum with a quartz window affixed to the input side and the connectorized fiber attached to the output side. With the vacuum

cell at atmospheric pressure, air breakdown continued to occur at  $\sim$ 7 mJ/pulse, which validated that the attenuation of the quartz window and its effect on the size of the laser beam focal spot were insignificant. When a “house vacuum” system was attached to the vacuum cell, a moderate vacuum was obtained with pressures maintained in the 457–585 Torr range (18–23 inches Hg). This was sufficient to inhibit air breakdown and allowed pulse energies  $>50$  mJ/pulse to be successfully transmitted through the cell. Coupling the laser pulses into the optical fiber through the vacuum cell resulted in successful delivery of 25 mJ/pulses to the target at pulse repetition rates of 20 Hz. However, while on one occasion this configuration operated successfully for an extended period ( $>1$  hour), a later test of the fiber system resulted in failure after  $\sim$ 10 minutes of continuous operation. The failure mode was gradual as the fiber melted at a distance of several inches from the input to the fiber. This again illustrates the difficulty in coupling high peak-power Q-switched laser pulses into optical fibers. It was not possible to determine the exact cause of the failure. However, this problem is believed to be caused by the poor beam quality of the Lumonics Q-switched Nd:YAG generation laser (Table 6) being used.

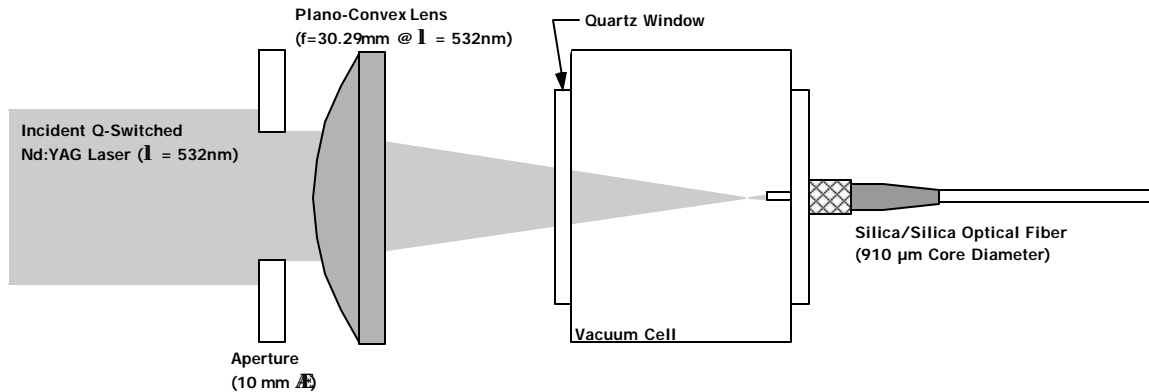


Figure 26. Experimental Vacuum Cell Configuration Used to Prevent Air-Breakdown when Coupling High Peak-Power Generation Laser Pulses into the Silica/Silica Optical Fiber

**4.5.4.3 Techniques for Smoothing the Q-Switched Nd:YAG Generation Laser Beam Profile**

Visual observations of the burn pattern produced by the Lumonics Q-switched Nd:YAG generation laser (Table 6) show inhomogeneities (hot spots) that cause the laser beam profile to deviate from a Gaussian distribution and support the presumption of poor beam quality. If these hot spots should become focused, they can lead to damage in an optical fiber as the beam propagates through it. To eliminate the hot spots, the energy distribution in the input laser beam should be smoothed out. Two methods were considered for smoothing the beam. One method uses an LSD (light-scattering diffuser) to randomly scatter the beam and homogenize it before focusing it and coupling it into the optical fiber. The second method uses a pinhole to spatially filter the beam before coupling it into the optical fiber.

The LSDs can be selected to scatter the light over a specified angle. The larger the angle, the more thoroughly the beam will be homogenized and thus smoothed. The difficulty arises from the angular spread of the beam from the source represented by the LSD and the requirement that the LSD must be imaged on the input face of the optical fiber. The nominal diameter of the beam from the laser is 10 mm. The core diameter of the largest optical fiber we are currently using is

0.91 mm. If a single lens is used to image the diffuser onto the fiber, the lens must be a high performance lens. Calculations of the maximum LSD scattering angle that can be used and still allow imaging of the LSD onto the fiber face show that a LSD does not offer a viable solution.

A second approach is to use a pinhole to spatially filter and thus smooth the laser beam. A lens is used to focus the beam so that it will pass through the pinhole. The lens is selected to have an NA that is 70% - 80% of the NA of the fiber. The pinhole is placed an appropriate distance away from the face of the fiber so that the diverging beam will cover 80% of the fiber face. To obtain good discrimination between the spatial frequencies of the 10 mm Gaussian beam and the spatial frequencies of the beam inhomogeneities (hot spots), the focused beam spot size should be made as small as possible, consistent with the NA requirements of the optical fiber. To accomplish this, it is necessary to use a high quality lens, such as an achromat. Even then there are several potential problems associated with using pinhole spatial filters with a Q-switched laser. First there is the difficulty of aligning it so that the full power of the laser beam is not focused on the pinhole substrate. Second, a small pinhole requires greater alignment accuracy and spatial stability of the laser from shot-to-shot. Finally, we already observed air breakdown, which occurred at ~6 mJ/pulse (Section 4.5.4.1) so that it would be required to use a vacuum spatial filter. We did not find a commercial source for these and preferred not to build our own unless it was absolutely necessary.

#### **4.5.4.4 New Q-Switched Nd:YAG Laser**

Given the difficulties in implementing either the LSD or a pinhole, it was decided that the most expeditious course of action was the to procure a Q-switched Nd:YAG laser (Model CFR 200) from Big Sky Laser Technologies. The laser generates simultaneous dual-beam output at both the fundamental (1064 nm) and first harmonic (532 nm). A separate aperture for each beam allows for the laser wavelengths to be used independently. The system was configured for selection of the first harmonic beam to allow issues regarding coupling of the Q-switched generation laser into optical fiber to be revisited.

Using the Big Sky Nd:YAG laser, a test was performed to establish the threshold for air breakdown. Using the same lens as used previously (SH31 2331, f=30.29 at 532 nm), we were able to deliver close to 90 mJ/pulse before the onset of air breakdown. This result greatly simplifies the coupling of light into the optical fiber since the vacuum cell is no longer required. Furthermore, this tends to confirm that the problems observed previously were caused by the inhomogeneous spatial beam profile of the Lumonics laser system. Experiments were continued to establish the maximum pulse energy that could be successfully coupled into a silica/silica optical fiber (910  $\mu\text{m}$  core diameter). We have demonstrated continuous transmission of pulse energies up to ~45 mJ/pulse for periods of 60 minutes without failures. These results emphasize the importance of using a Q-switched laser with good beam quality when coupling into optical fibers.

#### **4.5.5 Summary and Discussion**

Although the CO<sub>2</sub> laser has been a popular choice for LBU inspection systems, the operating wavelength ( $\lambda = 10.6 \mu\text{m}$ ) and the high peak-power laser pulses preclude the use of fiber-optic beam delivery over all but very short lengths (<1.5 m) of specialized optical fiber. Consequently the major portion of the effort was directed at the investigation of the frequency-doubled Q-switched Nd:YAG and alexandrite generating lasers since they can be transmitted efficiently over standard silica optical fiber. The results presented detail the procedures used to optimize fiber coupling of the LBU system generation and detection laser beams. Using an optical fiber launch geometry that is tailored to satisfy a set of empirical guidelines has produced rugged and damage-free beam delivery configurations.

The delivery of both the alexandrite generation laser pulses (65 mJ) and the long-pulse Nd:YAG probe laser pulses (60 mJ) has been successfully demonstrated over 100 m lengths of optical fiber at laser pulse repetition rates of 20 Hz. Furthermore, when coupling the long-pulse Nd:YAG probe laser and the alexandrite generation laser into 100 m lengths of optical fiber, flexing of the optical fibers did not affect the transmitted power. This was an expected result since, in fibers of this length, intramodal dispersion results in excitation of all of the allowed propagation modes, and thus the full NA is utilized. This is an important result, since the fibers flex during scanning of the Cassegrain optical system, and variations in the delivered generation or probe laser energies will result in fluctuations in the detected ultrasonic wave amplitude that cannot be easily compensated for. An additional important observation is that for a 3 m length of optical fiber the output beam diverges with the same NA as the input beam. However, for the 100 m length of fiber, the output NA is independent of the input NA because of intramodal dispersion. Based on the need to minimize vignetting in the Cassegrain subassembly relay optics (Appendix D), the final LPPL delivery configuration utilizes a 100  $\mu\text{m}$  core diameter optical fiber having an NA of 0.12 with fiber coupling efficiencies of ~90% and probe laser-to-target transmission efficiencies (i.e., fiber coupling and vignetting losses accounted for) measured at ~85%. This was a marked improvement over the initial fiber-delivery configuration, which resulted in high losses caused primarily by vignetting of the probe laser beam as it propagated through the Cassegrain subassembly relay optics.

Initial coupling experiments with the frequency-doubled Q-switched Nd:YAG laser used a silica/silica optical fiber (910  $\mu\text{m}$  core diameter). Laser pulses with energies of ~6 mJ/pulse were successfully delivered with low loss and, more importantly, without failure of the optical fiber. Spatial inhomogeneities in the beam were believed to cause air breakdown and fiber damage when the laser energy was raised above 6 mJ/pulse. This belief was validated by the installation of a Q-switched Nd:YAG laser (Big Sky Laser Technologies) that operated with a smooth spatial profile and permitted the propagation of ~90 mJ/pulse before the onset of air breakdown. This eliminated the complication of using a vacuum cell and enabled pulse energies of ~45 mJ/pulse to be robustly delivered. To avoid fiber damage from the high peak-power generation lasers and to minimize vignetting in the Cassegrain subassembly relay optics (Appendix D), the final generation laser delivery optical fiber system used a 1.0 mm diameter fiber with an NA of 0.12. This resulted in a 67% overall transmission efficiency through the Cassegrain subassembly relay optics, which was a substantial improvement over that obtained with the 0.22 NA fiber. Thus, a

25 mJ/pulse can be routinely delivered to the target, while still remaining below the damage threshold of the fiber input face, which is considered sufficient for most laser inspection applications.

## 5. GENERATION EFFICIENCY STUDIES

### 5.1 Absolute Thermoelastic Ultrasonic Wave Generation Efficiency in Polymer-Matrix Composite Materials

The incident generation laser pulse produces a localized transient heat source that generates localized strain fields resulting in the thermoelastic generation of ultrasonic waves. Thus for laser-based ultrasonics, unlike conventional ultrasonics, both the efficiency of the transduction process and the spatial distribution of the resulting ultrasonic waves are strongly influenced by the characteristics of the material being inspected [26,27]. Thus, for LBU the *material* is the transducer. To identify the optimum generation laser configuration, a comparative study was performed of the longitudinal wave thermoelastic generation efficiency of the CO<sub>2</sub> ( $I = 10.6 \mu\text{m}$ ), Q-switched Nd:YAG ( $I = 1064$  and  $532 \text{ nm}$ ) and Q-switched alexandrite ( $I = 720\text{-}800 \text{ nm}$ ) generating lasers when used to irradiate a series of polymer-matrix composite specimens (Figure 27). Cross-calibration of the SFPI with a Michelson interferometer (see Appendix E) enabled the absolute thermoelastic generation efficiency to be obtained.

Although not previously used in laser-ultrasonic studies, the Q-switched alexandrite generation laser was selected because of its compatibility with transmission through 100 m lengths of optical fiber [6]. The alexandrite laser pulse had a full-width-half-maximum (FWHM) duration of ~95 ns, with the Nd:YAG and CO<sub>2</sub> lasers having a pulse duration of ~17 ns and ~95 ns, respectively. The long-pulse Nd:YAG probe laser was used in conjunction with a 1 m SFPI to detect the ultrasonic waves received on the opposite side of the specimen (i.e., transmission mode). Previous diagnostics have indicated that the finesse of the SFPI system is degraded as the aperture size increases. This is caused by imperfections in the reflective optical coatings applied to the mirror surfaces and mirror surface figure. Thus, to ensure that the sensitivity of the SFPI was not appreciably different for materials having significantly different scattering cross sections, the 50 mm aperture of the SFPI was limited to 25 mm with a fixed aperture. Each of the generation lasers was constrained to a 5 mm diameter illumination source using a fixed diameter aperture close to the part surface and was operated at pulse repetition rates of 20 Hz and energy levels sufficiently low that damage was not observed in the polymer-matrix composite samples. For each generating laser, the average peak-to-peak longitudinal pulse amplitude and average incident laser energy were measured for 100 waveform acquisitions. Experimental results (Figure 27) show a comparison of the normalized longitudinal wave amplitudes resulting from each generation laser. The results displayed in Figure 27 are for specimen thicknesses of 5 mm. The effect of the different laser pulse durations was not taken into account in this analysis, since the goal was to select an optimum laser configuration for maximizing the LBU system SNR (SNR). The data plotted in Figure 27 are also documented in Table 7.

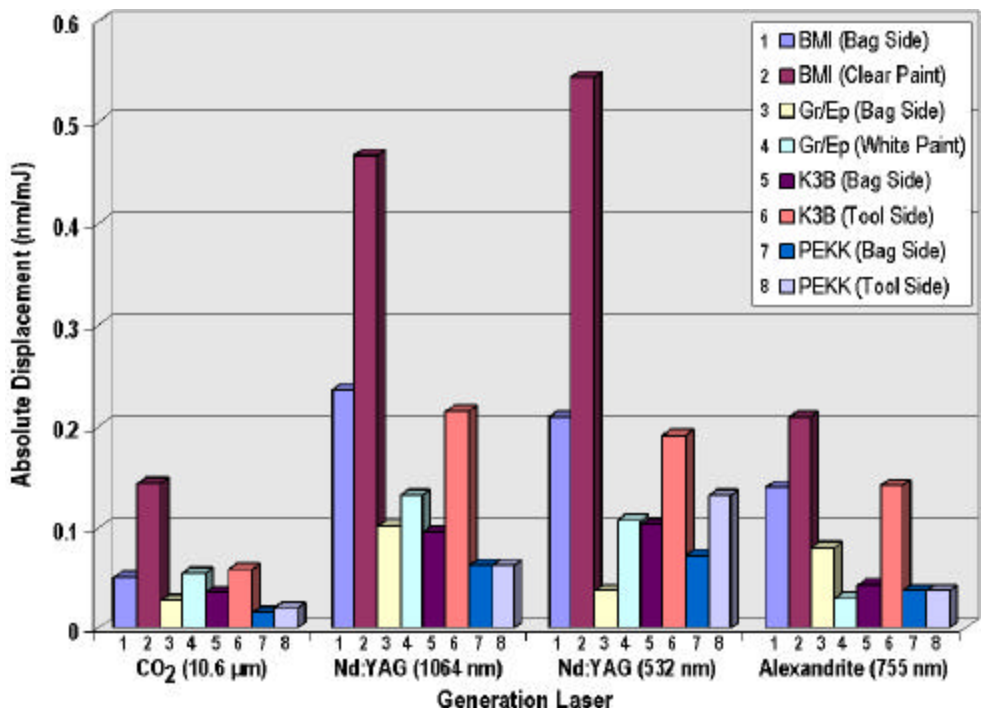


Figure 27. Absolute Longitudinal Wave Displacement for the CO<sub>2</sub>, Nd:YAG ( $\lambda = 532$  and 1064 nm) and Alexandrite Generating Lasers When Used to Irradiate a Series of Polymer-Matrix Composite Specimens

**Table 7. Thermoelastic Generation Efficiency in Polymer-Matrix Composites**

Sample Type	CO <sub>2</sub> (10.6 μm)	Nd:YAG (1064 nm)	Nd:YAG (532 nm)	Alexandrite (755 nm)
BMI (Bag Side)	0.050	0.235	0.208	0.139
BMI (Clear Paint)	0.144	0.466	0.545	0.209
Gr/Ep (Bag Side)	0.027	0.131	0.106	0.080
Gr/Ep (White Paint)	0.054	0.100	0.036	0.030
K3B (Bag Side)	0.035	0.095	0.103	0.043
K3B (Tool Side)	0.058	0.214	0.190	0.141
PEKK (Bag Side)	0.016	0.0614	0.072	0.038
PEKK (Tool Side)	0.020	0.0629	0.132	0.037

Comparison of this data set with results obtained previously for a bare graphite/epoxy specimen showed self-consistency for the two data sets. That is, for bare graphite/epoxy, the Nd:YAG laser at either the fundamental wavelength or first harmonic is most efficient for generation of ultrasound, followed by the alexandrite laser, and then the CO<sub>2</sub> laser. The generation efficiencies are markedly different for the four types of lasers for the different polymer-matrix composites investigated. This result is expected because of the different transmission characteristics of the epoxy resin as a function of incident generating laser wavelength. It can be seen that a higher generation efficiency was recorded for uncoated BMI compared with uncoated graphite/epoxy at the laser wavelengths investigated. For most materials investigated, the Nd:YAG laser yielded the

highest generation efficiency. One anomaly is that the alexandrite laser outperformed the Nd:YAG laser (at 532 nm) when inspecting the bag side of an uncoated graphite/epoxy specimen. Also, from Figure 27, in general the tool side of a part results in an enhancement of the generated ultrasonic amplitude. Unfortunately, however, the tool side is less desirable for inspecting in a scanning mode since the specularly reflected light, which is collected at near normal angles of incidence, results in excessive dynamic range requirements, which typically results in saturation of the detection electronics unless active control of the probe laser power is implemented.

Previous work [1,7] has shown that the transmittance through typical resins is highest for the Nd:YAG laser, followed by the alexandrite laser, so that the results for the experimentally determined generation efficiency are perhaps not unexpected. The CO<sub>2</sub> laser wavelength results in distributed absorption within the resin layer, thus generating a volumetric source as opposed to a buried source. A buried source is known to be more efficient for generation of ultrasonic waves than a volumetric source. Previously, surfaces coated with white polyurethane paint had produced significant improvements in ultrasonic generation efficiency. However, for the alexandrite laser, initial observations for a white-painted graphite/epoxy panel have produced unexpected results. Interestingly, in contrast with the Nd:YAG and CO<sub>2</sub> lasers, the alexandrite laser has reduced generation efficiency on white-painted graphite/epoxy. Based on the optical absorption determined using spectroscopic analyses of the resin, this is an unexpected result.

These are important results since the selection of the generation and detection lasers is a critical step in the process of optimizing the LBU system SNR. In addition to good thermoelastic generation efficiency, the Q-switched Nd:YAG laser can be transmitted efficiently over standard silica optical fibers at either of the two wavelengths investigated.

## 5.2 Effects of Coating Thickness on the Thermoelastic Generation Efficiency

Coatings on the surface of the structure being inspected also strongly influence the transduction efficiency [4,5]. Additionally we have found that the thermoelastic ultrasonic generation efficiency is strongly dependent on the thickness of white polyurethane paint used to obtain forward-directed longitudinal ultrasonic waves in a metal part. To determine the optimum paint thickness needed when inspecting a part with the LBU system, measurements have been made on a series of aluminum test samples that were coated with white polyurethane paint having thicknesses ranging from 13–71 μm (0.5–2.8 mils). The paint thickness was determined using a commercially available eddy current thickness gauge which had an accuracy of ± 1 μm. Figure 28 shows the variation in the thermoelastically generated longitudinal wave amplitude in an aluminum plate as a function of the applied paint thickness. Initially the paint was applied as a single layer. However, for thicker coatings it became necessary to apply multiple layers of paint to avoid nonuniformities in thickness caused by paint running. Figure 28 shows that as the paint thickness increased, so did the detected ultrasonic amplitude with the 71 μm (2.8 mil) thick paint layer providing the highest SNR. There is a discontinuity as the transition is made from single to multiple paint layers, but nevertheless Figure 28 shows that the generation efficiency is increased by 18× as the paint thickness is increased from ~13 μm to ~71 μm. Although a peak in ultrasonic generation efficiency was not reached in these experiments, additional oscillations, caused by reverberation within the paint layers, reduce the fidelity of the ultrasonic signal. Figure 29. illustrates the changes in the

duration of the reverberant longitudinal ultrasonic waves detected after thermoelastic excitation of an aluminum plate having different paint thicknesses applied to the surface. Paint thicknesses were (a)  $\sim 23 \mu\text{m}$ , (b)  $\sim 38 \mu\text{m}$ , (c)  $\sim 53 \mu\text{m}$  and (d)  $\sim 71 \mu\text{m}$ . At a paint thickness of  $71 \mu\text{m}$ , although the generation efficiency is high, the presence of the multiple paint layers causes a narrow banding of the ultrasonic signal, which ultimately will prevent resolution of the defects of interest.

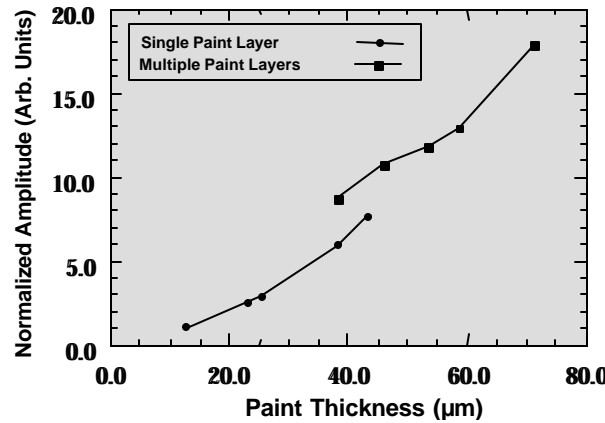


Figure 28. Plot Showing Variation in Thermoelastically Generated Longitudinal Wave Amplitude in an Aluminum Plate as a Function of the Applied Paint Thickness

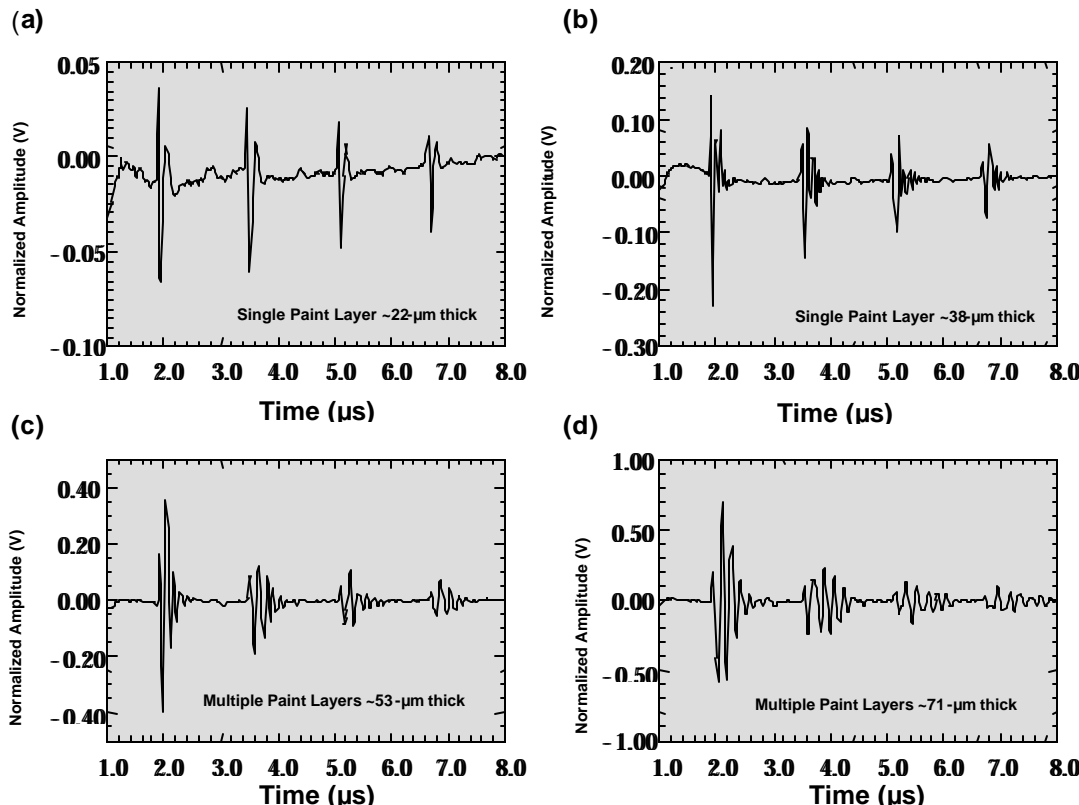


Figure 29. Reverberant Longitudinal Ultrasonic Waves Detected after Thermoelastic Excitation of an Aluminum Plate Having Different Paint Thicknesses Applied to the Surface. Paint Thicknesses Were (a)  $\sim 23 \mu\text{m}$ , (b)  $\sim 38 \mu\text{m}$ , (c)  $\sim 53 \mu\text{m}$  and (d)  $\sim 71 \mu\text{m}$ .

### **5.3 Summary and Discussion**

A comparison was made of the absolute thermoelastic generation efficiency of the Nd:YAG, alexandrite and CO<sub>2</sub> generating lasers when used for generation of longitudinal waves in several polymer-matrix materials and with different surface boundary conditions. The results indicate that in general, the Nd:YAG laser at either the fundamental wavelength or first harmonic is most efficient for generation of ultrasound. This result is significant since both the fundamental and first harmonic Nd:YAG laser wavelengths are compatible with transmission through standard silica fibers. Application of different-thickness paint layers to the surface of an aluminum plate was also investigated. Results indicate that the thickest paint layer resulted in the highest ultrasonic generation efficiency. However, this was accompanied by a corresponding reduction in the temporal bandwidth of the ultrasonic pulses. Thus, a trade-off exists between achieving maximum SNR and maintaining adequate defect resolution.

## **6. CONCLUSIONS AND SUMMARY**

The long-term objective of this research was to improve the quality and lower the cost of inspections for composite aircraft structures. By demonstrating that an all-fiber delivery system can be successfully used with laser-based ultrasonics, the opportunity exists to allow inspections to be carried out in areas of aircraft with restricted access. This can result in 1) significant cost savings since less tear-down of the aircraft is required, and 2) improvements in quality since it is practical to inspect limited-access areas of aircraft structures more frequently. Ultimately, the widespread use of laser-based ultrasonic technology throughout DoD, may well accommodate new assembly and fabrication methods and allow access to critical areas that now must have manhole-sized access ports or require extensive tear-down to obtain access.

The primary goal of this program was to demonstrate that it is feasible to construct an LBU system that employs a compact scanning head connected via optical fibers to the generation laser, probe laser, and the SFPI that is used to detect the ultrasonic signals. Further, it should be possible for the scan head to be remotely located at distances of 100 m from the lasers and SFPI. This significantly lowers the cost of the LBU system since the platform used to hold the scanning head can be of modest size rather than require a gantry crane to carry the generating laser and the collection optics. This was successfully accomplished through the design, manufacture and assembly of a compact fiber-coupled Cassegrain scanning system that was integrated into the LBU inspection system. The overall dimensions of the complete motorized scanning head are less than 12" x 9" x 22". The system developed allows operation, with minimum obscuration losses, at ranges of ~0.80-1.20 m and ~1.42–1.68 m based on two different secondary mirror configurations. The Cassegrain optical collection system was shown to have an off-axis optical power collection efficiency which exceeded that of a previously used galvanometer mirror system by ~16.4 $\times$ . Additionally, the Cassegrain system approach allowed the realization of decreased dynamic range requirements for the detection electronics. The fiber delivery of both the alexandrite and Q-switched Nd:YAG generation laser beams and the long-pulse Nd:YAG probe laser beam was successfully demonstrated.

A major accomplishment of the program was the successful design of the integrated scan head. The use of optical fibers to transmit the generation and probe laser beams from a remote location to the scan head and to transmit the probe laser light reflected from the target back to a remote location impose design constraints on the optics used with the scan head. Arrival at a final design was done using a combination of paraxial optical design analysis techniques to obtain insight into the issues and numerical ray-tracing techniques to correct for aberrations. Since the relay optics are located in a constrained space below the Cassegrain collection optics, it was found that it was best to use a design approach that imaged the faces of the fibers carrying the laser beams onto the target. This allowed the use of smaller diameter optical components. Since the size of the target spot and the ultimate étendue of the system were directly related, this placed significant restrictions on the diameters and NAs of the optical fibers. Successful trade-offs were possible that allowed target spot sizes of 8 mm to be achieved with transmission efficiencies through the relay optics of 67% for the generation laser and 87% for the probe laser.

The results of the analysis for optical collection of light reflected from the target show that it is advantageous to have a fiber with a large diameter and NA to obtain a large areal scan range without dynamically refocusing. Even so, severe limits are placed on the maximum diameters of the collection optics that can be used if practical-sized fibers are to be used ( $\leq 1.5$  mm core diameter). However, the use of relatively small diameter collection optics restricts the étendue of the system and, therefore, its sensitivity. If dynamic refocusing is used, larger collection optics can be used. This option is certainly feasible, but was not chosen in this program because of the already tight design requirements imposed by the compact integrated scan head and the limited resources available.

The realization of an all-optical fiber system requires that the generation and probe lasers be chosen with wavelengths that are compatible with the low-loss optical pass bands of the available optical fibers. This requirement dictated that the CO<sub>2</sub> laser, which is a popular choice for a generation laser for LBU inspection systems, not be used because of the unavailability of long length fibers that have low-loss pass bands at its wavelength of 10.6  $\mu\text{m}$ . Consequently, the major portion of the effort was directed at the investigation of the frequency-doubled ( $\lambda = 532$  nm) Q-switched Nd:YAG and alexandrite ( $\lambda = 755$  nm) generating lasers since they can be transmitted efficiently over standard silica optical fiber. The long-pulse Nd:YAG laser ( $\lambda = 1064$  nm) was chosen for the probe laser. The delivery of 65 mJ pulses from the alexandrite generation laser pulses and 60 mJ pulses from the long-pulse Nd:YAG probe laser pulses has been successfully demonstrated over 100 m lengths of optical fiber, at laser pulse repetition rates of 20 Hz. Although the transmission of 45 mJ pulses from the Q-switched Nd:YAG laser was demonstrated over only 3 m lengths of fiber, it is expected that there will be no difficulty in extending this to 100 m. As discussed in the report, a solution to problems associated with the successful transmission of the Q-switched pulses required the acquisition of a new laser with improved beam quality. Delivery of this item was late in the program and it was not possible to procure a 100 m length of 1 mm diameter, 0.12 NA fiber for the demonstration.

A secondary program goal was to determine the efficacy of using various lasers to thermoelastically generate ultrasound in various polymer-matrix composite materials. One of the advantages of using LBU for the inspection of complex-shaped materials is that the *material* is the transducer, and thus contour following systems are not required. Since each material can have a different thermoelastic response, it is essential that the thermoelastic generation efficiency be known for the specific materials that are to be inspected. In this program the absolute thermoelastic generation efficiency was established for four different laser wavelengths and eight different material/boundary conditions. It is significant that the Nd:YAG laser had the highest generation efficiency for most materials, since its wavelength is compatible with transmission through standard silica fibers. This program has shown that all-fiber delivery systems can be successfully used with laser-based ultrasonics. This will ultimately decrease the cost of such systems since the major elements can be concentrated in one location that is remote from the scan head. The techniques and technologies demonstrated in this program can be extended to allow inspections in areas of aircraft with restricted access. Thus, quality and safety will be improved through more frequent inspections without incurring the costs of extensive tear-down of the aircraft structure.

## 7. REFERENCES

- [1] A.D.W. McKie, R.C. Addison, Jr., *Ultrasonics* 32 (1994) 333-345.
- [2] M. Choquet, R. Héon, C. Padoleau, P. Bouchard, C. Néron, J.-P. Monchalin, *Rev. Prog. Quant. Nondestruc. Eval.* 14A (1994) 545-552.
- [3] C.J. Fiedler, T. Ducharme, J. Kwan, *Rev. Prog. Quant. Nondestruc. Eval.* 16A (1996) 515-522.
- [4] T.E. Drake, Jr., K.R. Yawn, S.Y. Chuang, M.A. Osterkamp, *Rev. Prog. Quant. Nondestruc. Eval.* 17A (1997) 587-593.
- [5] A.D.W. McKie, R.C. Addison, Jr., *Rev. Prog. Quant. Nondestruc. Eval.* 16A (1996) 523-530.
- [6] A.D.W. McKie and R.C. Addison, Jr., "Laser-Based Ultrasound Inspection with a Fiber-Based Scanning Cassegrain System" to be published in *Ultrasonics*.
- [7] A.D.W. McKie, R.C. Addison, Jr., *Rev. Prog. Quant. Nondestruc. Eval.* 12A (1992) 507-516.
- [8] Large Area Composite Inspection System, Contract # F33615-92-C-5983
- [9] A.D.W. McKie, R.C. Addison, Jr., *Rev. Prog. Quant. Nondestruc. Eval.* in press (1999)
- [10] A. Baranne, F. Launay, *Journal of Optics* 28 (1997) 158-172.
- [11] M. Hercher, "The Spherical Mirror Fabry-Pérot Interferometer," *Applied Optics*, Vol. 7, 1968, pp 951-966.
- [12] J.-P. Monchalin, R. Heon, Mater. Eval. 44 (1986) 1231-1237.
- [13] J.M. Vaughan, *The Fabry-Perot Interferometer: History, Theory, Practice and Applications*. Philadelphia: Adam Hilger, 1989.
- [14] Q. Shan, A.S. Bradford, R.J. Dewhurst, Meas. Sci. Technol. 9 (1998) 24-37.
- [15] R.J. Dewhurst, Q. Shan, Meas. Sci. Technol. 10 (1999) R139-168.
- [16] J.-P. Monchalin, R. Heon, P. Bouchard, C. Padoleau, Appl. Phys. Lett. 55 (1989) 1612-1614.
- [17] R.J. Dewhurst, Q. Shan, Meas. Sci. Technol. 5 (1994) 655-662.
- [18] R.C. Addison, Jr., A.D.W. McKie, Ultrasonics Symposium in press (1999).
- [19] S.W. Allison, G.T. Gillies, D.W. Magnuson and T.S. Pagano, Appl. Opt. 24 (19), 3140 (1985).
- [20] D.J. Anderson, R.D. Morgan, D.R. McCluskey, J.D.C. Jones, W.J. Easson and C.A. Greated, Meas. Sci. Technol., 6, 809 (1995).
- [21] T.G. De Hart, *Photonics Spectra*, November Issue, 107, (1992).

- [22] K. Leong and B.V. Hunter, in *Industrial Laser Review*, May Issue, 7 (1996).
- [23] C.C. Gregory, J.A. Harrington, *Appl. Opt.* 32 (1993) 3978-3980.
- [24] T.E. Drake, Jr., K.R. Yawn, S.Y. Chuang, M.A. Osterkamp, P. Acres, *Rev. Prog. Quant. Nondestruc. Eval.* in press (1999) .
- [25] A.D.W. McKie, R.C. Addison, Jr., *Rev. Prog. Quant. Nondestruc. Eval.* 13A (1993) 517-523.
- [26] C.B. Scruby, R.J. Dewhurst, D.A. Hutchins and S.B. Palmer, in *Research Techniques in Nondestructive Testing*, Vol. 5, ed. R.S. Sharpe, (Academic Press, New York, 1982), p. 281.
- [27] C.B. Scruby and L.E. Drain, *Laser Ultrasonics – Techniques and Applications* (Adam Hilger, New York, 1990).

## **8. LIST OF ACRONYMS**

<b>ACRONYM</b>	<b>DESCRIPTION</b>
CW	continuous wave
DLL	dynamic link library
FWHM	full-width-half-maximum
IR	infrared
LACIS-R	large area composite inspection system-rapid
LBU	laser-based ultrasound
LPPL	long-pulse probe laser
LSD	light scattering
NA	numerical aperture
NDE	nondestructive evaluation
OPD	optical path difference
PCS	plastic-clad silica
PZT	piezoelectric
RMS	root mean square
SFPI	SFPI
SMA	sub miniature assembly
SNR	SNR
STL	stereolithographic
TEA	transversely excited atmosphere
TTL	through the lens
UTC	Universal Technologies Corporation
UV	ultraviolet
ZPL	ZEMAX Programming Language

## Appendix A

### A1. Calculation of the Étendue for an SFPI

The operating characteristics of an SFPI system are ultimately defined by three fundamental parameters, namely the cavity length,  $r$ , the mirror reflectivity,  $R$ , and the wavelength of light,  $\lambda$ , used to illuminate the interferometer. A number of design decisions must be made before constructing an SFPI and the particular design parameters chosen are dictated by the particular application.

If the interferometer is to be used in a LBU system, it is desirable to have a detection bandwidth that is commensurate with the frequencies used to perform ultrasonic inspection. This is typically of the order of 10 MHz. The bandwidth, also known as the instrumental profile, of an SFPI is given by the following equation:

$$\Delta n = \frac{c(1 - R^2)}{4\pi r R}, \quad (\text{A-1})$$

where  $c$  is the velocity of light in the medium filling the cavity. To obtain the desired bandwidth it is necessary to choose values for both the mirror reflectivity and the interferometer cavity length. Ultimately, the longer the cavity length, the greater the étendue and hence the SNR. Having chosen a suitable cavity length, the mirror reflectivity required to obtain the desired bandwidth is obtained by solving Eq. (A-1) for  $R$ , which results in,

$$R = \frac{-\left(\frac{4\pi r \Delta n}{c}\right) \pm \sqrt{\left(\frac{4\pi r \Delta n}{c}\right)^2 + 4}}{2}. \quad (\text{A-2})$$

For a 500 mm long cavity and a 10 MHz bandwidth,  $R$  is given by the following equation:

$$R = \frac{-0.2094 \pm 2.01}{2}. \quad (\text{A-3})$$

Taking the positive root yields a value for  $R$  of  $\sim 0.9$ . Similarly, for a 1 m long cavity, to obtain the same bandwidth of 10 MHz, the mirror reflectivity must be  $\sim 81\%$ .

The étendue,  $U$ , may be written as the product of the effective source area,  $A$ , and the operational solid angle,  $\Omega$ , into which it radiates as the following equation shows:

$$U = A\Omega. \quad (\text{A-4})$$

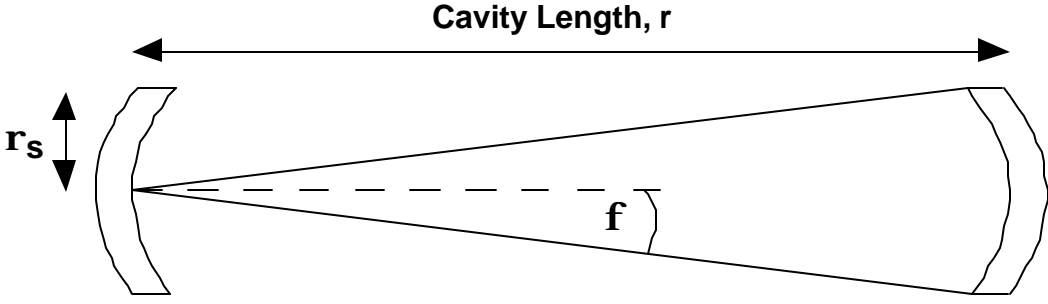


Figure A-1. Schematic of an SFPI

Referring to a schematic of the SFPI (Figure A-1), the étendue of the interferometer is given by the following equation:

$$U = (\mathbf{p} \mathbf{r}_s^2) \times 2 \mathbf{p} (1 - \cos \mathbf{f}), \quad (\text{A-5})$$

where  $\phi$  is the half angle and  $\rho_s$  is the radius of the mirror. Expanding  $\cos \mathbf{f}$  gives the following equation:

$$\cos \mathbf{f} = 1 - \frac{\mathbf{f}^2}{2!} + \frac{\mathbf{f}^4}{4!} - \frac{\mathbf{f}^6}{6!} + \dots, \quad (\text{A-6})$$

and for small angles  $\cos \mathbf{f}$  may be approximated by the following equation:

$$\cos \mathbf{f} \approx 1 - \frac{\mathbf{f}^2}{2!}. \quad (\text{A-7})$$

Substituting for  $\cos \mathbf{f}$  in Eq. (A-5) results in the following:

$$U = (\mathbf{p} \mathbf{r}_s^2) \mathbf{p} \mathbf{f}. \quad (\text{A-8})$$

Again, a small angle approximation may be made in which this time  $\phi$  can be approximated by the following:

$$\mathbf{f} = \frac{\mathbf{r}_s}{\mathbf{r}}, \quad (\text{A-9})$$

resulting in the following:

$$U = (\mathbf{p} \mathbf{r}_s^2) \left( \frac{\mathbf{p} \mathbf{r}_s^2}{\mathbf{r}^2} \right) \Rightarrow \frac{\mathbf{p}^2 \mathbf{r}_s^4}{\mathbf{r}^2}. \quad (\text{A-10})$$

This expression for the étendue is identical to the equations given by both Hercher (Eq. (29) in reference [11]) and Vaughan (p.192 in reference [13]). However, there is a discrepancy in their equations which define  $\rho_s$  in terms of  $\lambda$ ,  $\mathbf{r}$ , and  $U$ . Vaughan's definition of  $\rho_s$  is as follows:

$$\mathbf{r}_s = \left( \frac{2 \mathbf{r}^3 \mathbf{I}}{F_r} \right)^{\frac{1}{4}}. \quad (\text{A-11})$$

Whereas Hercher's definition of  $\rho_s$  is given by the following:

$$\mathbf{r}_s = \left( \frac{r^3 \mathbf{I}}{F_r} \right)^{\frac{1}{4}}, \quad (\text{A-12})$$

where  $\lambda$  is the wavelength of the illuminating radiation and  $F_r$  is the reflectivity finesse given by the following:

$$F_r = \frac{\mathbf{P}^R}{1 - R^2}. \quad (\text{A-13})$$

Hercher's definition will be used here. It follows from Eqs. (A-10) and (A-11) that the étendue may also be written as the following:

$$U = \frac{\mathbf{P}^2 r^3 \mathbf{I}}{F_r r^2} \Rightarrow \frac{\mathbf{P}^2 r \mathbf{I}}{F_r}. \quad (\text{A-14})$$

This expression is identical to that given by Hercher (Eq. (29) in reference [11]), but differs from Vaughan (p. 193 in reference [13]) by a factor of 2. Thus Eq. (A-14) represents the maximum étendue of the interferometer as defined by the mirror reflectivity, the mirror separation (cavity length), and the laser wavelength. A reduction in the interferometer étendue will occur if the aperture size of the interferometer is too small (i.e.,  $< 2 p_s$ ), in which case the étendue is limited by Eq. (10).

Consider the following two cases pertaining to the two Rockwell SFPI systems.

### Case A

For a 500 mm long cavity,  $R = 90\%$  and a laser wavelength of 514.5 nm using equations (A-12) and (A-13), the following equation applies:

$$\mathbf{r}_s = \left( \frac{500^3 \times 514.5 \times 10^{-6}}{14.88} \right)^{\frac{1}{4}} \Rightarrow \approx 8.11 \text{ mm}, \quad (\text{A-15})$$

i.e., this is the mirror radius that can be sustained to maintain the maximum étendue, limited only by  $\lambda$ ,  $r$  and  $R$ .

From Eq. (A-10) it follows that the maximum étendue is as follows:

$$U_{\max} = \frac{\mathbf{P}^2 \times 8.11^4}{500^2} \Rightarrow \approx 0.171 \text{ mm}^2 \cdot \text{sr}. \quad (\text{A-16})$$

This result could have been obtained directly from Eq. (A-14), as follows:

$$U_{\max} = \frac{\mathbf{P}^2 \times 500 \times 514.5 \times 10^{-6}}{14.88} \Rightarrow 0.171 \text{ mm}^2 \cdot \text{sr}. \quad (\text{A-17})$$

This interferometer has a aperture that is only 10 mm in diameter, so that the maximum étendue defined by Eq. (A-10) can no longer be achieved. Instead, the realizable étendue is reduced to the following:

$$U_{r_s=5} = \frac{P^2 \times 5^4}{500^2} \Rightarrow \approx 0.025 \text{ mm}^2 \cdot \text{sr} . \quad (\text{A-18})$$

### Case B

For a 1000 mm long cavity,  $R = 81\%$  and a laser wavelength of 1064 nm using Eqs. A-(11) and (A-12), the following equation applies:

$$r_s = \left( \frac{1000^3 \times 1064 \times 10^{-6}}{7.4} \right)^{\frac{1}{4}} \Rightarrow \approx 19.47 \text{ mm} . \quad (\text{A-19})$$

So to fully realize the maximum étendue in this interferometer, we need to use mirrors which have a clear aperture of at least 39 mm.

It has been assumed that in the absence of imperfections, the instrumental finesse is limited only by the value of the mirror reflectivity (Eq. (A-13)). This assumption has thus far been inherent in the above calculations for the étendue of the system. In practice it is necessary that the effects of mirror imperfections be considered. Hercher has analyzed the degradation of finesse caused by a number of factors. For an SFPI, in confocal adjustment, the significant factors in determining the instrumental finesse were found to be the reflectivity of the mirrors and their surface figure. Generally, if the mirrors have a smooth irregularity on the order of  $1/m$  across the aperture being used, then the mirror figure-limited finesse will be approximately as follows:

$$F_f \approx m / 2 . \quad (\text{A-20})$$

Hence for case B, a mirror with a figure of  $\approx \lambda/15$  could, in theory, be used, without reducing the finesse below that defined by the mirror reflectivity. A mirror figure of  $\lambda/15$  at 1064 nm is easily achieved and in this application it is desirable to specify a superior mirror figure of say  $\lambda/30$  at 1064 nm so that the finesse is governed solely by the mirror reflectivity.

### A2. Calculation of Effective Aperture of an SFPI

The expressions (Eqs. A-11 and A-12) derived for the effective aperture of an SFPI by Hercher [11] and Vaughan [13] differ by a factor of  $2^{1/4}$ . In order to determine which is correct, a model of the SFPI has been analyzed using the ZEMAX ray-tracing program to calculate the optical path difference (OPD) for each point on the aperture of the SFPI. The results of this calculation are used to determine the effective aperture of the SFPI. The model (Figure A-2) assumes that the input light rays are all parallel to the axis and do not pass through any optical components prior to entering the SFPI. In this model the system aperture is specified as an entrance pupil diameter of 50.8 mm. The wavelength was 1.064  $\mu\text{m}$ .

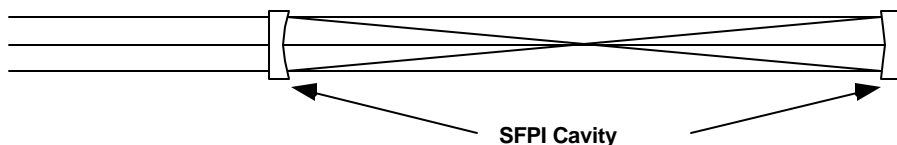


Figure A-2. Schematic Diagram of Model Used for Calculating the Effective Diameter of the Mirrors

The calculation of the effective aperture used a 256 x 256 element map of the OPD measured relative to the chief ray for rays reaching the output mirror on their first pass through the SFPI and a similar map of the OPD for rays reaching the output mirror on their fifth pass through the SFPI. Thus each ray had made four passes, through the SFPI between measurements. These two OPD maps were then subtracted to obtain the differential OPD for a ray after four passes through the SFPI. The theory for the SFPI [11,13] assumes that the rays retrace their paths after four passes through the cavity. This implies that the differential OPD will be the same for each successive set of four passes. This assumption was checked by measuring the differential OPD for a marginal ray for successive roundtrips (two passes) through the SFPI. It was found to be the same value to within  $\sim 0.008\%$  for the first six roundtrips. Further, the ray was essentially retracing its path after successive sets of four passes through the SFPI. The position of a marginal ray was changing only  $\sim 32 \mu\text{m}$  for each set of four passes for the model with the parallel input rays. It was concluded that it was valid to assume that the differential OPD for each successive set of four passes was the same and the change in the ray path was negligible.

If the on-axis separation between the SFPI mirrors is assumed to be an integral multiple of  $\pi$ , the output amplitude of the SFPI as a function of radial position,  $r$ , is given by the following:

$$S = \frac{1 - R}{1 - R^2 \exp(ik\mathbf{d}(r))}, \quad (\text{A-21})$$

where  $R$  is the mirror reflectivity and  $\delta(r)$  is the differential OPD at the radius  $r$  after four passes through the SFPI. The effective output amplitude of the SFPI is obtained by integrating  $S$  over the aperture.

$$\iint_{\text{area}} S r dr d\mathbf{f}. \quad (\text{A-22})$$

Since the OPD map is made up of 256 x 256 elements, the integral becomes a sum over  $n$  and  $m$ . The aperture is represented by a circle inscribed within the array of elements. Those elements outside of the circle have a value of zero. The output amplitude at each element has a different phase, so the sum will be less than would be obtained if  $\delta = 0$ . The effective output amplitude is given by the following equation:

$$S_{\text{eff}} = \frac{1}{N} \sum_{n,m}^{256} S_{n,m} \times (\text{aperture area}), \quad (\text{A-23})$$

where  $N$  is the number of elements within the circle. The effective diameter of the aperture is given by the following equation:

$$D_{\text{eff}} = 2\sqrt{\frac{S_{\text{eff}}}{p}}. \quad (\text{A-24})$$

The results of this calculation for mirror reflectivities of 0.81% and 0.93% are listed in Table 1. Also listed in Table A-1 are the results obtained using the formulas provided by Hercher (Eq. (12)) and Vaughan (Eq. (11)).

**Table A-1 Comparison of Effective Mirror Diameters for Two Reflectivities**

Mirror Reflectivity (%)	“OPD” Effective Diameter (mm)	“Hercher” Diameter (mm)	“Vaughan” Diameter (mm)
0.81	39.0	38.9	46.3
0.93	30.9	29.8	35.4

The results calculated using ZEMAX agree well with those obtained using Hercher’s formula. The slight discrepancy may occur because Hercher is assuming that there is a phase error, but there is no change in the ray path. The ZEMAX calculation includes both the phase change as well as the slight change in the ray path. Although the formula derived by Vaughan may be valid for a certain set of assumptions, it does not appear to be valid for the SFPI mode of operation being used for these experiments.

## Appendix B

### B1. Analysis of Light Collection from the Target to the Receiving Optical Fiber

Ideally, the focused output of the Cassegrain optical collection system should be coupled into an optical fiber which is located at the prime focus of the optical collection system and provides a flexible transmission path to the optical detection system. The range and angle of incidence (for inspection of a flat panel) are at a minimum when the optical axis of the Cassegrain scanner is perpendicular to the target surface, and are at a maximum when it is pointed at the corners of the inspection area. Thus, the distance between the secondary mirror and the image plane varies during a raster scan, and minimization of the optical collection loss at the receiving optical fiber must be considered. Two approaches may be pursued. Either the distance between the fiber entry face and the secondary mirror can be varied to track the image plane as the Cassegrain scan head deflects the probe laser beam over the inspection area, or the distance can be fixed at an optimum location for a specified operational range. For our initial Cassegrain system design, we chose to fix the distance between the fiber entry face and the secondary mirror. We have done a paraxial analysis of the limitations placed on the size of the collecting fiber by the other system parameters, which is presented in Section B1.1. The analysis of the light coupling through the Cassegrain optics and into the fiber was done using a numerical ray-tracing technique and is presented in Section B1.2.

#### B1.1. A Paraxial Analysis

The parameters that influence the required diameter of the optical fiber are the range to the target, the diameter of the light source at the target, the diameter of the collection lens, and its focal length. The source is assumed to be radiating isotropically. A sketch of the optical layout is shown in Figure B-1. The initial calculations assume that the target is 5 ft (1524 mm) from the lens and that the spot from the probe laser is scanned over a square area that is 6 ft x 6 ft (~ 1829 mm x 1829 mm). Therefore, the range to the target varies from a minimum of 1524 mm to a maximum of ~1999 mm. The distance from the lens to the input face of the optical fiber is fixed. As the range changes, the image plane of the target spot will move relative to the fiber face. There are two rays that are key to determining the optimum location of the fiber to minimize losses. One of these is the ray that originates from the center of the target spot and travels to the periphery of the lens. The other is the ray that originates on the periphery of the target spot and travels to the periphery of the lens. When the target spot is at its minimum range, its image plane is at its maximum distance from the lens. The ray that is coming to focus on-axis will be the outermost ray in the input plane of the fiber (Figure B-2a). Alternatively when the target spot is at its maximum range, its image plane is at its minimum distance from the lens. The ray that is coming to focus at the periphery of the image will now be the outermost ray in the input plane of the fiber (Figure B-2b). It is important that the input face of the fiber be located such that the height of each of these two rays is equal for each of the extreme positions of the target spot. When this is done, we find that there is a relationship between the focal length of the lens and the reduction in the size of the target spot when it is focused on the input face of the fiber. This relationship is used to determine the maximum ray height in the input plane of the fiber when the target spot is at one of its extrema.

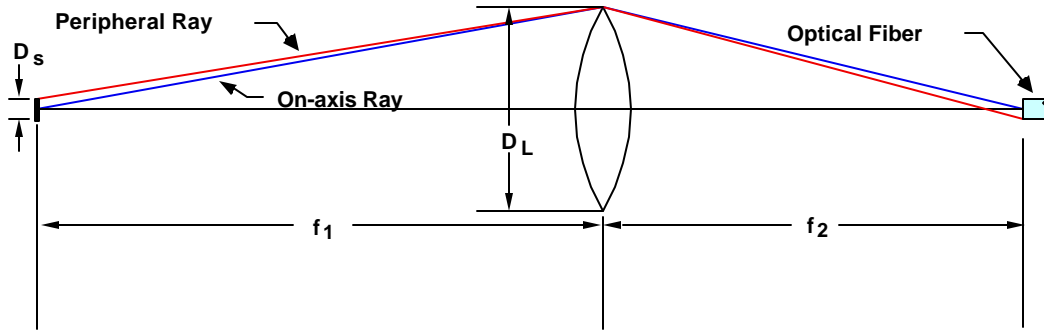


Figure B-1. Optical Layout for Calculating the Required Fiber Diameter Needed to Collect All of the Light Transmitted by the Lens at Both the Minimum and Maximum Range of the Target

Equation B-1 gives the ray height at a distance  $z$  from the lens for a ray originating from a height  $y_s$  on the target spot.

$$y = \frac{D_L}{2} - \left( \frac{D_L}{2} + \frac{y_s}{\left( \frac{f_1}{f} - 1 \right)} \right) \frac{z \left( \frac{f_1}{f} - 1 \right)}{f_1}, \quad (\text{B-1})$$

where  $D_L$  is the lens diameter,  $f$  is the lens focal length, and  $f_1$  is the target spot to lens distance (range). The magnitudes of the ray heights for the on-axis ray ( $y_s = 0$ ) and the peripheral ray ( $y_s = D_s/2$ ) are set equal.

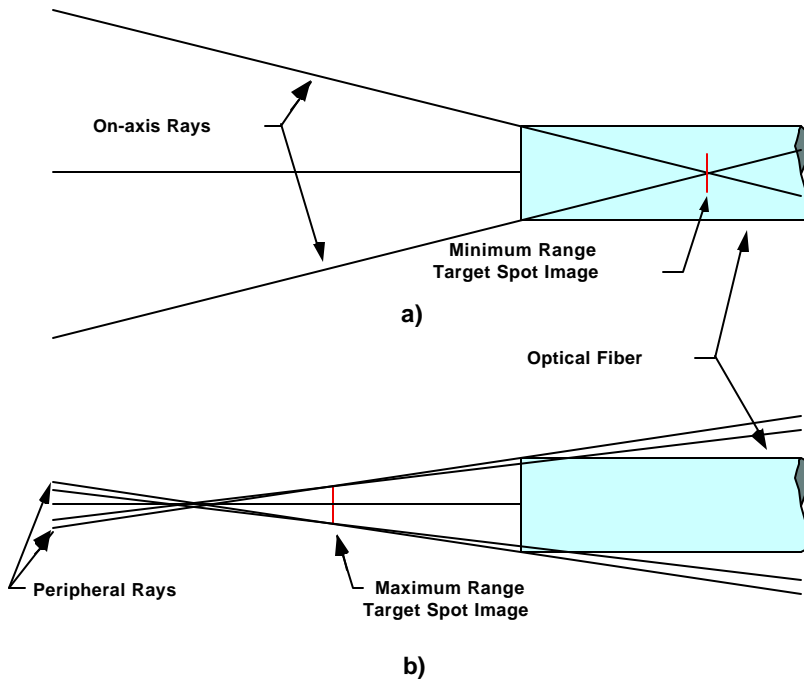


Figure B-2. Optical Rays Vignetted when the Target Spot is at a) Its Minimum Range, and b) Its Maximum Range.

Note that the sign of the height of the peripheral ray will be negative. We obtain the following:

$$\frac{D_L}{2} - \left[ \frac{D_L}{2} + 0 \right] \frac{z \left( \frac{f_{1\min}}{f} - 1 \right)}{f_{1\min}} = -\frac{D_L}{2} + \left[ \frac{D_L}{2} + \frac{D_s/2}{\left( \frac{f_{1\max}}{f} - 1 \right)} \right] \frac{z \left( \frac{f_{1\max}}{f} - 1 \right)}{f_{1\max}}. \quad (\text{B-2})$$

Referring to Figure B-1,  $z$  is the back focal plane of the lens, which is alternatively designated  $f_{2z}$  when the target spot is focused on the face of the fiber. The lens formula gives the following expression:

$$f_{2z} = \frac{f_{1x}}{\left( \frac{f_{1x}}{f} - 1 \right)}. \quad (\text{B-3})$$

Further the reduction ratio,  $n$ , is given by the following:

$$n = \frac{f_{1z}}{f_{2z}} = \left( \frac{f_{1z}}{f} - 1 \right). \quad (\text{B-4})$$

Substituting, we obtain the following:

$$f_{2z} = \frac{(n+1)f}{n}. \quad (\text{B-5})$$

When Eq. (B-3) and Eq. (B-5) are substituted into Eq. (B-2), we obtain the following relationship between  $f$  and  $n$ :

$$f = \frac{2}{n+1} \frac{1}{\left( \frac{1}{f_{1\max}} + \frac{1}{f_{1\min}} \right) - \frac{D_s/D_L}{f_{1\max}}}, \quad (\text{B-6})$$

or

$$f(n+1) = c, \quad (\text{B-7})$$

where

$$c = \frac{2}{\left( \frac{1}{f_{1\max}} + \frac{1}{f_{1\min}} \right) - \frac{D_s/D_L}{f_{1\max}}}. \quad (\text{B-8})$$

When Eq. (B-6) is substituted in Eq. (B-1) and either  $f_1 = f_{1\min}$ ,  $y_s = 0$  or  $f_1 = f_{1\max}$ ,  $y_s = D_s/2$ , we obtain the maximum ray height at the input face of the fiber as a function of the lens focal length,  $f$ . This is plotted in Figure B-3 for  $D_L = 40$  mm,  $D_s = 5$  mm,  $f_{1\min} = 1524$  mm, and  $f_{1\max} =$

1998.71 mm. Note that the shorter the focal length, the smaller the maximum ray height. However, the NA of the optical fiber sets a limit on the minimum value of  $f$ . The NA is given in terms of  $f_2$  as the following:

$$NA = \sin\left(\tan^{-1}\left(\frac{D_L/2}{f_2}\right)\right). \quad (B-9)$$

The minimum lens focal length,  $f$ , is given by the following:

$$f_{min} = \frac{\frac{1}{\tan(\sin^{-1}(NA))}}{\frac{D_L/2}{f_{max}}} + \frac{1}{f_{max}}. \quad (B-10)$$

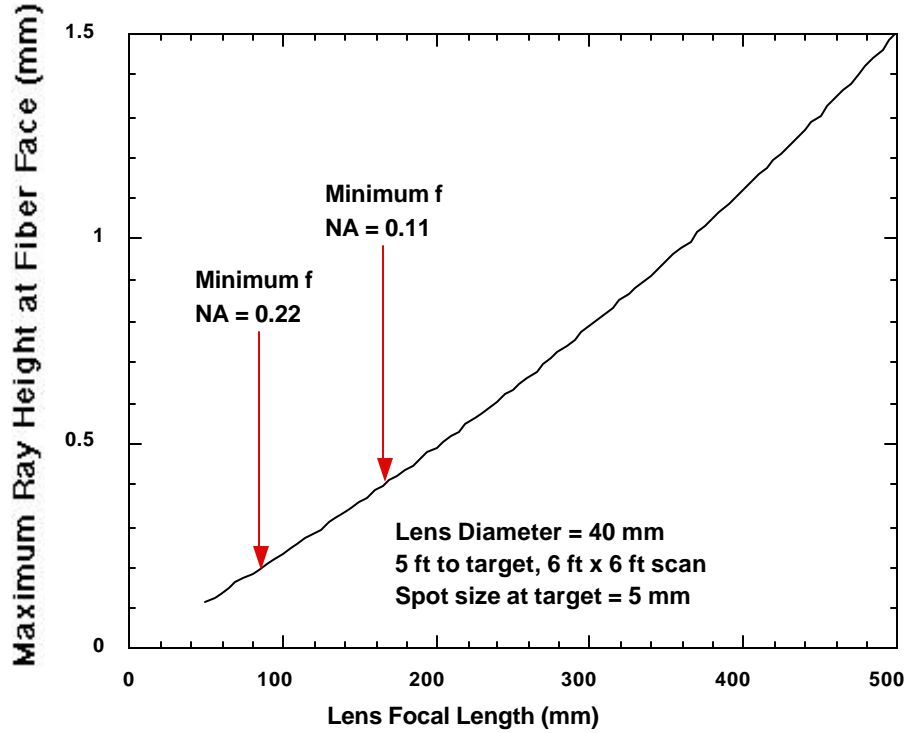


Figure B-3. Maximum Ray Height at Fiber Face as Focal Length of Light Collecting Lens Varies

For a fiber with an NA of 0.22,  $f_{min} = \sim 92.8$  mm, whereas for a fiber with an NA of 0.11,  $f_{min} = \sim 198.7$  mm. For the 0.11 NA fiber, we will choose  $f = 200$  mm and a lens diameter of 40 mm. The expression for the ray height at the fiber in terms of the range ( $f_1$ ) and the ray height on the target spot ( $y_s$ ) is as follows:

$$y_0 = \frac{D_L}{2} \left[ 1 - \left( 1 + \frac{2y_s/D_L}{\left( \frac{f_1}{f_{min}} - 1 \right)} \right) \right] \left( \frac{c}{\frac{c}{f_{min}} - 1} \right) \left( \frac{\frac{f_1}{f_{min}} - 1}{f_1} \right). \quad (B-11)$$

The absolute value of  $y_0$  is plotted in Figure B-4 for  $y_s = 0$  and 2.5 mm. The maximum value of  $y_0$  occurs at the extrema for  $f_l$  and is equal to ~0.49 mm. Thus a 1 mm core diameter fiber can be used to collect the light.

For our current Cassegrain collection system, the relevant scan parameters are a target distance of 40 inches (1016 mm) and a scan area of 4 ft x 4 ft (~1219 mm x 1219 mm). These values are used to calculate the minimum (1016 mm) and maximum (1332 mm) range shown in Figure B-5. The maximum value of  $y_0$  is ~0.36 mm. Thus a 0.75 mm core diameter fiber can be used to collect the light. Further analysis shows that the required fiber diameter increases rapidly as the diameter of the lens increases. This dependence is shown in Figure B-6 for several combinations of the target distance and the scan area. This calculation assumes that the NA of the fiber is constant at 0.22 and the focal length of the lens is the minimum possible for this NA. For the scan parameters relevant to our program, the required fiber diameter exceeds 1.5 mm for lens diameters greater than about 100 mm. This data is also presented in Figure B-7 for a fiber NA of 0.11. The results are somewhat anti-intuitive in that it seems that for a given lens diameter, the required fiber diameter should get larger when the fiber's NA increases. However, the lens focal length is not constant, and the étendue of the system is not constant for the various calculations.

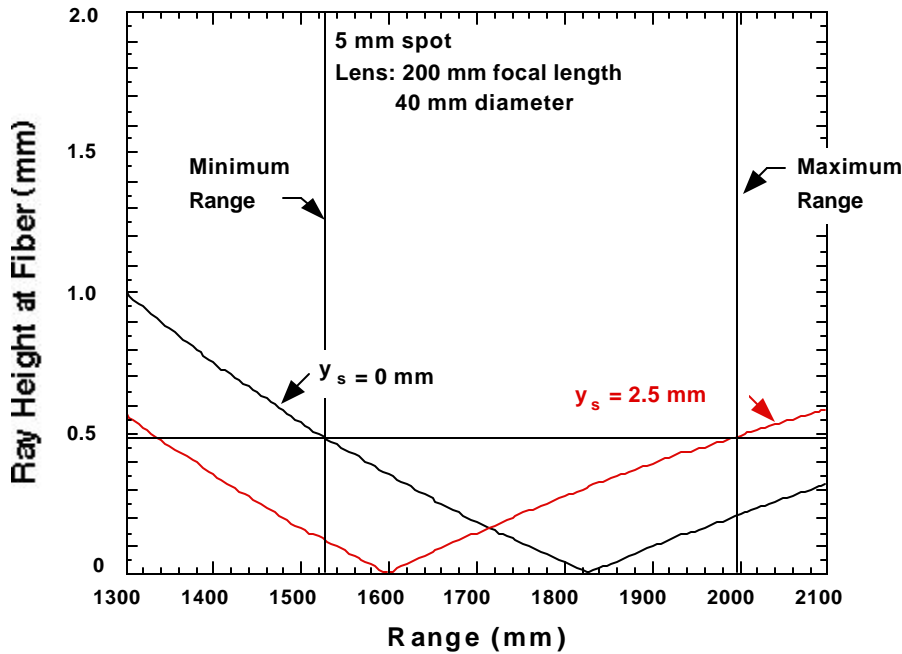


Figure B-4. Absolute Value of Ray Height at Fiber Face versus Minimum and Maximum Ranges are Based on a Target Distance of 5 ft and a Scan Area of 6 by 6 ft

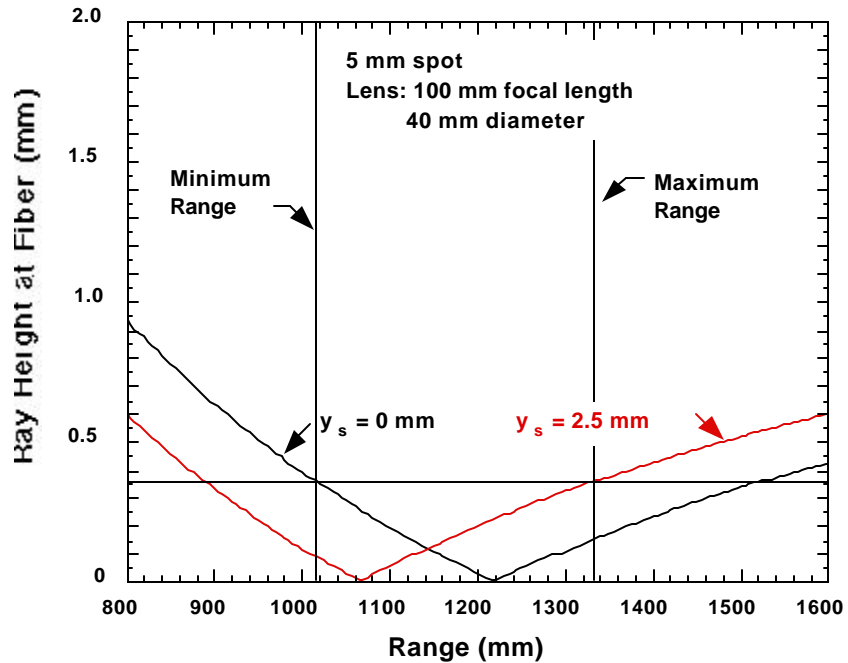


Figure B-5. Absolute value of Ray Height at Fiber Face versus Minimum and Maximum Ranges Based on a Target Distance of 40 Inches and a Scan Area of 4 by 4 ft

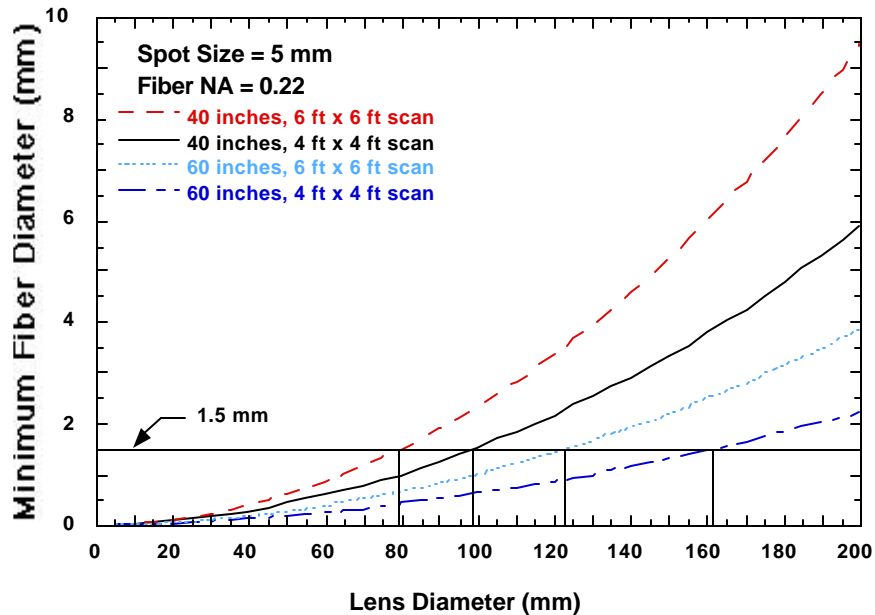


Figure B-6. Minimum Required Fiber Diameter to Collect All of the Light versus Lens Diameter for a Fiber NA of 0.22. Lens Diameters for a Fiber Diameter of 1.5 mm are Marked

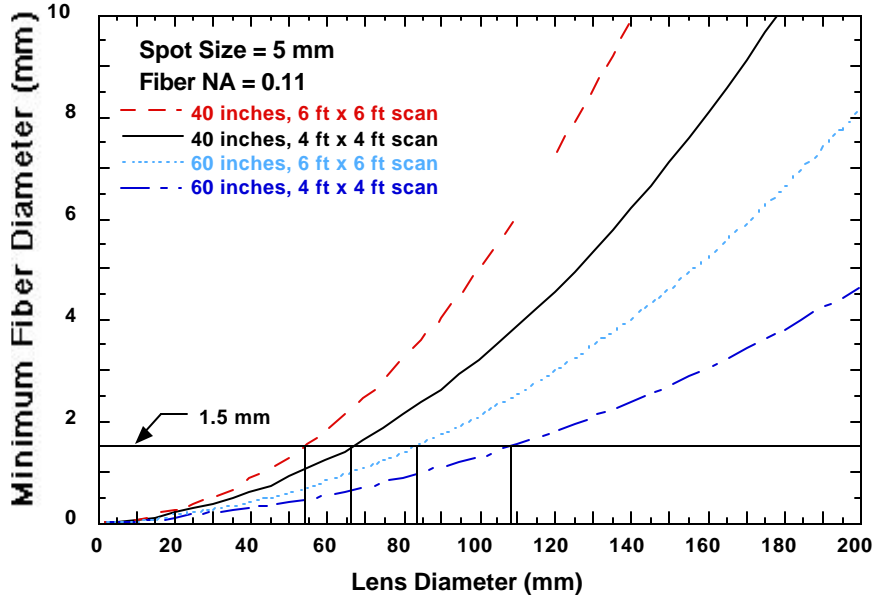


Figure B-7. Minimum Required Fiber Diameter to Collect All of the Light versus Lens Diameter for a Fiber NA of 0.11. Lens Diameters for a Fiber Diameter of 1.5 mm are Marked.

The results of this paraxial analysis of the optical collection of light reflected from the target show that it is advantageous to have a fiber with a large diameter and NA to obtain a large areal scan range without dynamically refocusing. Even so, severe limits are placed on the maximum lens diameters that can be used if practical-sized fibers are to be used ( $\leq 1.5$  mm core diameter). The use of the relatively small lens diameters restricts the étendue of the system and, therefore, its sensitivity. If dynamic refocusing is used, larger lenses can be used. If the results of these calculations are used to select the lens focal length, it will relax the accuracy requirements of the range finder.

### B1.2. An Optical Ray-Tracing Analysis

Figure B-8 shows the optical configuration for modeling the obscuration losses associated with the Cassegrain optical scanning system. Both ZEMAX and OptiCAD design models have been implemented for simulating the use of both a single large-core optical fiber and a coherent optical fiber bundle to collect the light at the prime focus of the Cassegrain system.

Figures B-9 and B-10 show calculations for the full Cassegrain system obscuration analysis (near-range configuration which uses a plane secondary mirror) which take into account obscuration caused by the secondary mirror, spider assembly and overfilling of the optical fiber. In both the OptiCAD model and the ZEMAX models, the source was assumed to be circular with a diameter of 5.85 mm. This source radiated uniformly over a full-divergence angle of  $8.7^\circ$ . In both models, the starting points and angles of the rays were selected randomly. In the OptiCAD model, 10,000 rays were used for each range, while 100,000 rays were used in the ZEMAX model. As seen in Figure B-9, the obscuration results obtained at the input to the 1.5 mm diameter fiber from the two modeling programs are in excellent agreement. An obscuration of

1.0 means that no light rays reached the detector. At the near range, this is caused by the secondary mirror or spider assembly completely blocking the rays radiating from the source. For the 1.5 mm diameter optical fiber with an NA of 0.38, Figure B-9 shows that a maximum of ~80% of light is transmitted into the fiber. Further, the light transmitted into the fiber is always less than the light transmitted into the 7 mm fiber bundle even at the optimum range. This implies that the spot size always slightly exceeds the fiber diameter. Away from the optimum range of ~1150 mm, the obscuration increases rapidly as the blur circle greatly exceeded the diameter of the fiber and increased the loss. This resulted in a much reduced optimum operational range compared with the optical fiber bundle which was anticipated. Further modeling in OptiCAD allowed the light transmitted through the fiber to also be calculated, thereby taking into account any skew rays that might enter the fiber but exceed the NA of the optical fiber and therefore be lost. This resulted in an additional ~14% loss. Similar analyses are shown for a 2 mm diameter fiber (NA=0.38) in Figure B-10. At the optimum range of ~1150 mm, the 2mm fiber is large enough to collect all of the light as evidenced by the fact that the data intersects the curve for the fiber bundle. Also, ~90% of the scattered light reached the input to the fiber with an additional ~16% loss after propagation through the fiber. It should be noted that these analyses have excluded any Fresnel losses at the fiber entry and exit faces.

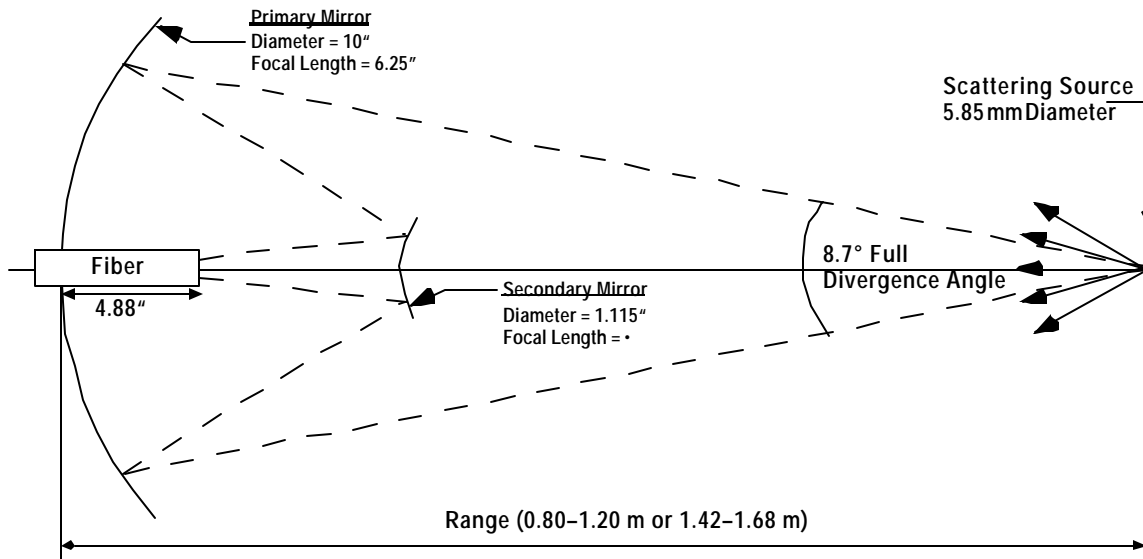


Figure B-8. Schematic Diagram Illustrating the Relevant Parameters Used for the Analytical and Ray-Tracing Obscuration Analyses

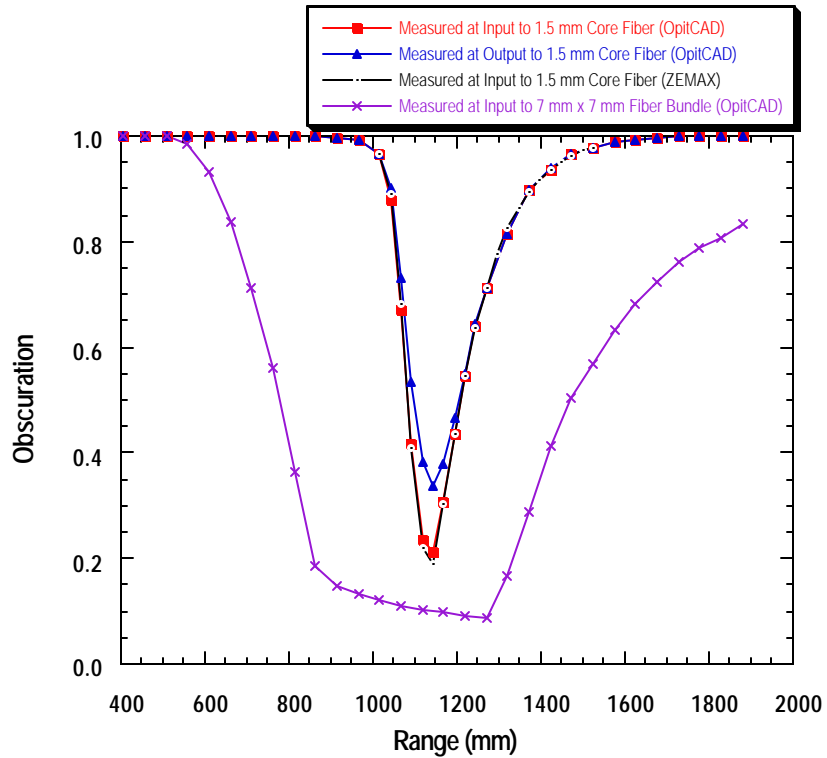


Figure B-9. Cassegrain System Obscuration Calculations for a 1.5 mm Core Diameter Optical Fiber and a 7 by 7 mm Optical Fiber Bundle

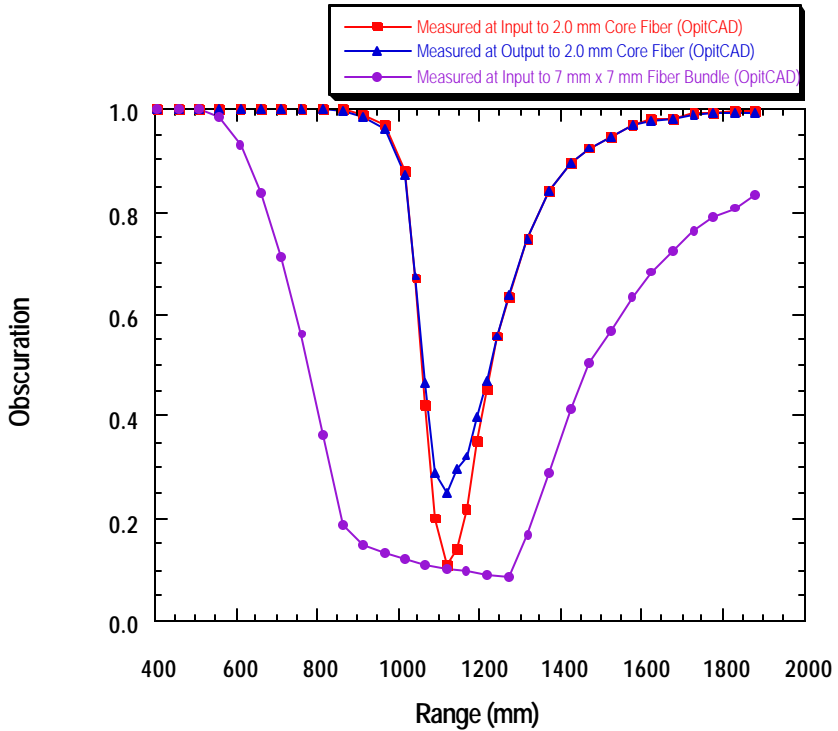


Figure B-10. Cassegrain System Obscuration Calculations for a 2.0 mm Core Diameter Optical Fiber and a 7 by 7 mm Optical Fiber Bundle

In summary, the results of the full obscuration analyses show that a 1.5 mm diameter fiber ( $NA=0.38$ ) will allow ~80% of the light scattered from a 5.85 mm diameter spot within a full-divergence angle of  $8.7^\circ$  to be incident on the fiber entry face. There is an additional ~14% loss caused by blockage of skew rays that exceed the NA of the optical fiber. Similar analyses for a 2 mm diameter fiber ( $NA=0.38$ ) show ~90% of the scattered light reaching the input to the fiber and an additional ~16% loss after coupling into the optical fiber. It should be noted that these analyses have neglected any Fresnel losses at the fiber entry and exit faces.

## B2. Analysis of Light Coupling from the Receiving Optical Fiber to the SFPI

There can be optical losses due to vignetting when the light reflected from a target or emitted from an optical fiber is coupled into an SFPI using a lens. It is useful to perform some simple paraxial optics calculations to obtain an estimate of the minimum optical beam diameters obtainable at the output mirror of the SFPI. This provides insight into the best lens to use for maximizing the coupling efficiency of the light from either the target or the optical fiber into the SFPI. A more accurate calculation of the losses can then be made using a numerical ray-tracing program that models a specific lens design.

### B2.1. A Paraxial Analysis

In these paraxial analyses, we will assume that the SFPI is 1m long and the mirrors have a diameter of 50 mm, which reflects the dimensions of one of the SFPIs currently being used at Rockwell. The analyses also assume that the light is coupled into the SFPI using a single lens that is located 260 mm from the input mirror of the SFPI, and the lens is assumed to be a thin lens that is free of all aberrations with a focal length,  $f$ . Finally the source is assumed to have a diameter,  $d$ , and an  $\text{NA} = \sin \theta$ . The analyses consider two separate cases that are described below.

## Analysis 1

The first analysis considers a situation that is similar to the one that has been used experimentally. The location of the source is constrained to be at the focal point of the lens. Thus the light being emitted on-axis will be collimated parallel to the optical axis. The light being emitted off-axis will also be collimated, but will not be parallel to the optical axis (Figure B-11).

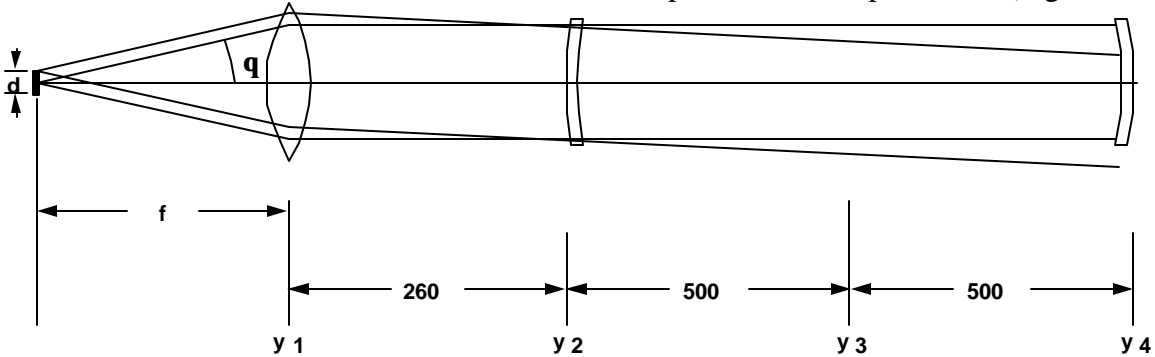


Figure B-11. Sketch of Optical Layout for Analysis of Coupling Losses when Using a Lens that Collimates the Light from the Source Prior to Passing through the SFPI

In Figure B-11, it can be seen that the marginal ray at the exit mirror of the SFPI arises from the edge of the source and travels at an angle,  $-\theta$ , with the optical axis, where  $\theta$  is given by Eq. (B-12):

$$\mathbf{q} = \sin^{-1}(NA). \quad (\text{B-12})$$

Referring to Figure B-11, the height of this marginal ray when it reaches the lens ( $y_1$ ) is given by the following:

$$y_1 = \frac{d}{2} - f \tan(\mathbf{q}). \quad (\text{B-13})$$

The slope of this ray after being refracted by the lens is given by the following:

$$\text{slope} = \frac{d}{2f}. \quad (\text{B-14})$$

The equation for the height of the marginal ray as a function of the distance,  $x$ , along the optical axis is given by the following:

$$y = \left( \frac{d}{2} - f \tan(\mathbf{q}) \right) - \frac{d}{2f}x. \quad (\text{B-15})$$

By substituting the value of  $x$  at the output mirror of the SFPI into Eq. (B-15), we obtain an expression for  $y_4$  as a function of the focal length,  $f$ . The minimum of this expression is found by setting the derivative equal to zero and solving for  $f$ . The minimum marginal ray height at the output mirror of the SFPI occurs for the value of  $f$  given by the following:

$$f = \sqrt{\frac{630d}{\tan(\mathbf{q})}} = 175.680. \quad (\text{B-16})$$

This expression is substituted into Eq. (B-15) to obtain the value of  $y$  as a function of  $x$  for the value of  $f$  that provides the minimum value of  $y_4$ , as shown in the following:

$$y = \left( \frac{d}{2} - \sqrt{630d \tan(\mathbf{q})} \right) - \sqrt{\frac{d \tan(\mathbf{q})}{2520}}x. \quad (\text{B-17})$$

The values of  $2y|_{f_{\text{opt}}}$  (i.e., the minimum diameter of the beam) at various locations are given in Table B-1 for  $d=10$  mm and  $\theta=11.537^\circ$ . Note that the minimum beam diameter at each of the mirrors is greater than the mirror size of 50 mm.

**Table B-1. Comparison of Beam Diameters at Different Locations**

Location	Beam Diameter (mm)
Lens ( $y_1$ )	61.721
SFPI entrance mirror ( $y_2$ )	76.521
SFPI center ( $y_3$ )	104.982
SFPI exit mirror ( $y_4$ )	133.442

Although this analysis provides a value for the minimum beam diameter, it is difficult to accurately translate this into an estimate of the percentage of the power that is coupled into the SFPI when considering light collected from an extended source. However, it provides the value of the lens focal length that will minimize the coupling losses. This can be used with one of the numerical ray-tracing programs to obtain the percentage of the power that is coupled into the SFPI with a specific lens that has aberrations.

## Analysis 2

This analysis attempts to increase the amount of light coupled into the SFPI by forming an image of the source that is constrained to be at the center of the SFPI. A schematic of the optical layout is shown in Figure B-12.

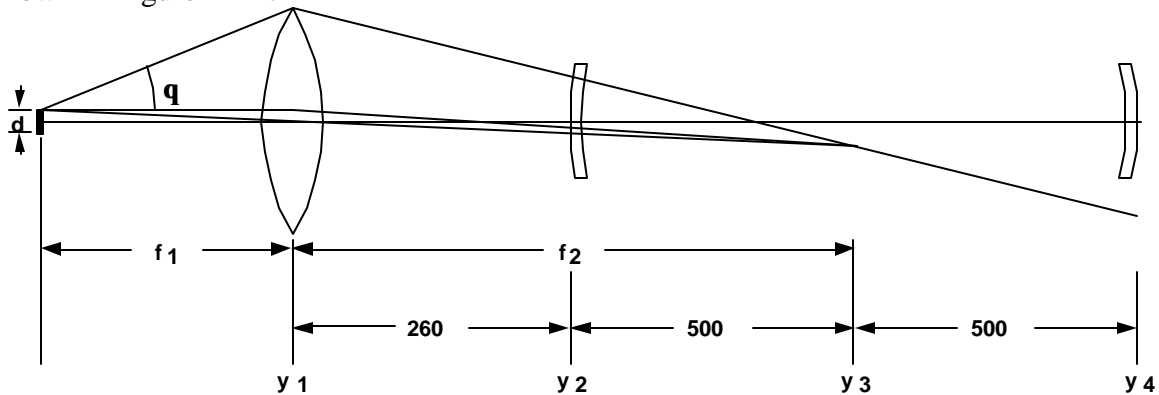


Figure B-12. Sketch of Optical Layout for Analysis of Coupling Losses when Using a Lens that Images the Source at the *Center* of the SFPI

Just as for analysis 1, the marginal ray is the one arising from the edge of the source and traveling at an angle,  $\theta$ , with the optical axis, where the following equation applies:

$$q = \sin^{-1}(NA) \cdot \quad (B-18)$$

The height of this marginal ray when it reaches the lens ( $y_1$ ) is given by the following equation:

$$y_1 = \frac{d}{2} + f_1 \tan(q) \cdot \quad (B-19)$$

The image of the source has a magnification,  $m$ . Therefore the height of the marginal ray when it reaches the center of the SFPI ( $y_3$ ) is given by the following:

$$y_3 = -\frac{m d}{2} \cdot \quad (B-20)$$

Since we are considering an ideal thin lens, the distance along the optical axis,  $x$ , is assumed to have its origin at the lens. Therefore, the equation for the height of the marginal ray as a function of the distance,  $x$ , along the optical axis is given by the following:

$$y = y_1 - \left( y_1 + \frac{m d}{2} \right) \frac{x}{f_2} \cdot \quad (B-21)$$

From the paraxial lens formula, we have the relationship shown in the following:

$$f_1 = \frac{f_2}{m}. \quad (\text{B-22})$$

Now substitute for  $f_1$  in Eq. (B-19) and  $y_1$  in Eq. (B-21) to obtain the following equation for the height of the marginal ray as a function of  $x$ :

$$y = \frac{d}{2} \left( 1 + \frac{2 f_2 \tan(\mathbf{q})}{dm} \right) - \frac{d}{2 f_2} \left( 1 + m + \frac{2 f_2 \tan(\mathbf{q})}{dm} \right) x. \quad (\text{B-23})$$

By substituting the value of  $x$  at the output mirror of the SFPI (i.e.,  $x=f_2+500$ ) into Eq. (B-23), we obtain an expression for  $y_4$  as a function of the magnification,  $m$ . The minimum of this expression as a function of  $m$  is found by setting the derivative equal to zero and solving for  $m$ . The minimum marginal ray height at the output mirror of the SFPI occurs when the value  $m$  has the value given by the following equation:

$$m = \sqrt{\frac{1000 f_2 \tan(\mathbf{q})}{d (f_2 + 500)}} = 3.5089, \quad (\text{B-24})$$

and this expression for  $m$  is substituted into Eq. (B-23) along with the value of  $x$  corresponding to the location of the output mirror, ( $f_2 + 500$ ).

This results in the following expression for the marginal ray height at the output mirror:

$$y_4 = -\left( \frac{250 d}{f_2} \right) - 2 \sqrt{\frac{250 d \tan(\mathbf{q})(f_2 + 500)}{f_2}}. \quad (\text{B-25})$$

The expression for the marginal ray height at the input mirror is obtained by substituting the value of  $x$  corresponding to the location of the input mirror ( $f_2 - 500$ ) into Eq. (B-23) along with the expression for  $m$  in Eq. (B-24).

The marginal ray height at the input mirror is given by the following:

$$y_2 = \left( \frac{250 d}{f_2} \right) + \left( \frac{1000}{f_2 + 500} \right) \sqrt{\frac{250 d \tan(\mathbf{q})(f_2 + 500)}{f_2}}. \quad (\text{B-26})$$

The value of  $y$  at the lens, which gives the lens radius, can similarly be obtained from Eq. (B-23) by setting  $x=0$  and substituting the expression for  $m$  given by Eq. (B-24). The following equation is obtained for the ray height at the lens:

$$y_1 = \frac{d}{2} \left( 1 + \sqrt{\frac{\tan(\mathbf{q}) f_2 (f_2 + 500)}{250 d}} \right). \quad (\text{B-27})$$

These equations can be evaluated as a function of  $f_2$  for various values of the parameters  $d$  and  $\theta$ . The results for  $d=10\text{mm}$  and for  $d=1\text{ mm}$  with  $\theta = \text{arcsine}(0.2)$  are shown in Figure B-13 a and b.

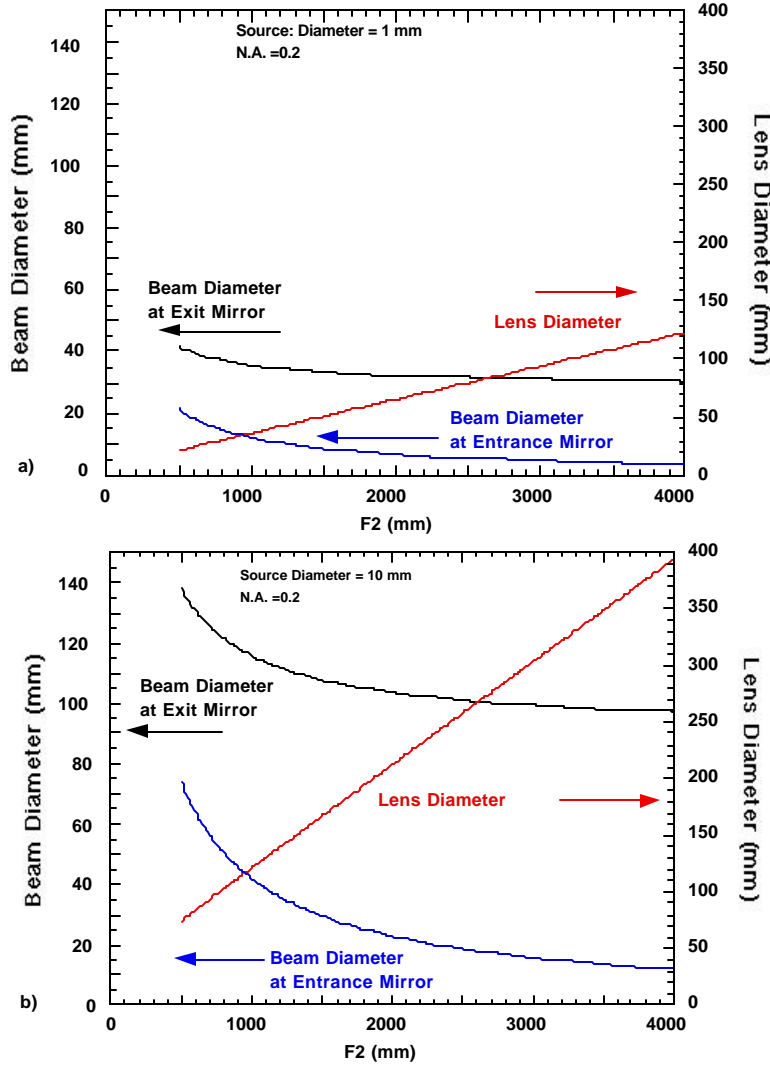


Figure B-13. a) Beam and Lens Diameter as a Function of the Distance between the Lens and the Center of the SFPI Cavity for a 1 mm Source with an NA of 0.2 ( $\theta = 11.537^\circ$ ).  
 b) Beam and Lens Diameter as a Function of the Distance between the Lens and the Center of the SFPI Cavity for a 10 mm Source with an NA of 0.2 ( $\theta = 11.537^\circ$ ). In Both cases, the Lens Focal Length is Selected to Image the Source at the Center of the SFPI with a Magnification that will Minimize the Beam Size at the Output Mirror of the SFPI.

These results show that the imaging technique can couple more light into the SFPI than the collimation technique. However, even with the imaging technique, it is not possible to couple all of the light into the SFPI if the source size is large. As can be seen, there is a significant difference in the lens diameter required for the two source sizes. Thus the output from a 1 mm diameter multimode optical fiber can be coupled into the SFPI with a 30 mm diameter, 800 mm focal length lens without any vignetting at the output mirror. Alternatively, the output from the coherent fiber bundle requires a 282 mm diameter, 2770 mm focal length lens to capture all of the light from the fiber and still results in significant vignetting at the output mirror since the beam diameter is 100 mm. As will be shown in the following section, even the light from a

small-diameter source will be vignetted when a real lens with aberrations is substituted for the paraxial lens.

### B2.2. An Optical Ray-Tracing Analysis

To obtain the actual performance of the system in the presence of optical aberrations, it is necessary to use numerical analysis and ray-tracing packages such as OptiCAD or ZEMAX. We have used these tools to determine the optimum performance that can be achieved by replacing the optical fiber bundle with a single large-core diameter optical fiber. A schematic for the model (Figure B-14) contains the beam splitter located at the entrance to the SFPI, as well as the optical fiber and a lens. The model for the SFPI employed for the initial screening of lenses used to couple light from the fiber to the SFPI contained an entrance window with zero optical power and an exit mirror. The version of ZEMAX being used, ZEMAX-XE, does not allow the reflectivity of the mirrors to be adjusted to any value other than 100%. The initial screening test for the lenses was to determine how much of the light could be transmitted through the entrance window and reflected from the exit mirror without vignetting. The system aperture was specified as an object space NA of 0.38, the field was set by the diameter of the fiber (1.5 mm), and the wavelength was 1.064  $\mu\text{m}$ .

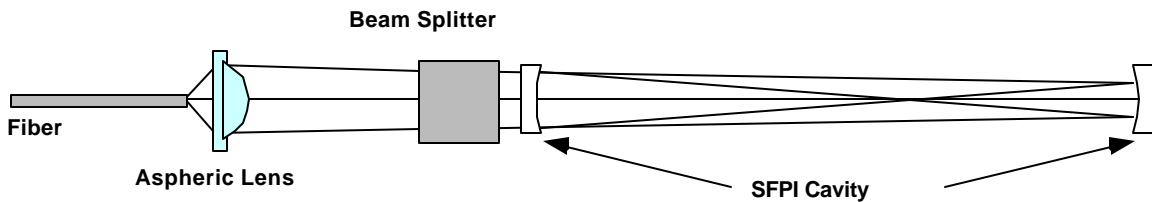


Figure B-14. Schematic Diagram of Model Used for Coupling between an Optical Fiber and the SFPI

As shown in Figure B-15, it is possible to couple nearly 100% of the light emanating from the 1.5 mm diameter fiber into the SFPI when using a paraxial lens to image the face of the fiber at the center of the SFPI. However, when a real lens is used, the amount of light that is coupled into the SFPI decreases significantly because of the aberrations associated with lenses that have a large enough NA to accept all of the light from the 0.38 NA fiber. Several lenses have been tested for collecting the light from the optical fiber and coupling it into the SFPI. These include an equi-convex lens (Coherent 43-1452), an air-spaced two-element condenser (Melles Griot 01 CMP 125) and an aspheric condenser (Melles Griot 01 LAG 019). The amount of light from the fiber that can be coupled into the SFPI without vignetting at either the entrance or exit mirror for each of these lenses is summarized in Table B-2.

**Table B-2 Efficiency of Light Coupling into the SFPI for Selected Lenses**

Lens	Diameter (mm)	Focal Length (mm)	Light Coupled into SFPI (%)
Coherent 43-1452	100	100	63.55
Melles Griot 01 CMP 125	100	100	71.85
Melles Griot 01 LAG 019	65	53	98.62

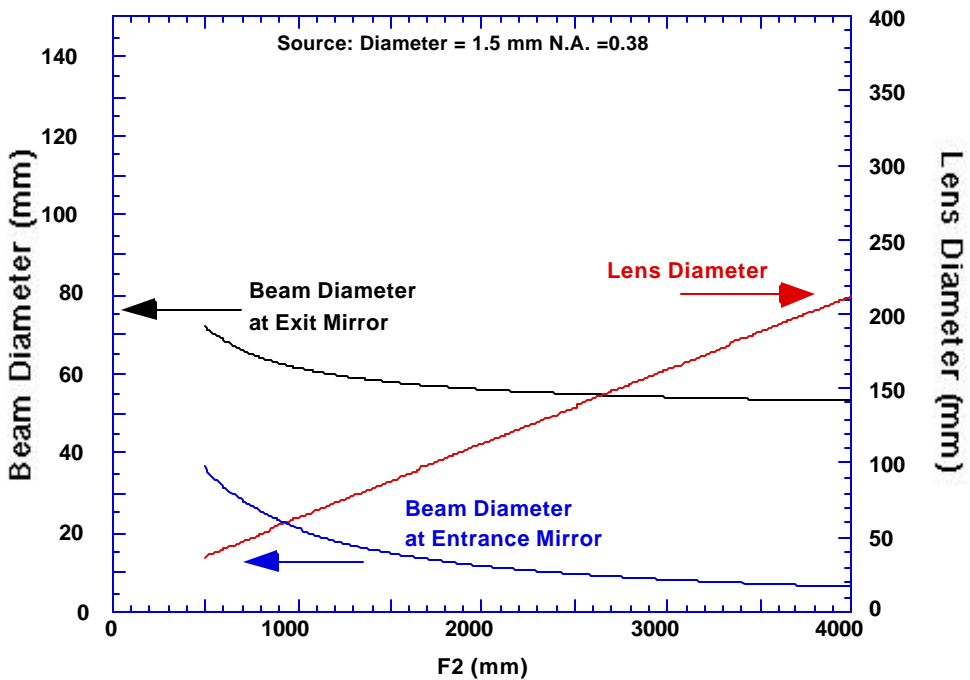


Figure B-15. Beam and Lens Diameter as a Function of the Distance between the Lens and the Center of the SFPI Cavity for a 1.5 mm Source with an NA of 0.38 ( $\theta = 22.33^\circ$ )

Since the performance of the aspheric condenser was significantly better than that of the others, it was selected for further studies of the coupling from the fiber to the SFPI. Since the version of ZEMAX that is being used does not support ray-tracing through nonsequential components, it is necessary to simulate the multiple bounces of the light through the SFPI with multiple mirrors in the model. These mirrors reflect the light back and forth over the length of the SFPI. The model used for these studies had 14 mirrors which effectively simulated light passing through the SFPI seven times. This is sufficient to allow an estimate of whether light is continuing to leak from the cavity or has reached a steady state. The results show that there is no significant loss of light during the first seven passes through the SFPI when using the aspheric condenser lens. This lens was selected for coupling the light from the fiber to the SFPI.

## Appendix C

### Analysis of the Cassegrain Obscuration Losses

The increasing sophistication of optical design and ray-tracing software packages allowed the simple analytical paraxial theory to be extended, thereby allowing for accurate and detailed modeling of the actual system design. For most of the ray-tracing analyses we have used OptiCAD, which is a geometric nonsequential optical ray-tracing system. OptiCAD allows the import of any 3D solid model via the STL file format thereby allowing for accurate and detailed modeling of an actual system design. Figure C-1 shows an accurate 3D model, imported into OptiCAD, which accurately represents the geometry of the Cassegrain optical collection system that was implemented in the laboratory. Both the spider that holds the secondary mirror in place and the optical fiber bundle are accurately modeled. This allows for the obscurations caused by the spider to be taken into account when performing the optical analysis, thereby extending the analyses beyond the simple analytical calculations performed previously. Furthermore, OptiCAD allows simulation of an optical fiber, thereby providing a method to establish the complete optical collection and transmission efficiency of the system through to the output of the optical fiber.

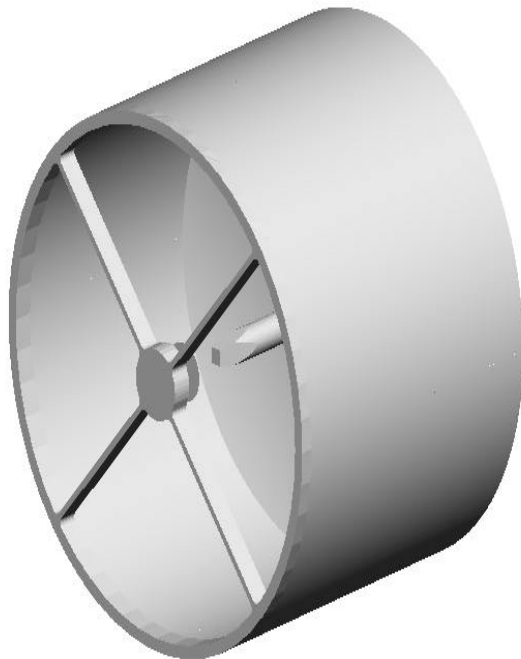


Figure C-1. 3D Model Imported into OptiCAD for the Analysis of the Cassegrain Optical Collection System

Initial work involved comparison of obscuration results obtained by performing an optical ray-trace in OptiCAD with analytical models, so that the accuracy of the ray-tracing method could be verified. As shown in Figure C-2, rays originate from a light source and propagate along the z-axis to interact with the Cassegrain optical collection system. The beam diameter and maximum solid angle into which the rays radiate is defined by the étendue of the interferometer system.

Based upon the calculations of Hercher [11], it can be shown that for a 1 m length SFPI having a mirror reflectivity of either 81% or 93% and an incident laser wavelength of 1064 nm, the maximum étendue is  $1.4192 \text{ mm}^2.\text{sr}$  or  $0.4856 \text{ mm}^2.\text{sr}$ , respectively (see Appendix A). Thus for a maximum full-divergence angle of the source of  $8.7^\circ$  spot sizes of 10 mm and 5.85 mm diameter, respectively, are required. As a ray propagates through the system, the ray energy is reduced by surface and volumetric absorption. In the model of the Cassegrain system (Figure C-2), rays are absorbed when they are incident on all surfaces except for the primary and secondary mirrors. A detector element, having the same spatial extent as the input aperture of the optical fiber bundle, is located at the entry plane to the optical fiber bundle which allows rays reaching the input aperture of the optical fiber bundle to be recorded. Thus by launching a known number of rays from the optical source, the obscuration of the system can be determined by recording the number of rays incident on the detector and obtaining the ratio of received ray energy to launched ray energy. Figure C-3 shows a comparison of analytical paraxial theory and optical ray-trace model obscuration calculations for cases of vignetting by the secondary mirror alone, and vignetting by the spider assembly which holds the secondary mirror in place. An obscuration of 1.0 means that no rays reached the detector. This is caused at near-range by the secondary mirror or spider assembly completely blocking the rays radiating from the source. While in reality the obscuration of the spider is the dominating obscuration in the system, ray-tracing of the obscuration caused by the secondary mirror alone was included since it permitted comparison with an analytical model and thereby provided a technique for verifying the ray trace data. As can be seen from Figure C-3, the point source analytical paraxial theory is in excellent agreement with the point source optical ray-trace model. The optical ray-tracing capability then allowed the analysis to be extended to a source having a finite spatial extent. Again, from Figure C-3 it can be seen that the point and extended source optical ray-trace models are in excellent agreement except for the near-range configuration.

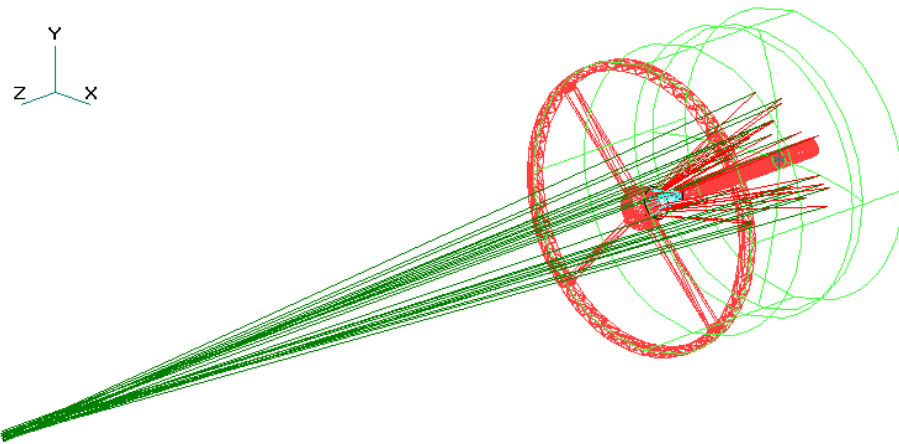


Figure C-2. Wire Frame Display of the Optical Configuration Used to Analyze the Obscurations in the Cassegrain Optical Collection System. The Source Shown is Modeled as an Extended Source Having a 10 mm Diameter and 25 rays are Shown Diverging from the Source with a Maximum Full-Divergence Angle of  $8.7^\circ$ . Obscuration Calculations are Performed with the Source Located at Different Locations along the z-axis. The Source is Shown at z=38 inches in this Model.

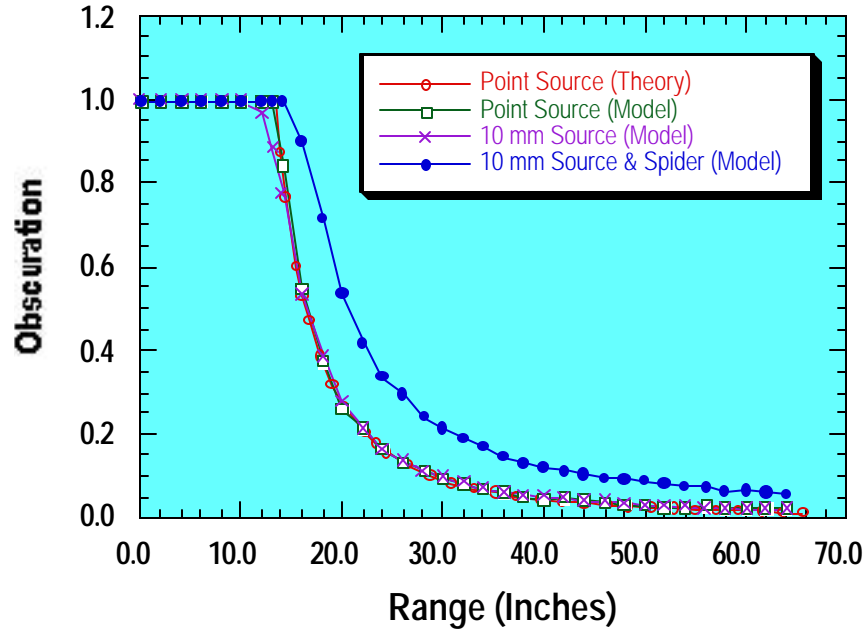


Figure C-3. Comparison of Analytical Paraxial Theory and Optical Ray-Trace Model Obscuration Calculations for Cases of Vignetting by the Secondary Mirror Alone, and Vignetting by the Spider Assembly Which Holds the Secondary Mirror in Place. For each Ray-Traced Case, the Source Radiated 10,000 Rays into a Maximum Full-Divergence Angle of  $8.7^\circ$ .

Figure C-4 extends the optical ray-trace model calculations presented in Figure C-3 and shows the full Cassegrain system obscuration which takes into account obscuration caused by the spider and, in addition, overfilling of the optical fiber bundle. It can be seen from Figure C-4 that the point and extended source ray-trace models produce very similar results. The optimum operational range, where the obscuration is at a minimum, when using a flat secondary mirror is calculated to be from  $\sim 36$  to  $\sim 50$  inches for a 10 mm diameter extended source or  $\sim 34$  to  $\sim 50$  inches for a point source. These results are in very good agreement with the original design specification of 33 to 48 inches, which was calculated assuming a point source analytical model.

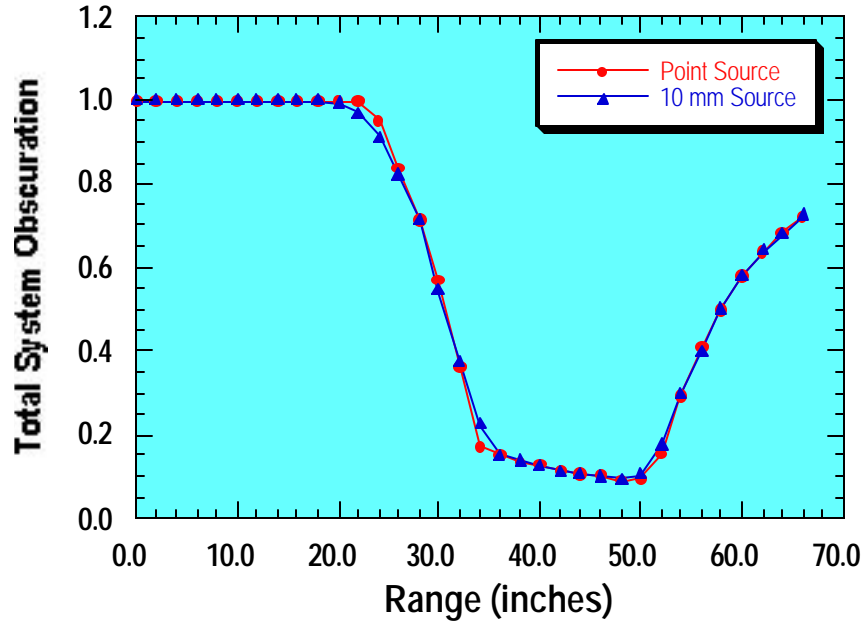


Figure C-4. Calculations for the Full Cassegrain System Obscuration Which Takes Into Account Obscuration Caused by the Spider and Overfilling of the Optical Fiber Bundle. For the Optical Ray-Trace, the Source Radiated 10,000 Rays into a Maximum Full-Divergence Angle of  $8.7^\circ$ .

The final step for completion of the OptiCAD Cassegrain system model was to implement a source having a Gaussian distribution to simulate the reflected probe laser beam. Custom sources, such as the Gaussian source, are integrated into the OptiCAD environment via a dynamic link library (DLL). We obtained the source code for the Gaussian source DLL from the vendor of OptiCAD and modified and recompiled the code to remove an unwanted dependency between spot size and beam divergence. In the new Gaussian source model each ray emitted from the Gaussian source has a full intensity value of 1.0. The Gaussian spatial profile is realized by the summation of many rays over the region of the emitting source, with the central region, corresponding to the beam waist, being the most heavily populated. Figure C-5 shows the spatial profile for a Gaussian source of 5 mm extent having a beam waist of 2.5 mm. Figure C-6 shows the spatial profile for a disk source which radiates a Lambertian distribution from any point on the surface. Both intensity distributions resulted from the summation of  $10^6$  rays emanating from the source and incident on the detector plane.

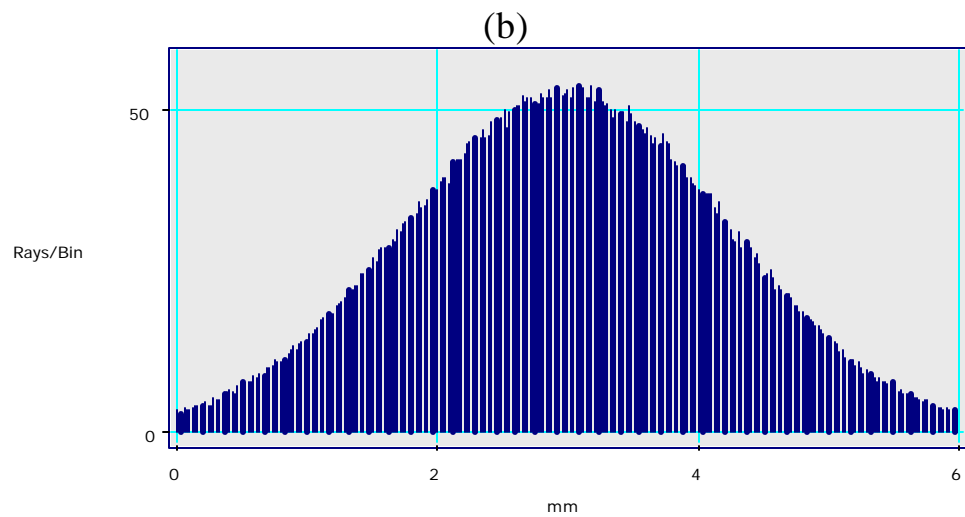
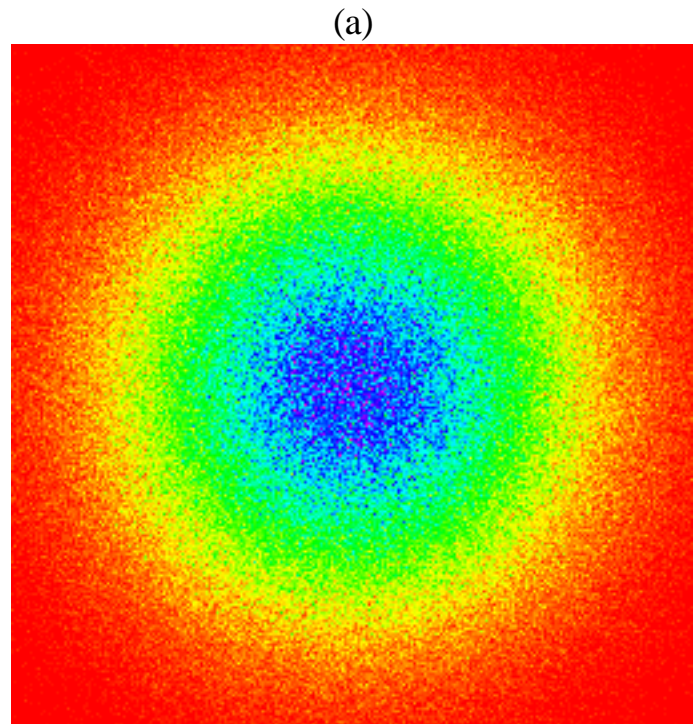


Figure C-5. Spatial Beam Profile Resulting from the Summation of  $10^6$  rays Traced from a Gaussian Source of 5 mm Extent having a Beam Waist of 2.5 mm and Received at the Detector. (a) 2D Intensity Distribution, (b) 1D Intensity Profile with Symmetry about the Center of the Beam.

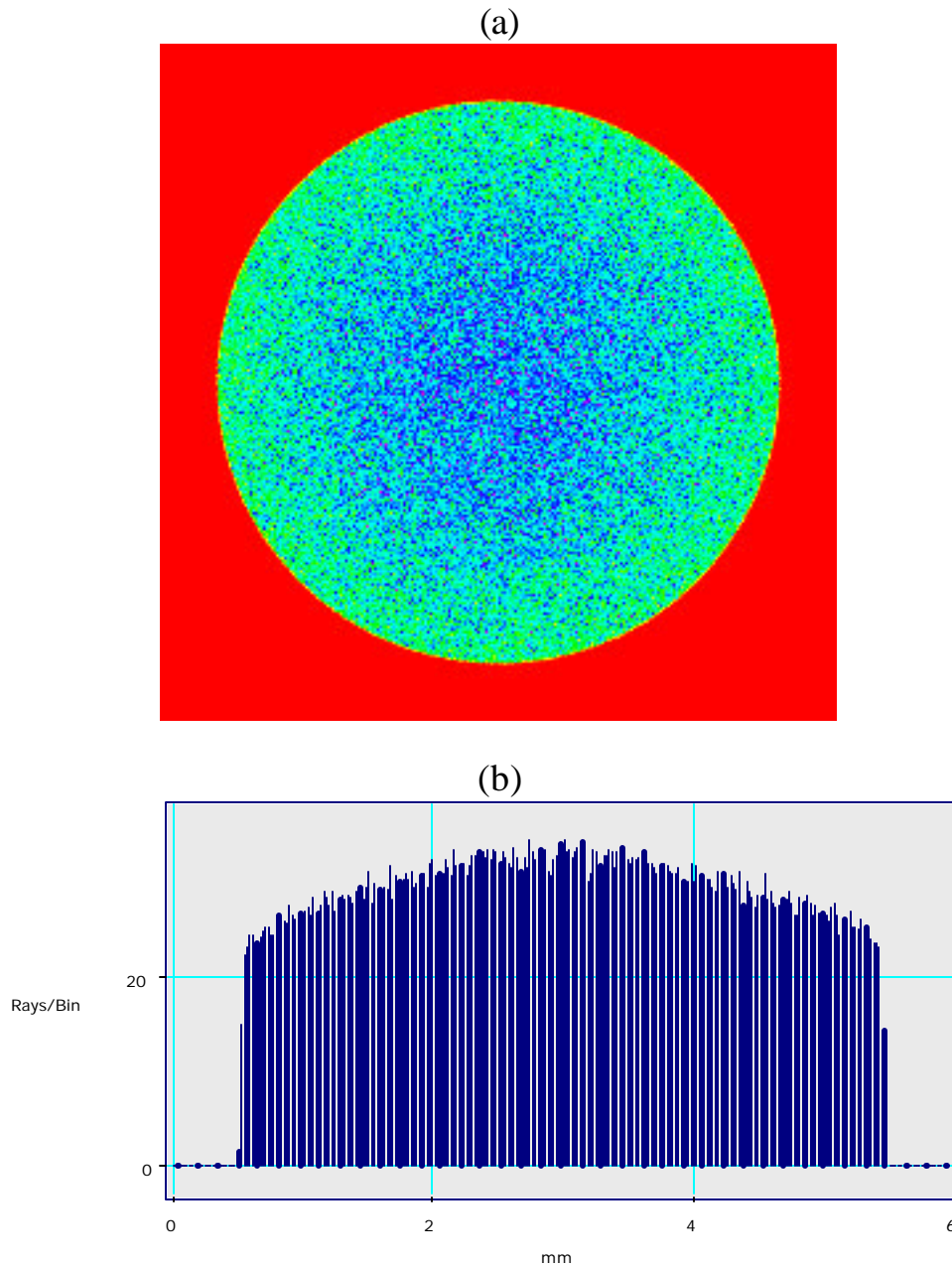


Figure C-6. Spatial Beam Profile Resulting from the Summation of  $10^6$  rays Traced from a 5 mm Diameter Lambertian Disk Source and Received at the Detector. (a) 2D Intensity Distribution, (b) 1D Intensity Profile with symmetry about the Center of the Beam.

Figure C-7 again shows calculations for the full Cassegrain system obscuration analysis (near-range configuration) which take into account obscuration caused by the spider and overfilling of the optical fiber bundle. However, this time a comparison is made of the results when a correction to the spot size is not made based on the criteria presented in Table 1. It can be seen from Figure C-7 that the results for the 93% reflectivity mirrors at a probe laser spot size of 10 mm do not produce satisfactory results, with obscurations exceeding 25% for all ranges.

However, adjusting the full-divergence angle and thereby reducing the probe laser spot size to 5.85 mm, the results are almost identical to those from the original design. These results show the importance of reducing the probe laser spot diameter from  $\sim$ 10 mm to  $\sim$ 5.85 mm to minimize the obscuration for the current SFPI operational configuration. This required optimization of the optical elements being used in the Cassegrain subassembly which is used to transmit the laser beams from the output of the optical fibers to the target.

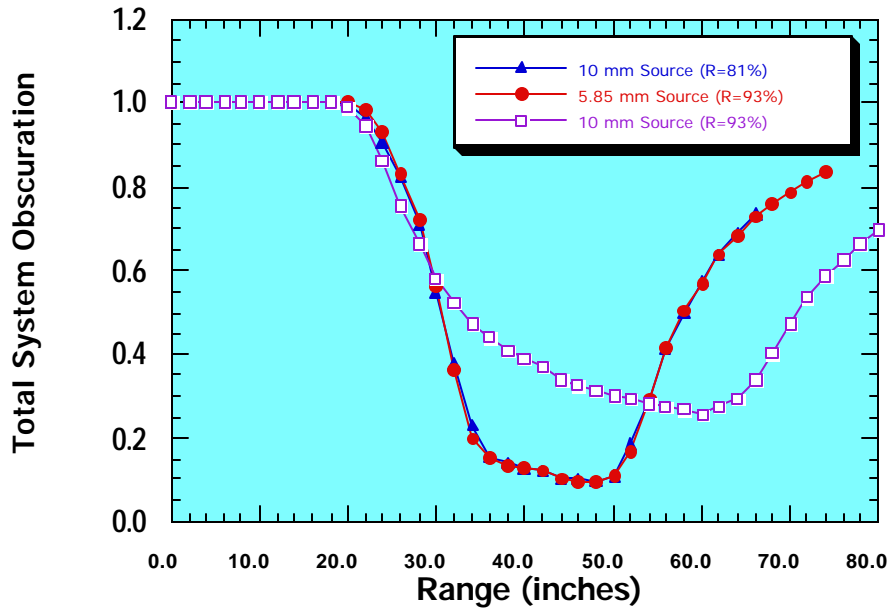


Figure C-7. Calculations for the Full Cassegrain System Obscuration Which Take into Account Obscuration Caused by the Spider and Overfilling of the Optical Fiber Bundle. Several Parameter Sets, Described Below, were Analyzed and the Results Plotted.

- (a) 10 mm source (R=81%) corresponds to the obscuration calculated for a 1 m length SFPI having a mirror reflectivity of 81% and an incident laser wavelength of 1064 nm with a maximum étendue is  $1.419 \text{ mm}^2.\text{sr}$ . The maximum full-divergence angle is  $8.7^\circ$ .
- (b) 5.85 mm source (R=93%) corresponds to the obscuration calculated for a 1 m length SFPI having a mirror reflectivity of 93% and an incident laser wavelength of 1064 nm with a maximum étendue is  $0.4856 \text{ mm}^2.\text{sr}$ . The maximum full-divergence angle is  $8.7^\circ$ .
- (c) 10 mm source (R=93%) corresponds to the obscuration calculated for a 1 m length SFPI having a mirror reflectivity of 93% and an incident laser wavelength of 1064 nm with a maximum étendue is  $0.4856 \text{ mm}^2.\text{sr}$ . The maximum full-divergence angle is  $5.1^\circ$ .

For each parameter set analyzed, the source radiated 10,000 rays into the maximum full-divergence angle.

Figure C-8 again shows calculations for the full Cassegrain system obscuration analysis (near-range configuration) which take into account obscuration caused by the secondary mirror/spider assembly and overfilling of the optical fiber bundle. However, this time both Lambertian and Gaussian spatial source distributions were modeled using 10,000 rays that radiated from the source into a maximum full-divergence angle of  $8.7^\circ$  and were compared with the analytical

model for a 7 mm diameter fiber (Figure C-8). The results are similar for both analytical and optical ray-trace models. The main difference was slightly increased loss associated with the ray-trace models, which would be expected since the obscuration caused by the spider assembly was accounted for. The maximum loss of light at each extreme of the near-range configuration was about 10% to 20%, which was consistent with experimental measurements and was within acceptable limits for this type of system. Small differences are also evident in the Gaussian and Lambertian optical ray-trace models, but these typically occur outside of the operational range for the system.

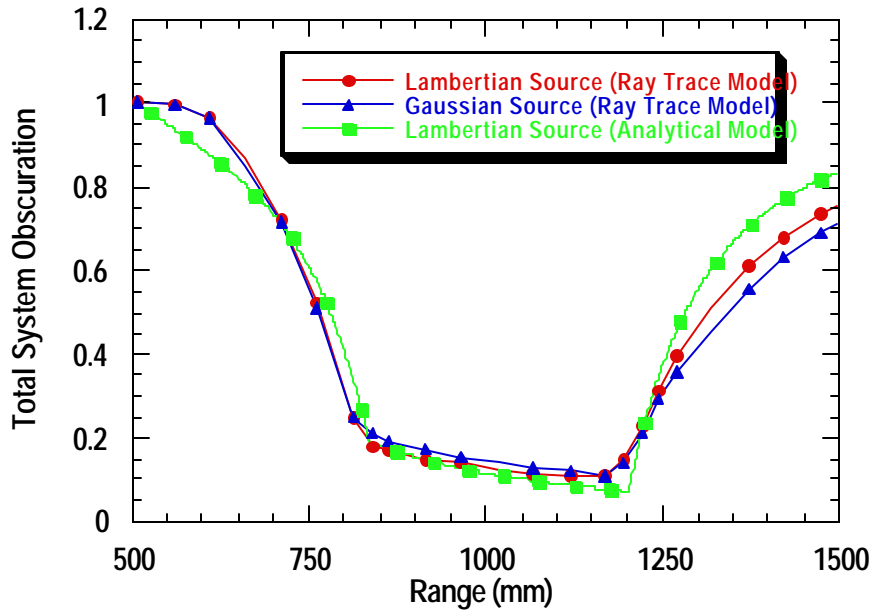


Figure C-8. Optical Ray-Trace Calculations of the Loss of Light from a 5.85 mm Diameter Probe Laser Spot Scattered from the Target. Light Loss Results from Obscuration Caused by the Secondary Mirror and Spider Assembly and from Overfilling of a 7 mm Diameter Optical Fiber.

## Appendix D

### D1. Analysis of Light Coupling from a Delivery Optical Fiber to the Target

The input sources for the Cassegrain optical beam delivery subassembly are the two optical fibers transmitting the light from the generating laser and the probe laser. The subassembly relay optics must combine the two light beams so that they are collinear with each other and also collinear with the axis of the Cassegrain optics. In addition, the subassembly is required to focus the two beams onto the target with the desired spot size and a minimal loss of light. Since in the current design the subassembly must fit beneath the Cassegrain housing, the space requirements must be minimized. To gain insight into the system design considerations, it is helpful to initially use a paraxial design procedure for specifying the lens and fiber diameter that should be used in the relay optics. However, to obtain specific performance data, such as the effect of lens aberrations, the efficiency with which the light is transmitted to the target, and the spot size of the beams at the target, an exact ray-tracing analysis must be used. The analysis presented below shows that when coupling the generation and probe laser from a fiber to the target, it is advantageous to have a small fiber diameter and NA to obtain a small spot size at the target with reasonably sized relay optics. Although the latter is possible with the probe laser, the typical generating laser power densities dictate fibers with core diameters of 1000  $\mu\text{m}$  or greater. These conflicting requirements result in design trade-offs to select a fiber diameter and NA that will maintain optimal transmission and minimize the target spot size while avoiding damage to the delivery optical fiber.

#### D1.1. A Paraxial Analysis

Initial design parameters for the Cassegrain system dictated an overall étendue that matched that of the SFPI. For the current system configuration, this implies that the rays from the target have a maximum full-divergence angle of 8.7° and the spot size has a diameter of 5.85 mm for optimum collection efficiency. To satisfy the minimal space requirements, a 25.4 mm diameter beam combiner was selected. This imposes a limiting aperture of ~18 mm when the beam combiner is oriented at 45°. If the light from the optical fibers could be collimated with the required 5.85 mm diameter, this would ensure optimized delivery of the generation and probe laser beams to the target without vignetting within the Cassegrain optical beam delivery subassembly. Also, for the inspection of contoured geometries, the generation and probe laser spot sizes would not vary as the depth of the contoured part changed. Unfortunately, however, as shown in the analysis presented below, the practical implementation of a collimated beam from a large-core multimode optical fiber is restricted by a fixed relationship between the diameter of the source and its NA which controls the beam divergence. The alternative to using a collimation technique is to use a lens to image the face of the fiber onto the target. Both collimation and imaging techniques will be described.

##### D1.1.1. Collimating Method

This method places the fiber face in the object plane of the lens so that the on-axis light is collimated by the lens and propagates to the target without diverging (neglecting diffraction). Assume that there is an extended object, such as an optical fiber, with a diameter,  $d$ , which is

radiating light uniformly over its aperture and has a numerical aperture of  $NA_f$ . When this light is collimated with a lens (Figure D-1), the light emanating from a point,  $O$ , on the optical axis is collimated into a beam with a diameter  $D_c$  that has zero divergence (in the absence of diffraction) and propagates parallel to the optical axis of the lens. The light emanating from a point on the periphery of the object,  $O_p$ , is also collimated into a beam with the same diameter and having no divergence, but propagating at an angle,  $\mathbf{q}_f$ , with respect to the optical axis of the lens. Further, a ray from  $O_p$  that is parallel to the optical axis will pass through the focal point of the lens on the output side. If the lens used to collimate the light has a focal length,  $f$ , and the object has a diameter,  $d$ , the following relationship is obtained between  $f$ ,  $d$ , and  $\mathbf{q}$ :

$$f = \left( \frac{d}{2 \tan(\mathbf{q})} \right). \quad (D-1)$$

The angle  $\mathbf{q}$  is thus the minimum divergence half-angle of the collimated beam that contains all of the light radiated from the object.

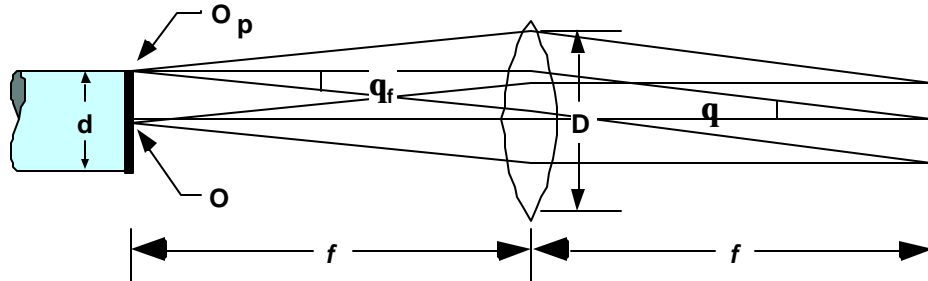


Figure D-1. Sketch of Optical Rays Relevant to Determining the Minimum Divergence Angle,  $\mathbf{q}$ , of a Collimated Beam from an Optical Fiber with a Diameter,  $d$ , and an  $NA_f = \sin \mathbf{q}$

The focal length of the lens is related to the diameter of the collimated beam and the NA of the fiber through the following relation:

$$f = \left( \frac{D_c}{2 \tan(\mathbf{q}_f)} \right), \quad (D-2)$$

where the NA of the fiber is  $\sin \mathbf{q}$ .

When Eq. (D-1) and Eq. (D-2) are combined, we obtain the following expression for the minimum divergence angle,  $\mathbf{q}$  :

$$\tan(\mathbf{q}) = \left( \frac{d}{D_c} \right) \tan(\mathbf{q}_f). \quad (D-3)$$

Therefore, to reduce the minimum divergence angle for a desired collimated beam size, either the diameter of the optical fiber or its NA must be reduced. The focal length of the lens is not relevant to the minimum divergence angle, but, along with the NA of the object, does determine

the beam diameter. Thus, for a beam delivery fiber having a 600  $\mu\text{m}$  diameter core with an NA of 0.39, from Eq. (D-3), it can be seen that using a single lens to obtain a beam diameter of 5.85 mm results in a beam divergence half-angle of  $\sim 2.5$  degrees. Clearly the beam is not collimated and will have a spot size at the target much greater than 5.85 mm.

The parameters used in the above calculations are somewhat arbitrary. It is of interest to determine the combination of lens focal length and diameter, and fiber diameter and NA that will produce the minimum spot size at the target. This can be done by deriving an expression for the spot size in terms of the lens and fiber parameters. The marginal ray at the target will be the one with its origin on the periphery of the fiber that is directed towards the optical axis at an angle,  $\mathbf{q}$  (Figure D-1). In general, the height of the marginal ray after it has passed through the lens is given by Eq. (D-4):

$$y = \frac{d}{2} - f \tan \mathbf{q}_f - z \tan \mathbf{q}, \quad (\text{D-4})$$

where  $d$  = fiber core diameter,  $\sin \mathbf{q}$  = NA of fiber,  $f$  is the lens focal length, and  $z$  is distance from lens along optical axis.

Also the diameter of the beam at the lens,  $D$ , is given by the following relationship:

$$D = d + 2 f \tan \mathbf{q}_f. \quad (\text{D-5})$$

Substituting for  $f$ , we obtain the following:

$$D = d + \frac{d \tan \mathbf{q}_f}{\tan \mathbf{q}}. \quad (\text{D-6})$$

Rearranging Eq. (D-7), we obtain the following expression for  $\tan \mathbf{q}$

$$\tan \mathbf{q} = \frac{\tan \mathbf{q}_f}{\left( \frac{D}{d} - 1 \right)}. \quad (\text{D-7})$$

Now use Eqs. (D-1) and (D-7) to substitute for  $f$  and  $\tan \mathbf{q}$  in Eq. (D-4) to obtain the following:

$$y = \frac{d}{2} - \frac{d}{2} \left( \frac{D}{d} - 1 \right) - z \frac{\tan \mathbf{q}_f}{\left( \frac{D}{d} - 1 \right)}. \quad (\text{D-8})$$

The spot size at the target is designated,  $S$ , and is related to the value of  $y$  at the target,  $y_t$ , by the expression:

$$S = -2 y_t, \quad (\text{D-9})$$

where the minus sign is used to force  $S$  to be positive since it is noted that  $y$  will have a negative value at the target if it is positive at the fiber face. It is convenient to write the minimum lens diameter in terms of the spot size as follows:

$$D = \mathbf{a}S, \quad (\text{D-10})$$

where  $\mathbf{a}$  is always less than unity. Substituting Eqs. (D-8) and (D-10) into Eq. (D-9), we obtain the following:

$$S = -d + d \left( \frac{\mathbf{a}S}{d} - 1 \right) + 2z_t \frac{\tan \mathbf{q}_f}{\left( \frac{\mathbf{a}S}{d} - 1 \right)}, \quad (\text{D-11})$$

where  $z_t$  is the distance to the target.

This can be rewritten as the following quadratic equation in  $S$ :

$$S^2 - \frac{(1-3\mathbf{a})d}{\mathbf{a}(1-\mathbf{a})} S - \frac{2d(d+z_t \tan \mathbf{q}_f)}{\mathbf{a}(1-\mathbf{a})} = 0. \quad (\text{D-12})$$

The solution to Eq. (D-12) is as follows:

$$S = \frac{(1-3\mathbf{a})d}{2\mathbf{a}(1-\mathbf{a})} \left[ 1 \pm \sqrt{1 + \frac{8\mathbf{a}(1-\mathbf{a})(d+z_t \tan \mathbf{q}_f)}{(1-3\mathbf{a})^2 d}} \right]. \quad (\text{D-13})$$

The denominator functions are zero when  $\mathbf{a}$  is 1/3 and 1. The value of  $S$  remains finite at each of these values of  $\mathbf{a}$ . If  $\mathbf{a} = 1/3$ , we obtain the following:

$$S = 3\sqrt{d(d+z_t \tan \mathbf{q}_f)}. \quad (\text{D-14})$$

If  $\mathbf{a} = 1$ , we obtain the following:

$$S = d + z_t \tan \mathbf{q}_f. \quad (\text{D-15})$$

The results of the spot size analysis are best summarized graphically. The variation of  $S$  with  $\mathbf{a}$  (Figure D-2) for fiber diameters ranging from 0.1 mm to 1.5 mm, a fiber NA of 0.12 and  $z_t = 1.175\text{m}$  shows that the minimum spot size occurs for  $\mathbf{a} \sim 0.5$  and the value of the minimum increases as the fiber diameter increases. The variation for two different fiber NAs, each having a fiber diameter of 0.1 mm, is shown in Figure D-3. The minimum spot size for the 0.1 mm fiber is 10.56 mm and occurs for  $\mathbf{a} \sim 0.515$ . Note that even for this small fiber diameter, the spot size is significantly larger than the desired size of 5.85 mm.

The variation of the lens diameter and focal length versus  $\mathbf{a}$  are summarized in Figures D-4 and D-5. The relationship between the beam diameter at the lens,  $D$ , and the spot size at the target,  $S$ , given by Eq. D-10, is used to obtain the relationship between  $D$  and  $\mathbf{a}$ .

$$D = \frac{(1-3\mathbf{a})d}{2(1-\mathbf{a})} \left[ 1 \pm \sqrt{1 + \frac{8\mathbf{a}(1-\mathbf{a})(d+z_t \tan \mathbf{q}_f)}{(1-3\mathbf{a})^2 d}} \right]. \quad (\text{D-16})$$

This expression is plotted in Figure D-4 for several fiber diameters ranging from 0.1 mm to 1.5 mm. The beam diameter at the lens corresponding to the minimum spot size when  $a \sim 0.515$  is  $\sim 5.44$  mm.

The focal length of the lens is given in terms of  $a$  by the following equation:

$$f = \frac{1}{2} \left( \frac{D - d}{\tan q_f} \right) = \frac{1}{2} \left( \frac{a S - d}{\tan q_f} \right). \quad (\text{D-17})$$

The relationship between  $f$  and  $a$  for several fiber diameters is shown in Figure D-5. Note that the required focal length increases as the fiber diameter increases. The focal length of the lens corresponding to the minimum spot size when  $a \sim 0.515$  is  $\sim 22.08$  mm.

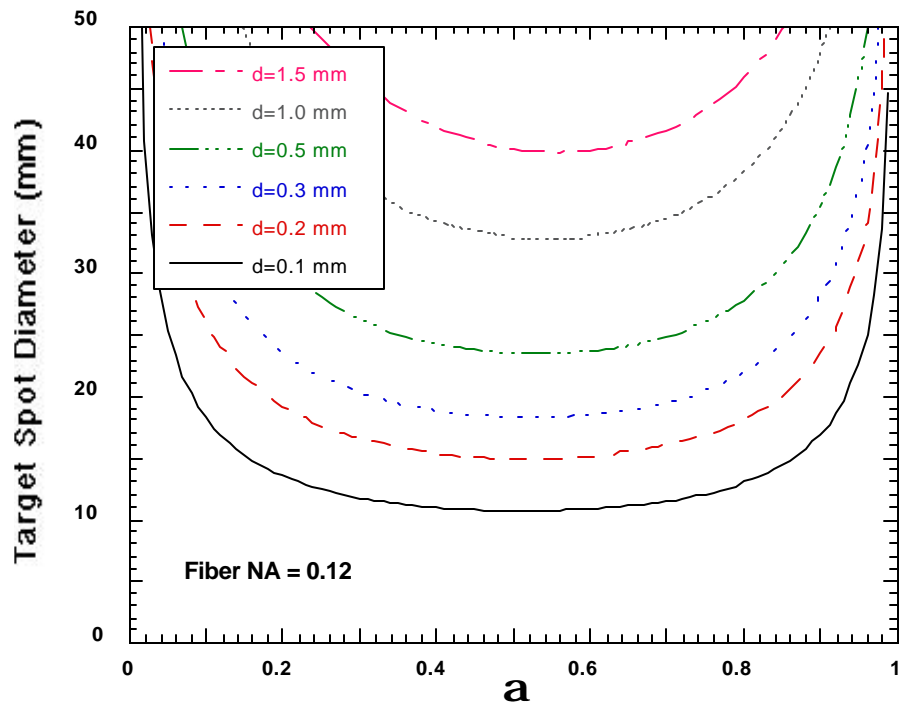


Figure D-2. Variation of Diameter of Target Spot ( $S$ ) as a Function of  $a$  for a 0.12 NA Fiber with Diameters Ranging from 0.1 mm to 1.5 mm

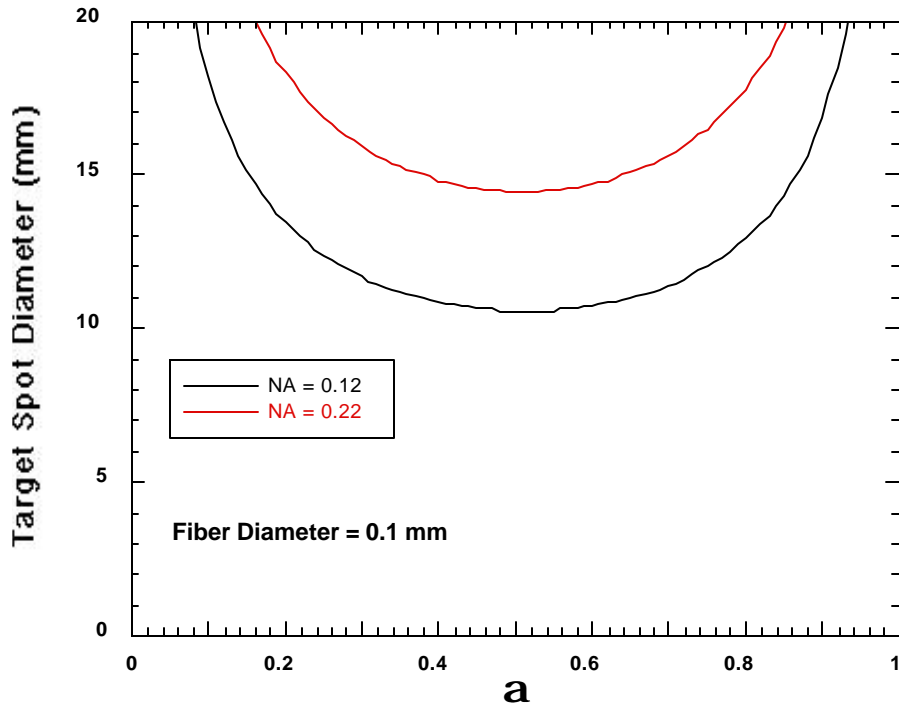


Figure D-3. Variation of Diameter of Target Spot (S) as a Function of  $a$  for a 0.1 mm Diameter Fiber with NAs of 0.12 and 0.22

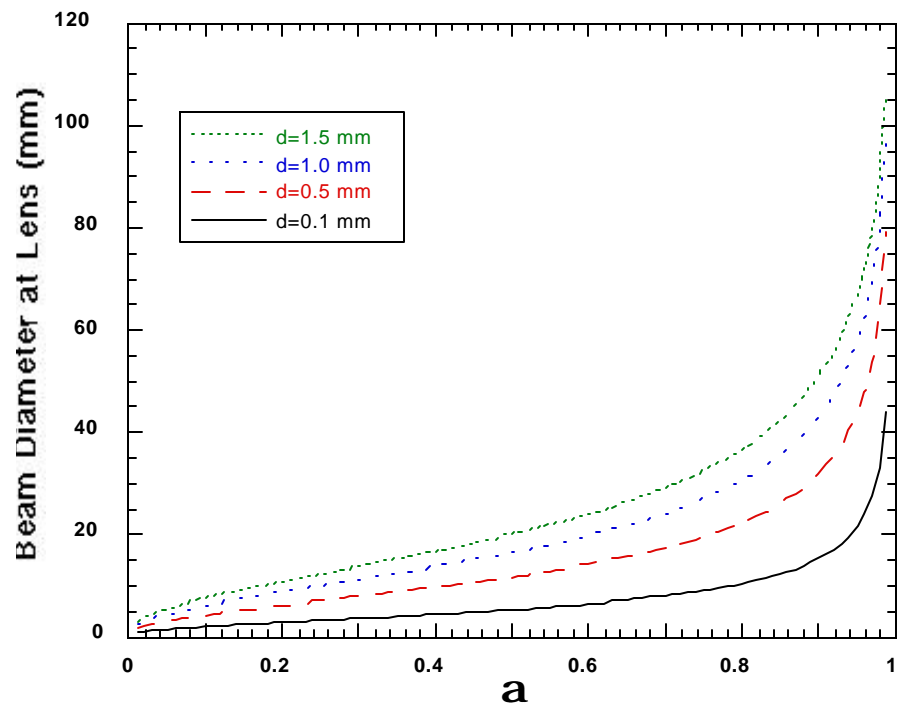


Figure D-4. Variation of Beam Diameter at Lens, D, as a Function of  $a$  for Fiber Diameters Ranging from 0.1 to 1.5 mm

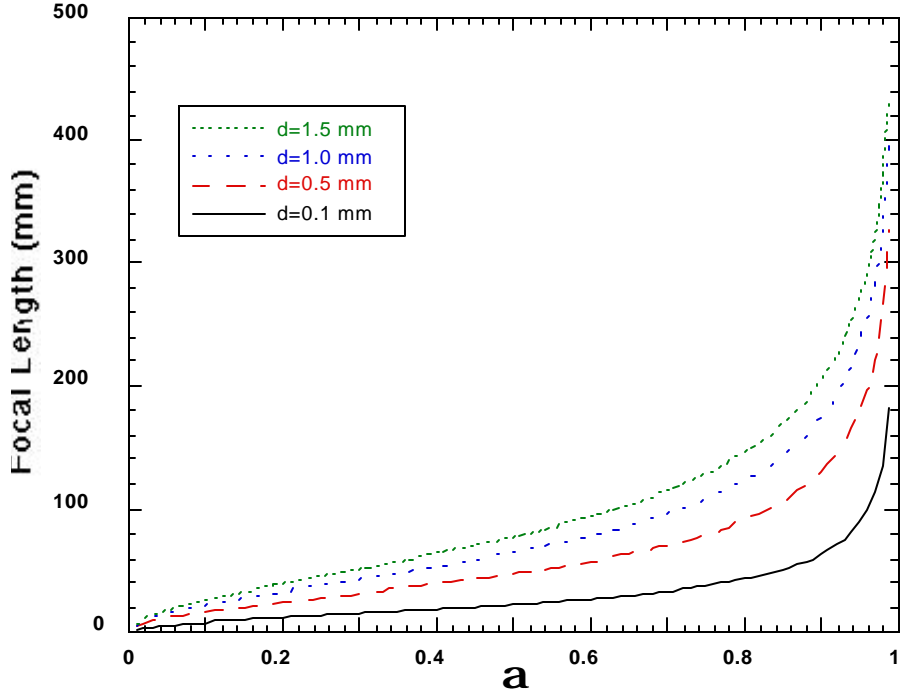


Figure D-5. Variation of Lens Focal Length,  $f$ , as a Function of  $a$  for Fiber Diameters Ranging from 0.1 to 1.5 mm

### D1.1.2. Imaging Method

This method images the fiber face onto the target. The lens is designed with a magnification that produces the desired spot size at the target. If  $m$  is the desired magnification, then the relationship between the lens focal length,  $f$ , and the object-to-lens distance,  $f_1$ , is given by the following equation:

$$f = \left( \frac{m}{m + 1} \right) f_1, \quad (\text{D-12})$$

where

$$m = \frac{f_2}{f_1} = \frac{S}{d}, \quad (\text{D-13})$$

and  $f_2$  is the lens to target distance,  $S$  is the target spot diameter, and  $d$  is the fiber diameter.

The beam diameter at the lens will be given by the following:

$$D = d + 2 f \tan q_f, \quad (\text{D-14})$$

where the NA of the fiber is  $\sin q_f$ . The desired target spot diameter is  $\sim 5.85$  mm and the target distance  $f_2$  is 1175 mm. Using Eqs. D-12, D-13, and D-14, we obtain the following expressions for the focal length of the lens and the beam diameter at the lens:

$$f = \frac{f_2}{\frac{S}{d} + 1} \quad (D-15)$$

$$D = d \left( 1 + \frac{2 f_2}{S} \tan q_f \right). \quad (D-16)$$

The beam diameter at the lens versus the fiber diameter for  $S = 6$ , and  $f_2 = 1175$  is shown in Figure D-6, and the focal length versus the fiber diameter is shown in Figure D-7. The required focal length for a 0.1 mm diameter fiber with an NA=0.12 is 19.26 mm, and the beam diameter at the lens is 4.83 mm. The lens-to-fiber distance is 19.58 mm. These parameters are compatible with coupling of the probe laser. However, increasing the fiber diameter to 1.0 mm for the generating laser increases the focal length to ~168 mm, and the beam diameter at the lens is 48.34 mm. The lens-to-fiber distance is increased to 195.83 mm. Unfortunately, changing the optical components to accommodate these dimensions for delivery of the generation laser conflicts with the minimal space design requirements of the current implementation and a design trade-off is needed.

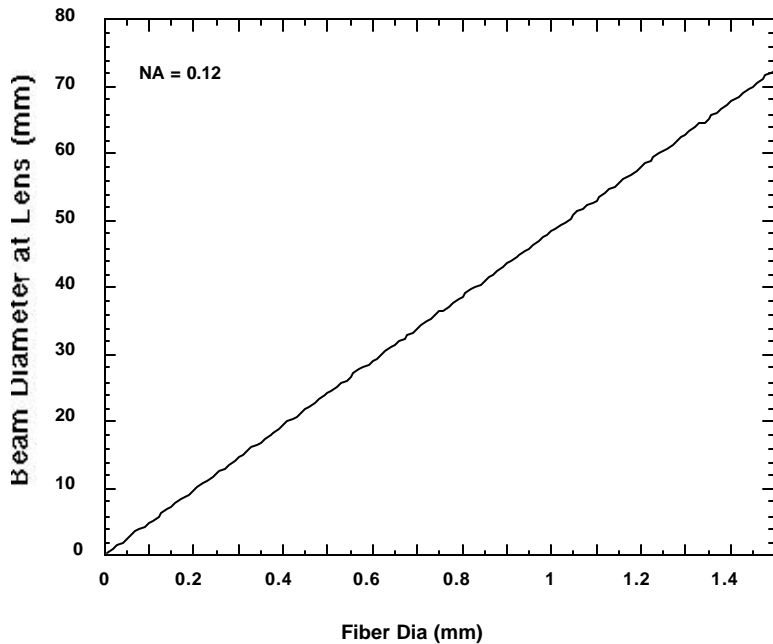


Figure D-6. Beam Diameter at Lens Versus Fiber Diameter for a 0.12 NA Fiber and a 6 mm Target Spot Diameter

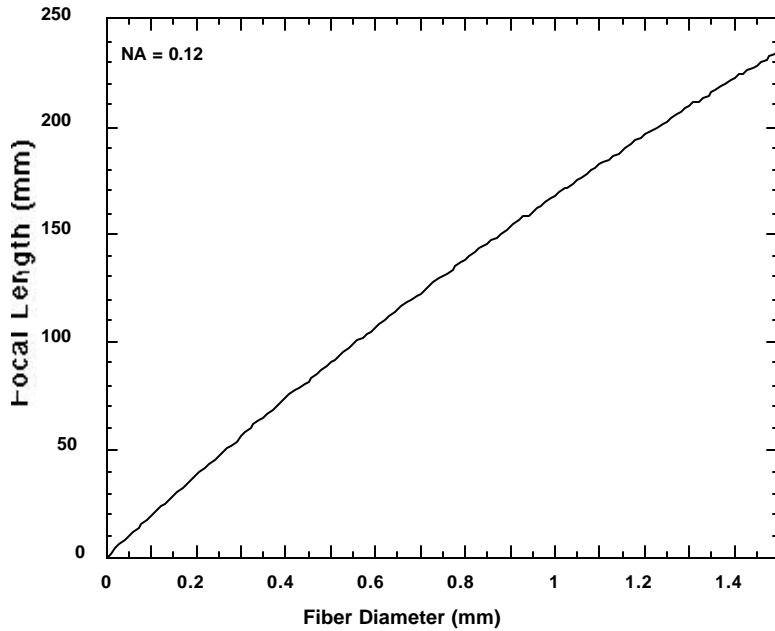


Figure D-7. Focal Length of Lens Versus Fiber Diameter for a 0.12 NA Fiber and a 6 mm Target Spot Diameter

#### D1.1.3. Summary of Paraxial Analysis

Using the collimating method, we determined that even for small fiber diameters ( $100 \mu\text{m}$ ), the spot size is significantly larger than the desired size of  $5.85 \text{ mm}$  and we found that it is best to image the delivery fiber face onto the target unless the fibers have core diameters  $\ll 0.1 \text{ mm}$ . When imaging the fiber face, the core diameter and NA of the fiber significantly affect the diameter of the lenses required to relay the light from the fiber to the target as well as the spot size at the target. These results show that a small fiber diameter and NA are required to obtain a small spot size at the target with reasonably sized relay optics. Since the probe laser has relatively low peak-power densities, a small fiber core diameter can be used, making this a suitable solution. However, the high peak-power densities of the generating laser require fibers with core diameters of  $1000 \mu\text{m}$  or greater. This results in larger lens diameters that cannot be readily accommodated in the relay optics subassembly. These conflicting requirements require a design trade-off between the fiber diameter and the maximum apertures of the beam splitter, focusing lens and turning mirrors that comprise the relay optics. To best optimize the design, it is necessary to model the complete system using a numerical ray-tracing analysis package such as OptiCAD or ZEMAX.

#### D1.2. Ray-Tracing Analysis of the Cassegrain Subassembly Relay Optics

The objective of the numerical ray-tracing is to determine a design that will achieve the desired spot size at the target while minimizing the power loss due to vignetting. Using the optical design program, ZEMAX, a model of the LACIS-R generation laser relay optics was prepared. The model contains the components shown in Figure D-8. The light that is emitted from the optical fiber, passes through a lens to the first turning mirror (mirror 1) to the second turning mirror (mirror 2) and then to the target. Mirror 1 is elliptical with major and minor axes of  $31.5 \text{ mm}$  and  $22.4 \text{ mm}$ . The second mirror is circular with a diameter of  $18 \text{ mm}$ . The optical fiber is

0.91 mm in diameter with an NA of 0.22. The lens used to image the fiber face onto the target is a Newport KPX094 plano-convex lens with a diameter of 25.4 mm and a nominal focal length of 100 mm. The model allows the face of the 0.91 mm diameter fiber to be imaged onto the target at a range of 1028.7 mm from the Cassegrain primary mirror. When the lens is adjusted to produce the minimum spot size on the target, which is ~8.8 mm, the transmitted energy is only ~14.6% of the energy emitted from the fiber. This is slightly less than the energy that was experimentally transmitted through this system, which was ~20%. The likely causes of the difference between the two results are a slightly larger spot size at the target during the experiments and a nonuniform distribution of light across the output face of the fiber. Neither of these parameters was precisely measured experimentally but could result in an increase in the transmitted energy.

The model allows a systematic investigation of the energy loss at each element in the current system for different spot sizes on the target. It also allows simulation of improvements that can be realized by changing various parameters within the system, such as the diameter and NA of the optical fiber, the diameters of the two mirrors, and the location of the lens to a position between the two mirrors. This capability was used to investigate changes that could be made to improve the power transmission efficiency.

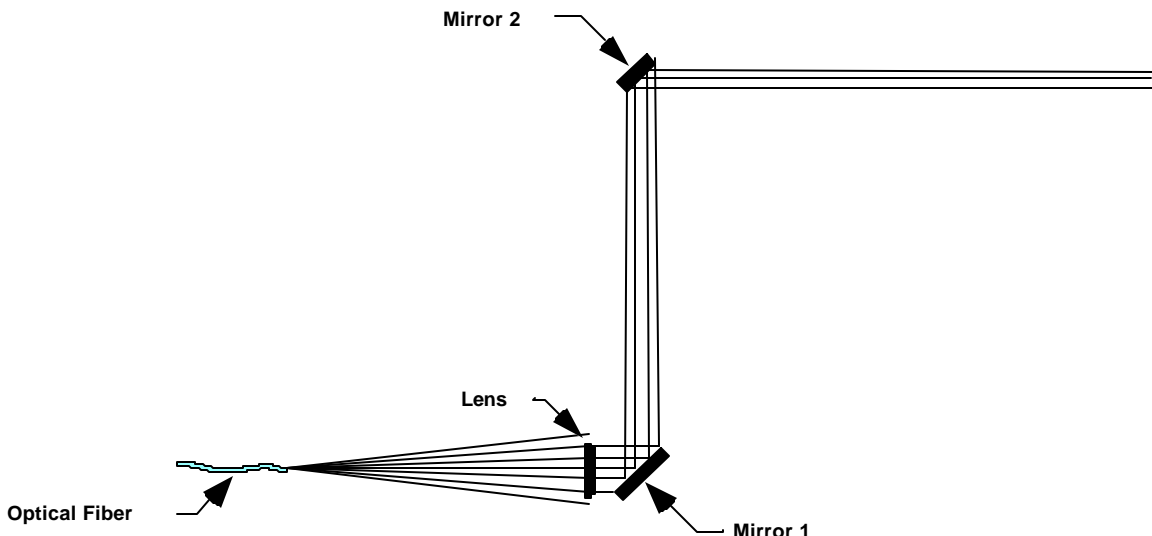


Figure D-8. Schematic of LACIS-R Relay Optics Configuration Used to Transmit Generation Beam from Optical Fiber

Investigation of where the beam was being vignetted found that significant improvement in the power transmission efficiency could be obtained by changing the model so that the lens is placed between the two turning mirrors. This allows a slightly larger lens to be used if needed and reduces the vignetting at mirror 1. This model is shown in Figure D-9. In addition, the beamsplitter that is used to combine the generation and probe laser beams was added to the model to evaluate vignetting at this surface and decentering of the beam. Based on the paraxial analysis and on investigations using the LACIS-R model, the diameter of the optical fiber that is

to be used to deliver the Q-switched Nd:YAG generation laser to the Cassegrain subassembly was increased to 1.0 mm and its NA was decreased to 0.12.

Still using the Newport KPX-094 lens, the improved design decreases the spot size at the target to 8 mm and increases the transmission efficiency to 46.6%. With the improved design, the first folding mirror transmits about 86% of the energy, which implies that ~40% of the energy is vignetted at the second folding mirror. A measure of the size of the spot at the target is obtained by calculating the fraction of energy encircled versus the radius from the center of the spot (Figure D-10). About 90% of the energy is contained within a diameter of 8 mm.

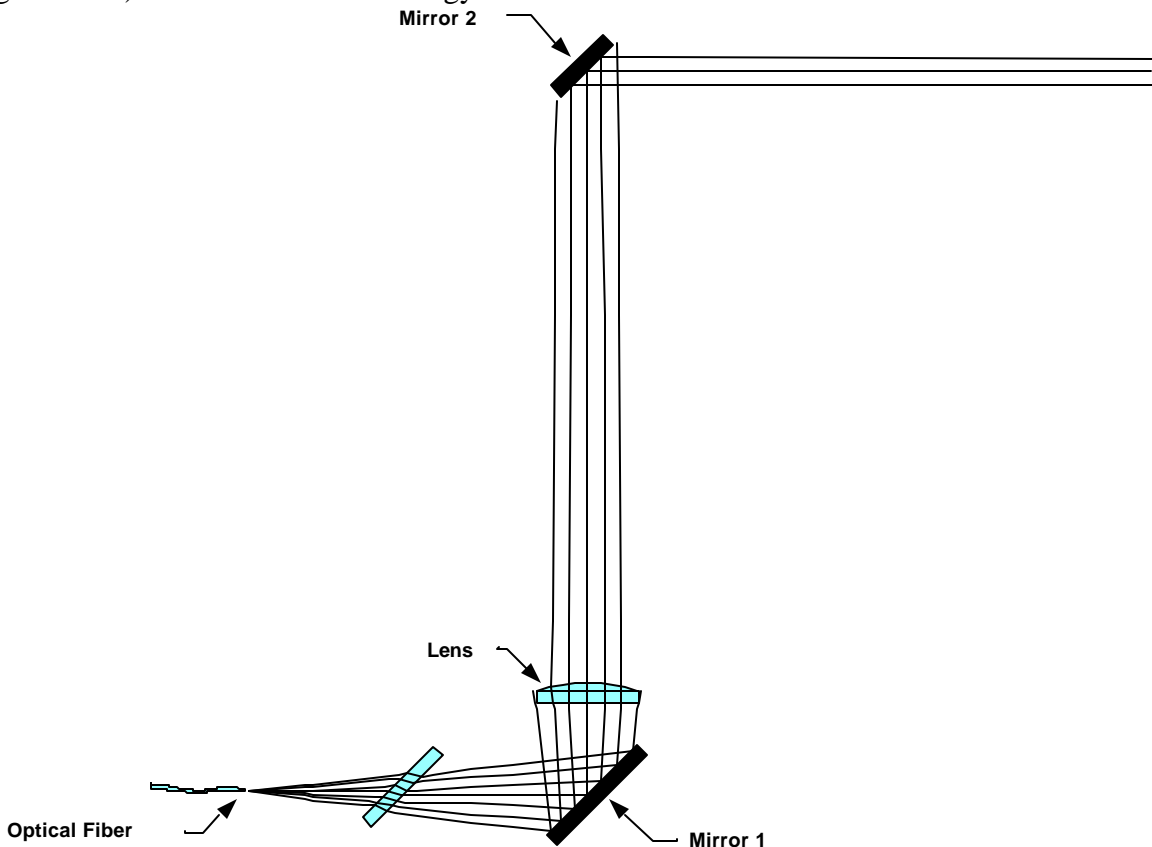


Figure D-9. Schematic of the Improved Relay Optics Configuration Used to Transmit the Generation Beam from Optical Fiber to Target

As the model evolved, it became necessary to develop macros using the ZEMAX Programming Language (ZPL) to adjust the various parameters of the system, such as the spacing between components and decentering of the folding mirrors to optimize the energy throughput of the system. Use of the macros allows the optimization to be done more rapidly and accurately than a trial and error manual technique. It has been possible to develop a design procedure for optimizing the relay optics used with the Cassegrain scanner that produces reliable results after two iterations. The chief design criteria are to maximize the transmission efficiency for a given lens and to have the output beam be coaxial with the axis of the Cassegrain scanner. The steps used are itemized below.

1. Select lens that will provide desired magnification with the lens-to-target distance set to the required value. A paraxial analysis is used for this.
2. Vary the distance between the optical fiber and the lens to place the minimum blur circle at the target. This can be done with default merit function available in the optical design program, ZEMAX.
3. Adjust the decenter of the beamsplitter to maximize the transmitted optical power. This is done using a custom macro developed using ZPL, designated OPTIMUM\_DECENTER.
4. Adjust the decenter of the first folding mirror to maximize the transmitted optical power. This also uses the OPTIMUM\_DECENTER macro used in step 3.
5. Adjust the decenter of the lens to make the chief ray parallel to the axis of the Cassegrain scanner when it is incident on the target. This requires use of a different custom ZPL macro, designated COAX.
6. Adjust the decenter of the second folding mirror to maximize the transmitted optical power using the OPTIMUM\_DECENTER macro used in step 3.
7. Measure the percentage of the power from the optical fiber that is transmitted to the target and the RMS spot size at the target.
8. Refocus the system using the procedure given in step 2.
9. Again measure the percentage of the power from the optical fiber that is transmitted to the target and the RMS spot size at the target. Note the difference between these values and those obtained in step 7. If this difference is significant, iterate design steps 3 through 8.

This procedure has been used with three different lenses including the one used with the LACIS-R optics. The results of these calculations are summarized in Table D-1.

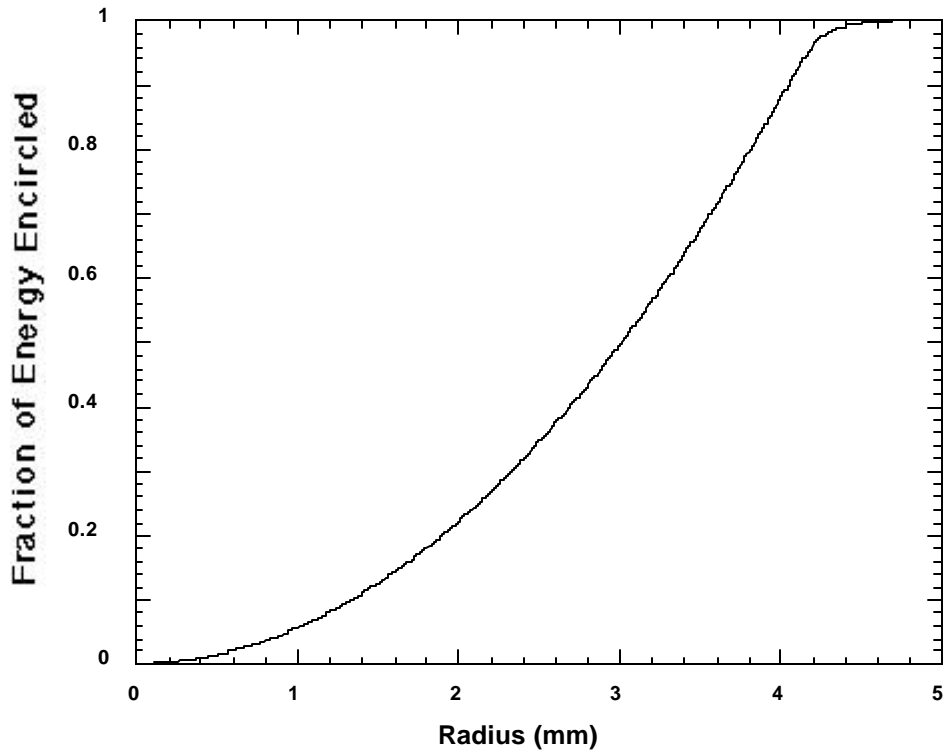


Figure D-10. Fraction of Energy in Laser Spot at Target as a Function of the Radius from Center

**Table D-1 Optical Transmission Efficiency of Relay Optics With Selected Lenses**

Lens Model	Diameter (mm)	Focal Length (mm)	Power Transmitted (%)	RMS Spot Size (mm)
Newport KPX-094	25.4	100	46.6	8
Melles Griot LAO-139	30	140	20.5	6
Melles Griot LAO-189	30	200	8.7	4

## Appendix E

### Cross-Calibration of the SFPI with a Stabilized Michelson Interferometer

For many rudimentary investigations, such as ultrasonic generation efficiency measurements of different material types using different lasers, it is often useful to present data in absolute form so that previous and future investigations may be easily compared and other researchers may make direct comparisons under perhaps different operating configurations. We have been pursuing two methods for obtaining absolute data from the SFPI. The first approach which has been implemented is to use a stabilized Michelson interferometer to cross-calibrate the SFPI. The second method which is under investigation under separate Rockwell Science Center funding is a more direct approach which integrates a calibrated phase modulator into the SFPI system.

The sensitivity of the Michelson interferometer to small displacements is well known and given by the following equation:

$$\frac{dV_{out}}{dx} = \frac{2PV_{p-p}}{\lambda}, \quad (E-1)$$

where  $\delta V_{out}$  is the measured signal voltage in the linear operating regime,  $\delta x$  is the sample displacement,  $V_{p-p}$  is the peak-peak voltage corresponding to the modulation depth caused by a full fringe shift (i.e., a phase difference of greater than  $\pi$  radians or displacement of  $>\lambda/2$ ), and  $\lambda$  is the incident laser wavelength. Thus, in practice an acquired signal waveform can be calibrated in terms of absolute displacement by applying the following transformation:

$$dx = \frac{I dV_{out}}{2PV_{p-p}}. \quad (E-2)$$

To realize the cross calibration of the SFPI using the stabilized Michelson interferometer, a reliable and stable amplitude source of ultrasonic waves is required. To this end, a piezoelectric calibration cell was constructed which uses a 5 MHz longitudinal wave contact transducer affixed to the rear surface of a 0.375 inch thick polished aluminum mirror. The calibration cell is designed so that the transducer is under compression, thereby maintaining good interfacial contact with the aluminum mirror. This design has been shown to be very rugged and allows the calibration cell to be moved between optical setups without any detrimental changes in performance. During testing the 5 MHz calibration transducer was operated in pulse-echo mode, which provided a self-calibration signal that was monitored to verify that the integrity of the interfacial contact was maintained during the cross calibration procedures. The calibration cell also provides a 5 mm diameter input aperture for optical alignment purposes so that the same central region of the aluminum mirror is probed by either the Michelson interferometer system, which employs an argon-ion probe laser, or the 1 m SFPI system, which employs a long-pulse Nd:YAG probe laser.

To complete the cross calibration procedure, the signal acquired with the SFPI needs to be converted to displacement. The SFPI is frequently referred to as a velocity sensor, which would mean that in the time domain its output is the derivative of the input, and in the frequency domain its output is  $j\omega$  times the input. Although this is precisely true at dc, it is not accurate for signals in the center portion of the SFPI passband. Therefore a simple integration of the acquired signal will not yield the desired displacement information. To obtain an accurate estimate of the true displacement signal that was detected with the SFPI, it is necessary to perform a deconvolution operation on the received signal using the correct complex frequency response of the SFPI. The deconvolution operation will thus reverse the signal modifications produced by the SFPI and allow an accurate estimate of the ultrasonic wave displacement. The calculated theoretical magnitude and phase response of the SFPI that will be used to perform the deconvolution is shown in Figure E-1. The results of the deconvolution operation will have an unknown scaling factor that will depend on the response function. However, since the displacement amplitude generated by the calibration cell was fixed, the peak-to-peak amplitude of the deconvolved calibration signal will be scaled accordingly.

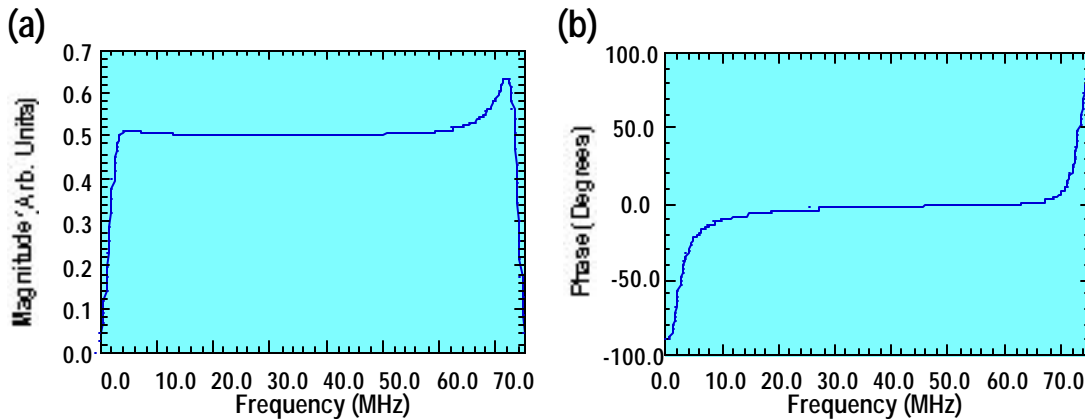


Figure E-1. (a) Theoretical Magnitude and (b) Phase Response of the 1 m SFPI Operating in Reflection Mode with Mirror Reflectivities of 93%

Thus, at low frequencies, the SFPI is a velocity sensor and so its output signal  $s(t)$  will be proportional to the surface velocity ( $v$ ), which can be integrated to obtain the surface displacement ( $\mathbf{dx}$ ), as the following shows:

$$d\mathbf{x} = \dot{\mathbf{v}} v dt \quad . \quad (\text{E-3})$$

However, at higher frequencies, the signals are closer to the center portion of the SFPI passband, making it possible to obtain the displacement by simply multiplying the SFPI output signal by a constant,  $k$ , as in the following equation:

$$d\mathbf{x} = ks(t) \quad . \quad (\text{E-4})$$

The cross calibration procedure requires that a signal from the piezoelectric calibration cell be detected with the Michelson interferometer and the SFPI. The signals from the SFPI will be deconvolved to obtain waveforms that are proportional to displacement. The results of the deconvolution operation will have an unknown scaling factor that is determined by using the calibration cell to generate a known signal and comparing the output of the Michelson interferometer with the deconvolved SFPI output signal. Once this scaling factor is known, any output signal from the SFPI can be converted to the equivalent surface displacement. Figure E-2 shows a comparison of the amplitudes of ultrasonic signals detected with the 1 m SFPI and Michelson interferometer systems when using the calibration cell as the ultrasonic source. The waveform acquired with the Michelson interferometer (Figure E-2b) is displayed in units of absolute displacement (nm) by applying the calibration transformation given in Eq. (E-2) with  $\lambda=514.5$  nm and  $V_{p-p}=1.3$  V. The peak-peak displacement is 7.9 nm. The peak-peak voltage of the SFPI signal (Figure E-2a) is 647.3 mV, which, therefore, is also equivalent to 7.9 nm. The linear calibration coefficient is thus 0.012 nm/mV.

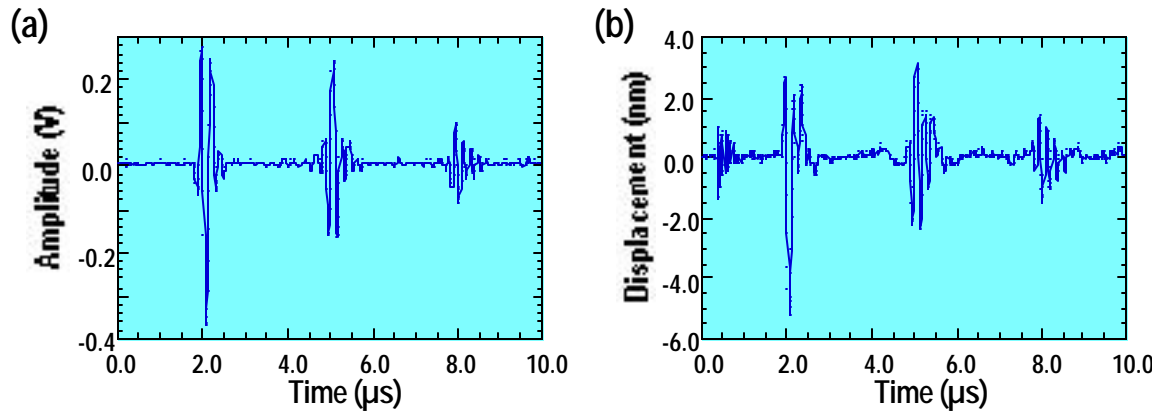


Figure E-2. Ultrasonic Waveforms Generated by the PZT Calibration Cell and Detected by (a) the 1 m SFPI, and (b) the Stabilized Michelson Interferometer

Each of the output signals, obtained during the thermoelastic generation study of polymer-matrix composites, was converted to a surface displacement signal using the deconvolution technique. The peak-to-peak amplitude of each of these signals was then plotted versus the peak-to-peak amplitude of the SFPI output signals (Figure E-3). Normalization corrections were applied to the data to account for different incident generation laser pulse energies, and small differences in sample thickness were corrected by applying an attenuation correction. It is assumed that any frequency dispersion of the ultrasonic attenuation in the materials was negligible over the system bandwidth and that the thermal damage threshold of the material was not exceeded. Although the frequency content of the signals produced by the different lasers are slightly different, it is assumed that the frequency content of the signals from any one of the lasers will be the same for all of the materials tested. Since deconvolution is a linear operation, the signals generated by any one of the lasers will lie on a straight line for all of the materials. The straight lines for the different lasers may have slightly different slopes because the frequency content of the signals is slightly different.

For comparison, the output signals from the thermoelastic generation study were also transformed by using the integral relationship (Eq. (E-3)) and the scaling constant (Eq. (E-4)). Figure E-4 shows a plot of the pseudo-displacement signals obtained by integrating the SFPI signals versus the peak-to-peak amplitude of the SFPI output signals.

The relative values of the pseudo-displacement signals obtained using the integral relationship have significant differences from the values obtained using deconvolution. In particular, for the alexandrite laser (755 nm), the difference in the displacement ranges from -10% to -25%. The minimum errors are obtained for the CO<sub>2</sub> laser (10.6 μm), which range from 0 to 15%. The results for the scaling constant are closer to those obtained with the deconvolution. The maximum errors, observed for the Nd:YAG laser operating at 532 nm, range from -4% to +5%. The minimum errors are again obtained for the CO<sub>2</sub> laser, which range from -4% to 0%. This demonstrates the importance of using the deconvolution method to accurately obtain the absolute displacement from the SFPI output data.

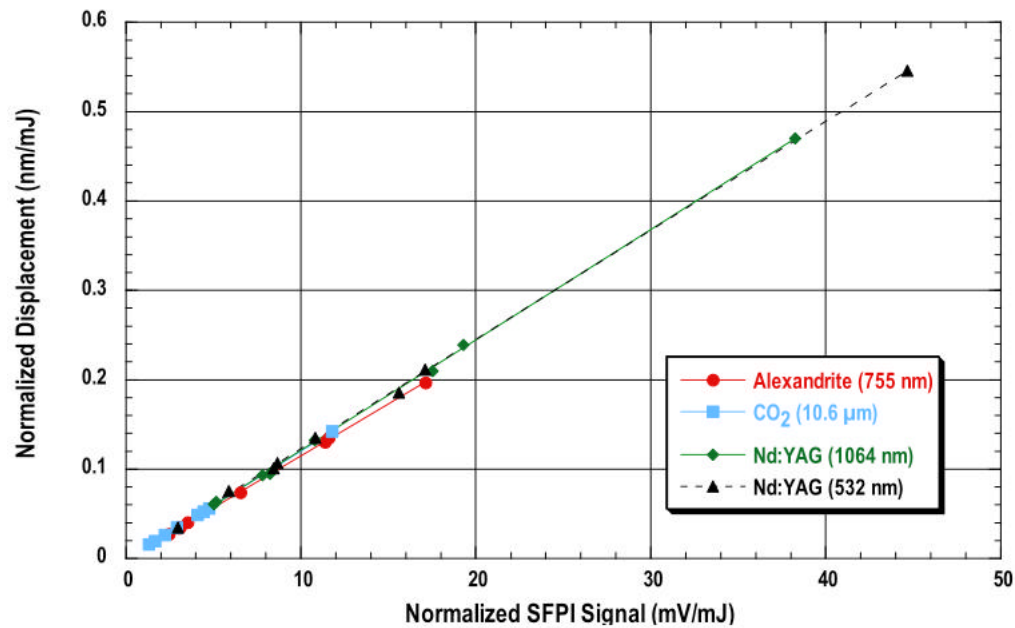


Figure E-3. Plot of the Deconvolved SFPI Signal Amplitude (i.e., Displacement) as a Function of the Raw SFPI Signal Amplitude

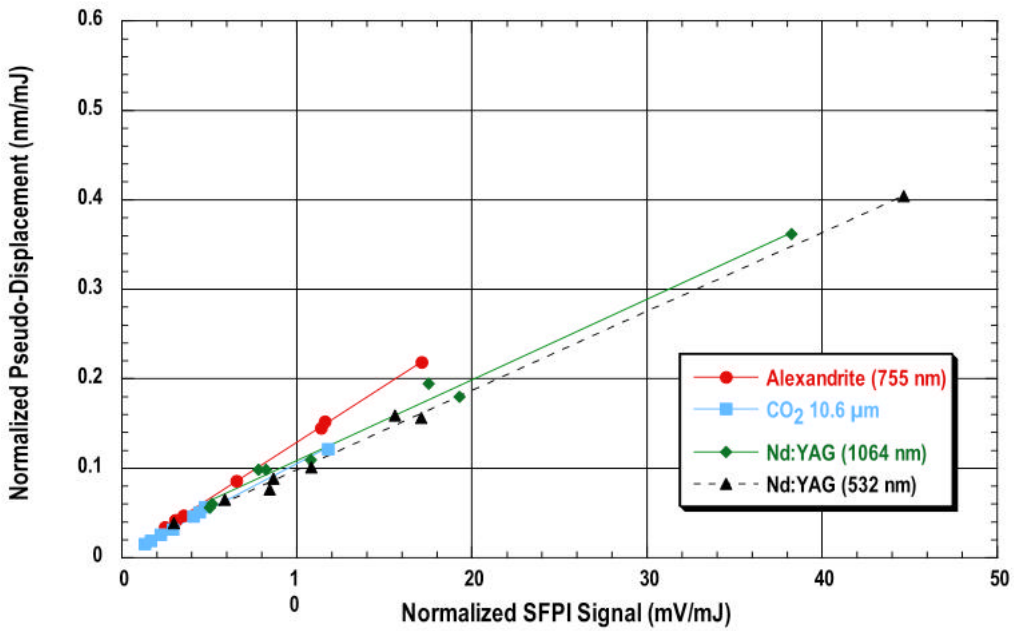


Figure E-4. Plot of the Pseudo-Displacement Obtained by Integration of the SFPI signal, as a Function of the Raw SFPI Signal Amplitude